DEVELOPMENT OF CALCIUM SILICATE COMPOSITES FOR BONE TISSUE ENGINEERING

MEHDI MEHRALI

THESIS SUBMITTED IN FULFILMENT OF THE REQUIREMENT FOR THE DEGREE OF DOCTOR OF PHILOSOPHY

FACULTY OF ENGINEERING

UNIVERSITY OF MALAYA

KUALA LUMPUR

2015

UNIVERSITI MALAYA

ORIGINAL LITERARY WORK DECLARATION

Name of Candidate: MEHDI MEHRALI

Registration/Matric No: KHA110042

Name of Degree: DOCTOR OF PHILOSOPHY

Title of Project Paper/ Research Report/ Dissertation/ Thesis ("This Work"):

Development of calcium silicate composite for bone tissue engineering

Field of Study: Advanced Materials

I do solemnly and sincerely declare that:

(1) I am the sole author/writer of this Work;
(2) This work is original;
(3) Any use of any work in which copyright exists was done by way of fair dealing and for permitted purpose and any excerpt from, or reference to or reproduction of any copyright work has been disclose expressly and sufficiently and the title of the Work and its authorship have been acknowledge in this Work;
(4) I do not have any actual knowledge nor do I ought reasonably to know that the making of this work constitutes an infringement of any copyright work;
(5) I hereby assign all and every rights in the copyright to this work to the University of Malaya (UM), who henceforth shall be owner of the copyright in this work and that any written consent of UM having been first had and obtained;
(6) I am fully aware that if in the course of making this work I have infringed any copyright whether intentionally or otherwise, I am be subject to legal action or any other action as may be determined by UM.

Candidate's Signature Date

Subscribed and solemnly declared before,

Witness's Signature Date

Name:

Designation

ABSTRACT

Calcium silicate ($CaSiO_3$, CS) ceramics is a promising bioactive material for bone tissue engineering, particularly for bone repair. However, the brittle nature and low fracture toughness of CS often result in premature fracture of implants. Hence, there is a need to improve the fracture toughness of CS without compromising its biocompatibility. In this project, CS ceramic composites with improved mechanical strength and comparatively high bioactivity were fabricated for load-bearing applications in bone tissue engineering.

In the first step, calcium silicate hydrate (CSH), consisting of nanosheets, has been successfully synthesized assisted by a tip ultrasonic irradiation (UI) method using calcium nitrate (Ca (NO_3).$4H_2O$), sodium silicate ($Na_2SiO_3 \cdot 9H_2O$) and sodium dodecyl sulfate (SDS) in water. Systematic studies found that the reaction time of ultrasonic irradiation and concentrations of surfactant (SDS) in the system were important factors to control the crystallite size and morphology.

Recent findings indicating the promising biocompatibility of graphene imply that graphene can be used as an additive to improve the mechanical properties of composites. Therefore, in the second step, we report a simple method for the synthesis of calcium silicate/reduced graphene oxide (CS/rGO) composites using a hydrothermal approach followed by hot isostatic pressing (HIP). Adding rGO to pure CS increased the hardness of the material by ~40%, the elastic modulus by ~52% and the fracture toughness by ~123%. Different toughening mechanisms were observed including crack bridging, crack branching, crack deflection and rGO pull-out, thus increasing the resistance to crack propagation and leading to a considerable improvement in the fracture toughness of the composites. The formation of bone-like apatite on a range of CS/rGO composites with rGO weight percentages ranging from 0 to 1.5 has been

investigated in simulated body fluid (SBF). The cell adhesion results showed that human osteoblast cells (hFOB) can adhere to and develop on the CS/rGO composites. In addition, the proliferation rate and alkaline phosphatase (ALP) activity of cells on the CS/rGO composites were compared with the pure CS ceramics.

In the third step, CS ceramic composites reinforced with graphene nanoplatelets (GNP) were prepared using hot isostatic pressing (HIP) at 1150°C. Quantitative analysis suggests that GNP plays a role in microstructure development and is responsible for the improved densification. A uniform distribution of 1 wt. % GNP in the CS matrix, high densification and fine CS grain size help to improve the fracture toughness by ~130%, hardness by ~30% and brittleness index by ~40% as compared to the CS matrix without GNP. The CS/GNP composites exhibit good apatite-forming ability in the simulated body fluid (SBF). These results indicate that the addition of GNP decreased the pH value in SBF. The effect of addition of GNP on early adhesion and proliferation of human osteoblast cells (hFOB) was measured in vitro. The CS/GNP composites showed good biocompatibility and promoted cell viability and cell proliferation. The results indicated that the cell viability and proliferation are affected by time and concentration of GNP in the CS matrix.

ABSTRAK

Kalsium silikat ($CaSiO_3$, CS) seramik menjanjikan bahan-bahan bioaktif yang digunakan untuk kejuruteraan tisu tulang, terutamanya pembaikan tulang. Sebaliknya, sifat rapuh dan keliatan patah yang rendah pada CS sering menyebabkan keretakan pramatang implan. Oleh hal yang demikian, keliatan patah CS perlu dipertingkatkan tanpa menjejaskan sifat biocompatibility yang sedia ada. Dalam projek ini, CS komposit seramik direka dengan kekuatan mekanikal yang lebih baik dan bioaktiviti agak tinggi untuk aplikasi menanggung beban dalam kejuruteraan tisu tulang.

Dalam langkah pertama, kalsium silikat hidrat (CSH) yang terdiri daripada nanosheets telah berjaya disintesiskan melalui kaedah penyinaran ultrasonik tip (UI) dengan menggunakan kalsium nitrat (Ca (NO_3).$4H_2O$), natrium silikat ($Na_2SiO_3 \cdot 9H_2O$) dan natrium dodecyl sulfat (SDS) dalam air. Kajian sistematik mendapati bahawa tindak balas masa penyinaran ultrasonik dan kepekatan surfaktan (SDS) dalam sistem merupakan faktor penting untuk mengawal saiz kristal dan morfologi.

Penemuan-penemuan baru menunjukkan biocompatibility graphene menandakan bahawa graphene boleh digunakan sebagai bahan tambahan untuk meningkatkan sifat-sifat mekanik komposit. Oleh itu, dalam langkah kedua, kami melaporkan kaedah yang mudah untuk sintesis kalsium silikat/reduced graphene oksida (CS/rGO) komposit dengan menggunakan pendekatan hidrotermal diikuti dengan penekanan sestatik panas (HIP). Penambahan rGO pada CS tulen meningkatkan kekerasan bahan pada ~40%, modulus elastik pada ~52% dan keliatan patah pada ~123%. Perbezaan kekuatan mekanisme yang diperhatikan termasuk retak penyambung, retak cawangan, pesongan retak dan rGO tarik keluar, sekaligus meningkatkan daya tahan untuk perambatan retak dan membawa kepada peningkatan yang besar dalam keliatan patah bagi komposit. Pembentukan bone-like apatit dalam pelbagai komposit CS/rGO dengan rGO peratusan berat antara 0-1,5 telah disiasat melalui simulasi cecair badan (SBF). Keputusan lekatan

sel menunjukkan bahawa sel-sel osteoblast manusia (hFOB) boleh mematuhi dan terjadi pada komposit CS/rGO. Di samping itu, aktiviti kadar percambahan dan phosphatase alkali (ALP) sel-sel pada komposit CS / rGO telah bertambah baik berbanding dengan seramik CS tulen. Keputusan ini menunjukkan bahawa komposit kalsium silikat/pengurangan graphene oksida adalah bahan yang menjanjikan untuk aplikasi bioperubatan.

Dalam langkah ketiga, CS komposit seramik diperkuatkan dengan nanoplatelets graphene (GNP) yang disediakan dengan menggunakan isostatic panas menekan (HIP) pada 1150°C. Analisis kuantitatif mikrostruktur menunjukkan bahawa GNP memainkan peranan dalam saiz butiran dan bertanggungjawab untuk pemadatan yang lebih baik. Taburan seragam 1 wt.% GNP dalam matriks CS, pemadatan yang tinggi dan saiz butiran CS yang halus membantu untuk meningkatkan keliatan patah pada ~130%, kekerasan pada ~30% dan indeks kerapuhan pada ~40% berbanding dengan matriks CS tanpa KNK. Komposit GNP/CS mempamerkan kebolehan apatite-forming yang baik di dalam simulasi cecair badan (SBF). Keputusan menunjukkan bahawa penambahan GNP menurunkan nilai pH di SBF. Kesan penambahan GNP pada lekatan awal dan pembiakan sel-sel osteoblast manusia (hFOB) diukur secara in vitro. Komposit GNP/CS menunjukkan biocompatibility baik dan menggalakkan daya maju sel dan percambahan sel. Keputusan menunjukkan bahawa daya maju sel dan perkembangan dipengaruhi oleh masa dan kepekatan GNP dalam matriks CS.

ACKNOWLEDGMENTS

I am deeply indebted to my supervisors, Associate Prof. Dr. Hendrik Simon Cornelis Metselaar and Dr. Nahrizul Adib Kadri for their consultation and guidance of this research project and thesis. Working with them has been a great experience.

I am greatly indebted to all my committee members, who gave me their experience, knowledge, support and resources. Special appreciation is due to Prof. Dr. Noor Azuan Abu Osman and Associate Prof. Dr. Keivan Zandi who have gone a long way beyond duty to support me in the difficult times.

I would like to thank my brother Mr. Mohammad Mehrali for the useful discussions and help, which we experienced in all the steps of my study. Also, valuable discussions with A.R. Akhiani and staff members are greatly appreciated.

I would also like to convey thanks to the University of Malaya, Bright Sparks Unit and Ministry of Higher Education (MOHE) of Malaysia, Grant number UM.C/HIR/MOHE/ENG/10 D000010-16001 and Institute of Research Management and Consultancy (IPPP), University of Malaya No. (PV008/2012A), for providing the financial support and laboratory facilities.

Last but not the least, heartfelt thanks extended to my beloved family for their love, support and encouragement.

Table of Contents

LIST OF FIGURES

LIST OF TABLES

LIST OF SYMBOLS AND ABBREVIATIONS

AFM	Atomic force microscopy
ALDs	Average lateral dimensions
ALP	Alkaline phosphatase
ATCC	American type culture collection
AW-GC	Apatite-wollastonite glass ceramic
β-TCP	β-tricalcium phosphate
Ca	Calcium
CLSM	Confocal laser scanning microscopy
CMS	Critical micelle concentration
CNT	Carbon nanotube
CS	Calcium silicate
CSH	Calcium silicate hydrate
CTAB	Hexadecyltrimethylammonium bromide
DW	Distilled water
E	Elastic modulus
E_r	Reduced modulus
ECM	Extracellular matrix
EDX	Energy dispersive X-ray spectroscopy
FESEM	Field emission scanning electron microscopy
FTIR	Fourier transform infrared spectroscopy
GO	Graphene oxide
GNP	Graphene nanoplatelets
HA	Hydroxyapatite
hFOB	Human fetal osteoblast

HIP	Hot isostatic pressing
HMDS	Hexamethyldisilazane
hMSCs	Human mesenchymal stem cells
HOG	Human oligodendroglia
H	Hardness
iPSC	Induced pluripotent stem cells
TEM	Transmission electron microscopy
Ti	Titanium
k	Thermal conductivity, W/m.K
K_{IC}	Fracture toughness
Kg	Kilogram
LDH	lactate dehydrogenase
MTT	Methyl thiazole tetrazolium (Assay)
PBS	Phosphate buffered saline
PGA	Polyglycolic acid
PLA	Polylactic acid
PLGA	Poly (lactic-co-glycolic acid)
rGO	Reduced graphene oxide
SBF	Simulated body fluid
SD	Standard deviation
SDS	Sodium dodecyl sulfonate
Si	Silicon
SiO_3	silicate
SPS	Spark plasma sintering
Sr	Strontium
SSP	Size–strain plot

UI	Ultrasonic irradiation
vol.%	Volume percentage
wt.%	Weight percentage
XRD	X-ray diffraction

Greek symbols

Θ	Angle
ρ	Density, kg/m^3
ε	Lattice strain
ν	Poisson's ratio

CHAPTER 1

INTRODUCTION

1.1 Background

Today, people pay more and more attention to the quality of life, especially to medical care and rehabilitation, due to the development of society and the improvement of human's living standards. Hence, the field of biomaterials is a rapidly emerging one, because of its direct relation to healthcare and impact on human health related issues.

In general, the types of orthopedic biomaterials are classified into two groups. In the first group are implants and fixing accessories, which are commonly made of ceramics, hard polymers, metals or their composites. The next category are scaffolds for bone tissue regeneration, which are based on polymers - preferably the biodegradable ones and their composites. It is notable that the mechanical properties of each biomaterial strongly influence how it can be utilized in orthopedics. Implants can also include genetic or molecular factors that will be released when the biomaterial dissolves, and these released soluble factors are expected to direct the osteogenic differentiation of osteoprogenitor cells. Therefore, new biomaterials must be developed that are biocompatible and mimic the properties of natural bone, such as matching the functional and mechanical behaviour of the tissue to be replaced, and that form a stable bond between the implant and the surrounding tissue after implantation.

Traditional hard tissue replacing materials consist of polymers, metals, ceramics and their composites. Some clinical applications of these materials have been accomplished. However, there are significant disadvantages of these materials. The popular metals in clinical application are titanium (Ti), stainless steel and its alloys. Some hip joints, bone fixing plates and bolts are made of these metals. Studies have shown that Ti and its alloys are among the most successful metallic biomaterials for

dental and orthopaedic applications because of their good mechanical properties (elastic modulus, strength, toughness and fatigue), excellent corrosion resistance, and good biocompatibility. However, Ti and Ti alloys are bioinert and cannot promote tissue bonding to the implants. Moreover, there is a stress shielding problem when they are used to replace hard tissues, especially in load bearing conditions. The theory of stress shielding hypothesizes that bone loss around orthopedic and implants is due to the removal of normal stress from the bone by an implant (O'Mahony, Williams, & Spencer, 2001). Polymer materials can be easily shaped and some of them, such as polyglycolic acid (PGA), poly (lactic-co-glycolic acid (PLGA) and polylactic acid (PLA) are biocompatible and biodegradable. Nevertheless, their degradation rate does not match well with the growing speed of new bone (Simitzis & Baciu, 2012). Bioceramics have been used in many medical, orthopedic, and dental applications. Bioceramics do not release toxic elements to the human body, even if they are exposed to body fluid for a long time. Bioceramics are classified mainly into three groups on the basis of the interactions between the implant material and the tissues. These groups are called bioinert, bioactive and biodegradable ceramics, respectively. Bioinert ceramics such as alumina and zirconia have stable structures, and there is no chemical reaction or biodegradation when they are implanted in human body. Although these ceramics are famous for thier high chemical stability and mechanical strength, they do not form biochemical interfacial bonds with the tissues (Yelten, Yilmaz, & Oktar, 2012). Biodegradable ceramics such as β-tricalcium phosphate (β-TCP) gradually resorb and are totally replaced by new bone ingrowths. β-tricalcium phosphate is not commonly used in load-bearing conditions due to their low mechanical strength. Bioactive ceramics such as hydroxyapatite (HA), glass ceramic A-W, and bioglass are now widely used as bone-repairing materials (Shanthi, Ashok, Balasubramanian, Riyasdeen, & Akbarsha, 2009). They bond to and integrate with living bone spontaneously by

forming a biologically active bone-like apatite layer on their surfaces in the body (X. Liu, Morra, Carpi, & Li, 2008). Calcium silicate ($CaSiO_3$, CS) is a novel bioactive ceramic that enables excellent attachment and proliferation of osteoblast cells and promotes apatite formation, making it an attractive candidate biomaterial for hard tissue repair (Gandolfi et al., 2010; X. Y. Liu, Ding, & Wang, 2001; Lu, Zhu, Ao, Qi, & Chen, 2012; Magallanes-Perdomo et al., 2010; Ni, Chang, & Chou, 2006; Ni, Chang, Chou, & Zhai, 2007). Calcium silicate bioceramics has two polymorphs, β-calcium silicate (low-temperature phase) and α-calcium silicate (high-temperature phase), with a phase-transition temperature of 1125 °C. Both materials were shown to be bioactive in the middle of 1990s due to a formation of surface hydroxyapatite (C. Wu & J. Chang, 2013). Moreover, some studies have shown that calcium silicate hydrate (CSH) can induce the formation of a bone-like apatite layer on its surface after soaking in simulated body fluid (SBF) (Lin, Chang, & Cheng, 2007). The biocompatibility, stability, heat-insulating ability, low dielectric loss at high frequency and mechanical properties of calcium silicates are determined by their morphology, crystal size, composition and structure. Hence, the control over the morphology of calcium silicate and CSH is of great importance for biomedical and industrial applications (Lin, Chang, & Lu, 2006; J. Wu, Y.-J. Zhu, S.-W. Cao, & F. Chen, 2010). However, the insufficient strength and toughness of this material remain major hurdles that impede its application in load bearing conditions (Lin et al., 2005; Long, Zhang, Chen, Chen, & Chang, 2008). One of the possible solutions is reinforcement of CS by a second phase material that can help improve the fracture toughness of the CS matrix. Thus, toughening of CS with a second phase such as yttria stabilized zirconia, alumina, Ti_3SiC_2 and titanium has been explored to overcome the deficiencies of pure CS (Pattanayak, Prasad, Rao, & Mohan, 2006; S. J. Zhao, Wang, Jiang, Zhang, & Chen, 2008). Keeping the biocompatibility of the composite structure in mind, the ideal reinforcement material is one that can

enhance the fracture toughness remarkably with a low content of reinforcement phase. The lower content of reinforcement phase ensures introduction of a minimum of foreign elements into the living body. Hence, it is important that the reinforcement phase possesses excellent strength and elastic modulus, in order that a minimum content can improve the fracture toughness of CS significantly. It is notable that the CS is difficult to densify by an ordinary sintering technique. In order to solve these problems, some investigators were able to fabricate dense CS ceramics with better properties using other sintering methods such as hot isostatic pressing and spark plasma sintering, instead of conventional methods (Zhong et al., 2011). So far, few of the materials such as alumina, zirconia and Ti_3SiC_2 that have been attempted for CS-based bioceramics have sufficient mechanical properties and favourable biocompatibility.

1.2 Graphene: Potential reinforcement to calcium silicate

Graphene, a flat monolayer of carbon atoms in a two-dimensional (2D) honeycomb lattice with a high aspect ratio layer geometry and a very high specific surface area, has attracted tremendous attention in recent years due to its exceptional thermal, mechanical and electrical properties (Ferrari & Basko, 2013; M. Mehrali, Latibari, Mehrali, Metselaar, & Silakhori, 2013; Z. P. Xu & Buehler, 2010). Graphene sheets have been applied in various biotechnologies such as bacteria inhabitation (Akhavan & Ghaderi, 2010; Tang et al., 2013), biosensing (Akhavan, Ghaderi, & Rahighi, 2012), drug delivery (L. M. Zhang, Xia, Zhao, Liu, & Zhang, 2010), cellular imaging (Peng, Hu, Zhou, Fan, & Huang, 2010), cancer targeting (Robinson et al., 2011), antiviral materials (Akhavan, Choobtashani, & Ghaderi, 2012), tissue engineering (Fan et al., 2014; Liao, Lin, Macosko, & Haynes, 2011; K. Zhou et al., 2012), and many other, due to its extremely large surface area, good biocompatibility, biostability and ease of chemical functionalization. Much of the work on graphene composites has focused on polymer matrix composites. The addition of graphene has

resulted in the improvement of electrical and mechanical properties of the polymer matrix composites (Castelain, Martinez, Marco, Ellis, & Salavagione, 2013; Ramanathan et al., 2008; K. Zhou et al., 2012). In recent years, there has been great interest in using graphene-based nanofillers, such as graphene oxide (GO), graphene nanoplatelets (GNPs), and reduced graphene oxide (rGO), to improve the mechanical performance of ceramics and bioceramics such as Si_3N_4 (Walker, Marotto, Rafiee, Koratkar, & Corral, 2011), zirconia/alumina composites (J. Liu, H. X. Yan, M. J. Reece, & K. Jiang, 2012), Al_2O_3 (J. Liu, H. Yan, & K. Jiang, 2013), hydroxyapatite (HA) (Y. Liu, Huang, & Li, 2013; Lv Zhang et al., 2013) and biphasic calcium phosphate composites (Y. Zhao et al.). All graphene-reinforced ceramic matrix composites were found to exhibit a decreased tendency to fracture, mainly due to crack bridging, crack deflection, crack tip shielding and crack branching. Li et al. (M. Li et al., 2013) synthesized nano-hydroxyapatite on pristine and chitosan functionalized graphene oxide (GO), which was densified using spark plasma sintering (SPS), to report on the effects of functionalized GO enhancing the cytocompatibility of a composite. Zhang et al. (Lv Zhang et al., 2013) prepared and characterized GNP/HA composites and reported the improvement of the mechanical properties, *in vitro* biocompatibility, good bone bonding ability and promotion of the deposition of plate-like HA in a simulated body fluid (SBF) solution as compared to pure HA. Moreover, recent studies have shown that GNP-based composites possess a series of merits, e.g., are non-toxic for human osteoblasts and mesenchymal stromal cells (Kalbacova, Broz, Kong, & Kalbac, 2010), suitable for adhesion and proliferation of osteoblasts (W. B. Hu et al., 2010). In recent years, reduced graphene oxide has emerged as a competitively alternative material for graphene. Thermal annealing or chemical treatment can eliminate functional groups on GO to produce reduced graphene oxide (rGO) (He et al., 2010; Hu et al., 2013) Agarwal et al.(Agarwal et al., 2010) tested the biocompatibility

of rGO with human fetal osteoblast (hFOB) cells, human oligodendroglia (HOG) cells and rat pheochromocytoma (neuroendocrine cell, PC12) cells and found that rGO is biocompatible with all the cells tested (Agarwal et al., 2010). Akhavan et al. (Akhavan, Ghaderi, & Akhavan, 2012) reported that the rGO do not display genotoxicity in the human mesenchymal stem cells (hMSCs). However, they found that interaction of rGO with stem cells and probably other biological systems such as organisms and tissues strongly depends on the lateral size of the sheets. Very recently, Liu et al. (Y. Liu et al., 2013) found that the rGO reinforcement in HA for load-bearing orthopedic implants is compatible with hFOB cells with an increase in fracture toughness compared to pure HA.

Thus, theoretically, graphene has the capabilities to serve as reinforcement to CS in orthopedic application.

1.3 Objectives of the current research

The overall objectives of this research are to synthesize of CSH and CS/graphene composites, and study the biocompatibility and apatite forming ability of CS/graphene composites.

This research work is broken down into the following specific tasks:

- To develop a facile method to synthesize CSH by employing a tip ultrasonic irradiation in water solvent.
- To use a simple hydrothermal method to synthesize CS nanowires on graphene oxide sheets, and investigate the influence of rGO filling percentages on the mechanical properties of fabricated composites.
- Exploring the potential of GNP as an alternative reinforcement to CS in terms of mechanical properties improvement and analyzing the role of graphene sheets (rGO and GNP) reinforcement in fracture toughness behavior of CS based composites.

- To investigate the apatite-forming ability of the fabricated composites in simulated body fluid (SBF), to study the effect of rGO and GNP content on the formation of HA on the fabricated composites.
- *In-vitro* evaluation of biocompatibility of CS-graphene sheets (rGO and GNP) composites by using human fetal osteoblast cells (hFOB).

1.4 Structure of thesis

This dissertation is arranged in different chapters. Chapter one highlights the background of the study, the problems existing in this area which provide the motivation for this research, and the objective of this research. Chapter two presents a literature review on this subject. Moreover, this chapter highlights those study areas that have not received much attention yet. Chapter three provides a detailed account of the methodology adopted in this project. Explanation of the results and scientific analysis of the outcomes in context with the objective of this study is discussed in chapter four. Comprehensive conclusions together with recommendations for further work on CS-graphene composites that would take this orthopedic implant material to clinical application stage are presented in chapter five.

CHAPTER 2

LITERATURE REVIEW

2.1 Overview of Bioceramics

Bone is a complex living tissue which has an elegant structure at different hierarchical scales. It is basically a composite comprising of an organic phase (based on collagen) in which calcium-containing inorganic crystals are embedded (Driessens, 1980). However, although the skeleton plays a vital role in the mammalian body both in terms of support and locomotion and also the protection of vital organs, it is susceptible to fractures as a result of injury and degenerative diseases which are often associated with ageing. Therefore there has always been a need, since the earliest time, for the repair of damaged hard tissue. The earliest attempts to replace hard tissue with biomaterials aimed to restore basic functions by repairing the defects caused by injury and disease. However, the aim was to elicit minimal biological response from the physiological environment. These materials are now largely classed as "Bioinert" and the absence of a toxic response would have been considered to be a successful outcome (Dinan, Gallego-Perez, Lee, Hansford, & Akbar, 2013). Although bioinert ceramics have been successfully used as hip prostheses, dental implants and joint prostheses in clinical applications, the bioactivity of the bioinert ceramics is poor (Hench, 1991). It is noted that the bioinert ceramics cannot bond with the natural bone directly, and fibrous tissue is generally generated around bioinert ceramics after implantation. Therefore, the bonding strength between the bioinert ceramic and the natural bone is weak. The bioinert ceramic implants were generally fixed through mechanical interlocking with the natural tissue. As with many biomedical implants, the material used in clinical application was originally designed for quite different purposes and the development of bone cement and some of the metallic alloys are prime examples of this. However, more

recently, interest has been directed towards the advantageous properties of ceramics including their excellent levels of chemical resistance, compressive strength and wear resistance. In the 1920s De Jong (Best, Porter, Thian, & Huang, 2008) first observed the similarities between the X-ray diffraction patterns of bone mineral and a calcium phosphate compound, hydroxyapatite. Later Posner and co-workers identified the crystallographic structure of bone mineral and hydroxyapatite (Barralet, Best, & Bonfield, 2000; Bauer, Geesink, Zimmerman, & McMahon, 1991; Bonfield, Grynpas, Tully, Bowman, & Abram, 1981). A series of studies in the 1960s, revealed that the presence of carbonate in bone and tooth mineral and hydroxyapatite may be observed directly, using infrared spectroscopy, in the form of weak peaks between 870 and 880 cm^{-1} and a stronger doublet between 1460 and 1530 cm^{-1} and also through alterations in the hydroxyapatite lattice parameters from X-ray diffraction (Zapanta-Legeros, 1965). The effect of the substitution of electronegative anions, such as fluoride and chloride for (OH^{-}), were also reported to influence the lattice parameters of the structures (Elliott & Young, 1967). However, the main thrust of these studies was characterisation and it was not until later in the 1960s and beyond that the development of bioactive ceramics came of age.

2.1.1 Bioactive Ceramics

Bioactive materials can elicit a specific biological response at the tissue/material interface which results in the formation of a bond between the tissue and the material. When a bioactive material is implanted into the human body, a series of biochemical and ion-exchange reactions occur between the bioactive implant and the surrounding body fluids resulting in the formation of a layer of bone-like apatite on the implant that is chemically and crystallographically equivalent to the mineral phase in bone, which promotes the bonding between the natural tissues and the material. Similar to other bioactive materials, bioactive ceramics can directly bond to the living bone tissue.

Typical examples of the conventional bioactive ceramics are synthetic hydroxyapatite (HA), Apatite-wollastonite glass ceramic (AW-GC) and Bioglass$^{@}$. In the last 20 years, novel bioactive ceramics and coatings/films were frequently investigated and explored, such as $CaO\text{-}SiO_2$ based ceramics and coatings. Since the discovery of bioglass by Hench and Anderson (Hench, 1991) in 1969, several glasses and glass ceramics were found to bond to living bone. All those bioglass and glass-ceramic components include the components of $CaO\text{-}SiO_2$. Kokubo and Ohtsuki et al. (Kokubo, 1990, 1991) pointed out that the $CaO\text{-}SiO_2$ components contributed mainly to the bioactivity of those materials. Therefore, some ceramics and coatings such as calcium silicate ($CaSiO_3$, CS), dicalcium silicate (Ca_2SiO_4) and diopside ($CaMg\text{-}Si_2O_6$), have been regarded as biomaterials, they may be the potential candidates for artificial bone.

2.1.2 Bioactive calcium silicate ceramics

Calcium silicate is an important compound in the ceramic and cement industries (X. Liu et al., 2008; Vukovich, 1956). Calcium silicate has three main polymorphs viz. triclinic wollastonite (TC), parawollastonite and pseudowollastonite. Wollastonite TC and parawollastonite are both referred to as the low temperature form (β-$CaSiO_3$, β-CS). The term wollastonite TC means triclinic wollastonite, which is a common mineral in nature (Henmi, Kawahara, Henmi, Kusachi, & Takeuchi, 1983). Parawollastonite is monoclinic, and is rarer in nature. Parawollastonite is distinguished from wollastonite TC by the slight inclination of the optic axial plane. Nevertheless, the properties of parawollastonite and wollastonite TC are closely related (X. Liu et al., 2008). Pseudowollastonite, the high temperature form (α-$CaSiO_3$, α-CS), is triclinic, and is known in nature merely in pyrometamorphosed tertiary rocks. The phase-transition temperature β-$CaSiO_3$ to α-$CaSiO_3$ is higher than 1125°C (X. Liu et al., 2008).

Calcium silicate powders and ceramics (β-CS and α-CS) were shown to be bioactive in the middle of 1990s due to a formation of a bone-like hydroxyapatite (HA)

surface layer after exposure to a stimulated body fluid (SBF), human saliva, and to form a bond to living bone in vivo by the formation of a hydroxyapatite layer surface (De Aza, Luklinska, Anseau, Guitian, & De Aza, 1999; X. Y. Liu, Ding, & Chu, 2004; S. Xu et al., 2008). This type of HA layer plays an essential role in forming a tight chemical bond between the bioactive material and the surrounding bone tissue (Kokubo & Takadama, 2006). Since then, numerous other studies further demonstrated that CS was a promising candidate material for bone replacement. Interestingly, some reports also indicated that the formation rate of hydroxyapatite on the surface of CS was faster than on the other biocompatible glasses and glass ceramics in SBF solution (Siriphannon, Kameshima, Yasumori, Okada, & Hayashi, 2000; S. Xu et al., 2008). Xu et al. also showed the potential of CS ceramics to become a third generation of biomaterials for artificial bone, which have enhanced bioactive and bioresorbable properties (S. Xu et al., 2008). Siriphannon et al. investigated the effect of the structure of the CS powders on the formation behaviour of HA by soaking various amorphous and crystalline CS powders (β-CS and α-CS) in a SBF solution for varying periods (Siriphannon, Kameshima, Yasumori, Okada, & Hayashi, 2002). They found that the amorphous CS powders showed a faster formation of HA because of the rapid release of calcium (Ca) ions in SBF solution. In addition, it is reported that dissolution may play an important role in influencing the apatite mineralization of calcium silicate ceramics. Moreover, they observed that after prolonged soaking, a denser layer of larger particle size formed on β-CS and α-CS as compared to amorphous CS powders. Generally, calcium silicate bioceramics posses improved apatite-forming ability in the SBF. However, the incorporation of other metal ions, such as magnesium (Mg), zinc (Zn) and zirconium (Zr) into calcium silicate ceramics will decrease their apatite mineralization.

2.2 Structure, synthesis, Properties and Fabrication Methods of CS

2.2.1 Calcium silicate hydrate

Calcium silicate hydrates (CSH) have potential applications in biomedical fields such as drug delivery (S. K. Jain, Awasthi, Jain, & Agrawal, 2005; J. Wu, Y. J. Zhu, S. W. Cao, & F. Chen, 2010) and bone tissue engineering (Wei, Chen, et al., 2009; S. Xu et al., 2008) owing to their comparatively good bioactivity, biocompatibility and biodegradability, and thus have drawn growing attention in recent years. CSH is the principal hydration product and primary binding phase in portland cement (P. Yu, R. J. Kirkpatrick, B. Poe, P. F. McMillan, & X. D. Cong, 1999). The calcium silicate hydrates possess a notable level of structural complexity. In excess of 30 crystalline CSH phases are known, and preparations made near room temperature have structures that range from semicrystalline to nearly amorphous (J. J. Chen, Thomas, Taylor, & Jennings, 2004). The Ca/Si molar ratio of the CSH gel free of hydrous silica and portlandite ($Ca(OH)_2$) can range from 0.66 to 1.5 (Bonaccorsi, Merlino, & Taylor, 2004; Nonat, 2004). The CSH is generally similar to those of tobermorite ($Ca_5Si_6O_{16}(OH)_2 \cdot 8H_2O$) and/or jennite ($Ca_9(Si_6O_{18})(OH)_6 \cdot 8H_2O$) (Nonat, 2004). Tobermorite and jennite are rare natural minerals that also form in autoclaved building and thermal insulation materials. However, the formation of tobermorite-like CSH is believed to occur when it has a low Ca/Si molar ratio (usually less than 1) while the Ca/Si ratio of jennite is 1.5 (J. J. Chen et al., 2004). The primary structural unit of tobermorite is a layer composed of CaO polyhedral sheets sandwiched between single silicate chains. The silicate chains that repeat at intervals of three silicate tetrahedra. Two of these tetrahedra, called paired tetrahedra, share two oxygen atoms with the central CaO sheet, while the third, called a bridging tetrahedron, shares only one. These calcium silicate layers have a negative charge and are held together by Ca^{2+} ions in the interlayer region, which also contains H_2O molecules. The minimum basal spacing, the c-axis dimension,

is ~0.98 nm, and additional H_2O molecules expand it to ~1.1 and 1.4 nm. Both 1.1 nm tobermorite and 1.4 nm tobermorite have similar [100] and [010] unit-cell dimensions, ideally contain single dreierketten silicate chains, and have similar oxygen sites (J. Wu, Zhu, & Chen, 2013). The idealized structural formula for 1.1 nm tobermorite is $Ca_{2.25}$ $(Si_3O_{7.5}$ $(OH)_{1.5}).H_2O$ with a C/S ratio of 0.83 but bridging silicate tetrahedra may be missing or crosslinked, resulting in a variable C/S ratio. The interlayer Ca^{2+} may be substituted by other cations (P. Yu et al., 1999).

The crystal structure of jennite is generally similar to that of tobermorite of as with tobermorite, the structure is based on layers in which a central CaO sheet is flanked on both sides by rows of single dreierketten, together with interlayer Ca^{2+} ions and water molecules (P. Yu et al., 1999). An important difference between tobermorite and jennite is that every other silicate chain is omitted and substituted by OH^-. Gard et al. suggested that the idealized jennite structural formula is $(Ca_8$ $(Si_6O_{18}H_2)$ $(OH)_8)$ $Ca.6H_2O$, which is based on corrugated sheets with a composition $(Ca_8Si_6O_{18}H_2(OH)_8.2H_2O)^{2-}$ lying parallel to (001), with additional Ca^{2+} cations and H_2O molecules sandwiched between them (Gard, Mohan, Taylor, & Cliff, 1980). Taylor reported that CSH with a C/S ratio >1.5 (called CSH (II)) has a structure similar to jennite, while CSH with a C/S ratio <1.5 (called CSH (I)) has a structure similar to tobermorite (Taylor, 1986). The other form of CSH structure is xonotlite, which has been attracting attention in recent years. Xonotlite $(Ca_6Si_6O_{17}$ $(OH)_2)$ is a fibrous hydrate silicate of calcium, whose chemical composition is closely related to tobermorite but has double chains running parallel to the *b*-axis which form layers in the *ab* plane (Burzo, 2006; Shaw, Clark, & Hendersona, 2000). Upon dehydration, xonotlite is in fact transformed into calcium silicate. Moreover, Thermogravimetric (TGA) analysis indicated on both synthetic and natural xonotlite show higher water content than assumed by the above formula (Burzo, 2006).

Generally, a comprehensive understanding of the CSH and/or CS crystal structure and ion substitute properties can help to fabricate CS particles based on the application requirements and understanding of the interaction between bone mineral and CS.

2.2.2 Synthesis of CS

Synthesis of CS particles is usually the first step to produce CS implants. Many methods, such as hydrothermal (X. K. Li & Chang, 2006; Lin, Chang, Chen, Ruan, & Ning, 2007; L. Z. Pei et al., 2010), sol gel (Baciu & Simitzis, 2007; Simitzis & Baciu, 2012), mechanochemical (Shirazi, Mehrali, et al., 2014; Singh & Karmakar, 2011), solid state reaction (Ibanez, Pena, & Sandoval, 1990), sonochemical (M. Zhang & Chang, 2010), microwave (Vichaphund, Kitiwan, Atong, & Thavorniti, 2011) and the chemical precipitation have been developed to prepare CS particles. The methods of chemical precipitation, hydrothermal and sonochemical that have been used in this research are briefly reviewed in the following paragraphs.

2.2.2.1 Chemical precipitation method

The chemical precipitation is low cost, simple and appropriate for industrial production CS. In the chemical precipitation method calcium nitrate ($Ca(NO_3)_2 \cdot 4H_2O$), calcium hydroxide $Ca(OH)_2$ or calcium chloride $CaCl_2$ are the possible sources of calcium (Ca^{2+}), while sodium metasilicate nonahydrate ($Na_2SiO_3 \cdot 9H_2O$) and tetraethyl orthosilicate ($Si(OC_2H_5)_4$ (TEOS)) are sources of silicate (SiO_3^{2-}). The most typical procedure involves the dropwise addition of one reagent to another at room temperature under continuous and gentle stirring, until the ratio of elements (Ca/Si) reaches the required stoichiometric ratio (1) (Lin et al., 2005). A powder prepared by simple precipitation is, however, usually poorly crystallized without any regular shape (Wan, Chang, Mao, Jiang, & Li, 2005). In this method, the particle size can be controlled

through adjusting synthesizing conditions, such as stirring speed and the concentration of the starting chemical.

2.2.2.2 Sonochemical method

The sonochemical method shows potential for the synthesis of nanomaterials due to the acoustic cavitation process in an aqueous medium where the formation, growth and collapse of microbubbles occur. The reactivity of chemicals is increased which increases the speed of the heterogeneous reactions between liquid and solid reactants. The sonochemical method has been used to produce unusual morphologies such as flower-like of monetite (Baradaran, Basirun, Mahmoudian, Hamdi, & Alias, 2013), nanorods of ZnO (Sadjadi & Eskandari, 2013), nanosheets of SnO_2 (H. Wang et al., 2012), hydroxyapatite (Sadat-Shojai, Khorasani, Dinpanah-Khoshdargi, & Jamshidi, 2013) and nanospheres of MnO_2 (Kim, Huh, Han, Cho, & Kim, 2012). According to their study, the efficiency of the synthesis process, morphology, particle size and crystallinity depends on many variables such as ultrasonic irradiation (UI) time, the type of used ultrasonic device, applied UI power, temperature, volume and concentration of ultrasonicated solution. Zhang and Chang prepared CSH microspheres by ultrasonic precipitation using calcium nitrate ($Ca(NO_3)_2 \cdot 4H_2O$) as the calcium (Ca^{2+}) source and sodium metasilicate nonahydrate ($Na_2SiO_3 \cdot 9H_2O$) as the source of silicate(SiO_3^{2-}) in an aqueous medium with cetyltrimethylammonium bromide (CTAB) acts as a surfactant. They showed that addition of CTAB favours the formation of hollow CSH microspheres, which can be used as a bioactive bone implants with drug delivery properties. When CTAB was absent in the solution, only irregular spheres with varied sizes and severe agglomeration were observed. In another study, Wu et al. (J. Wu et al., 2010) proposed a surfactant free sonochemical synthesis of mesoporous spheres of CSH under ambient conditions with well-defined 3D network structures constructed by nanosheets as building blocks. They reported that the structural features of CSH is

desirable for drug delivery due to their large specific surface area, mesopores, and interconnected microchannels for drug loading and release.

2.2.2.3 Hydrothermal method

Among the wet chemical methods, the hydrothermal process appears to have attracted much attention for the synthesis of materials at high temperature and high pressure using super saturated solutions (Sadat-Shojai et al., 2013). In this method, an autoclave or pressure vessel that can provide a high temperature – typically above the boiling point of water and high pressure are needed.

Li et al. (X. K. Li & Chang, 2006) synthesized xonotlite [$Ca_6(Si_6O_{17})(OH)_2$] nanowires with a diameter of 50–100 nm using TEOS and calcium nitrate as the original materials through the hydrothermal method, including CTAB as templates. CTAB is a cationic surfactant and its critical micelle concentration (CMC) is 0.03% (0.9–1.0 mM) (Delsanti, Moussaid, & Munch, 1993). They found that the long reaction time, low reaction temperature and the presence of CTAB favoured the synthesis of xonotlite nanofibers. Meanwhile, the phase of the powders decomposed from xonotlite to β-$CaSiO_3$ during calcination. The main disadvantage is the template solvent that was used in this method is harmful to health and the environment (L. Z. Pei et al., 2010).

Pei et al. (L. Z. Pei et al., 2010) fabricated calcium silicate nanowires from SiO_2 and CaO powders as precursors at 220 °C for 12 h. After being calcined at 800 °C for 1 h, the xonotlite nanowires are completely transformed into β-$CaSiO_3$ nanowires. They reported that the diameter of nanowires measured from transmission electron microscopy (TEM) observations was 30–150 nm. The advantage of this synthesis is that there were no other templates and that it uses cheap source materials. However, the diameter of nanowires has a relatively broad size distribution.

Lin et al. (Lin, Chang, Chen, et al., 2007) synthesized CS nanowires with a diameter of 10‑30 nm and a length up to tens of micrometers from $Ca(NO_3)_2.4H_2O$ and

$Na_2SiO_3.9H_2O$ as the original materials under hydrothermal conditions at 200°C for 24 hours. They reported that Xonotlite nanowires were firstly obtained by hydrothermal treatment; then the single crystalline β-$CaSiO_3$ nanowires were obtained by calcination of the xonotlite at 800°C for 2 h. Their results showed that diameter of nanowires were smaller and well distributed compared to other studies.

2.2.3 Sintering processes

Green or pre-sintered ceramic bodies are densified by the application of heat. This is known as sintering. Moreover, through a powder sintering process, the microstructure of ceramics can be controlled (Carty & Senapati, 1998). Green or pre-sintered ceramic bodies contain pores or voids, which need to be eliminated in order that the material can be fully densified to achieve appropriate mechanical properties. Therefore, one common process for doing that is sintering. The evolving process throughout the sintering process consists of the following steps:

(1) connection of particles;

(2) growth of connection necks;

(3) close of connected pores;

(4) decrease of pores and increase of bulk density;

(5) growth of crystals.

There are several sintering methods for ceramic densification including pressureless sintering, hot isostatic pressing (HIP), spark plasma sintering (SPS), microwave sintering and hot-press sintering. The sintering methods of pressureless sintering and hot isostatic pressing are briefly reviewed in the following paragraphs.

2.2.3.1 Pressureless sintering

Pressureless sintering is the most common method in the fabrication of ceramic materials. This technique imposes relatively low requirements on the equipment and yields products with high performance and desired shapes. Ceramic powders are pressed

in a mold by applying pressure or using other methods such as casting. to obtain shaped bulk samples. Afterward, the green bodies are sintered in air, vacuum or inert gas environments. Optimization of the sintering parameters is of crucial importance, such as compaction pressure, sintering temperature, cooling and heating rate, protection gas and sintering time, which influence the properties of sintered samples (Castillo-Rodríguez, Muñoz, & Domínguez-Rodríguez, 2006). However, the mechanical properties of ceramics sintered by pressureless sintering are comparatively poorer than ceramics sintered by the HIP and SPS methods due to the residual porosity. Furthermore, the sintering duration is generally several hours, which makes it a time consuming process.

2.2.3.2 Hot isostatic pressing

Hot isostatic pressing (HIP) plays an important role in the research and development of different materials, including metals and ceramics. During HIP, high temperature and high gas pressure are simultaneously applied to sintering powder (Bocanegra-Bernal, 2004). The pressurizing medium is normally an inert gas such as pure argon. The HIP method, which subjects a component to elevated temperatures (over 1000 °C) and pressures (over 98 MPa) to eliminate internal micro porosity, helped engineers to respond to regulations of aerospace industry (Bocanegra-Bernal, 2004). High performance ceramics, especially high temperature ceramics such as silicon carbide, alumina, zirconia and silicon nitride, were the first of these materials to be produced commercially, and HIP has been considered one the most promising technologies to fabricate parts with adequate mechanical strength and reliability made from these materials (Echeberria, Tarazona, He, Butler, & Castro, 2002; Hoffmann, Geyer, & Oberacker, 1999). The hot isostatic pressing (HIP) utilizes a high pressure between 100-300 MPa which is applied to an encapsulated chamber so that a high dynamic force is achieved. Thus, highly densified ceramic materials can be produced with limited grain growth. Moreover, HIP is a sealed system, therefore oxidation and

chemical reaction can be limited or prevented. Consequently, HIP is an admirable technique to produce high density and homogeneous materials (Tjong & Lau, 1999). With hot isostatic pressing (HIP) the formation of materials can be controlled and pressure can also be applied to increase the driving force for more densification, even for objects with complex shaped like turbine wheels. Pressure in HIP has been used to aid densification and sintering. HIP has been found as a unique method for forming and densification of ceramics (Bocanegra-Bernal, 2004).

2.2.3.3 CS ceramic composites

CS has a high osteoconductivity, significant biocompatibility and high bioactivity. But the disadvantage CS is that it is inherently brittle and that its mechanical properties are poor (Lin et al., 2005). CS has a comparable bending strength and elastic modulus to human cortical bone in dry test conditions (50–150 MPa) (C. T. Wu & J. Chang, 2013). However, the fracture toughness (K_{IC}) of CS ceramics is lower than 1 MPa $m^{1/2}$, while the fracture toughness value of human cortical bone ranges from 2-12MPa $m^{1/2}$ depending on the type and age of the bones. The poor static and fracture strength limits the application of CS to low or non load-bearing conditions.

Long et al. (Long, Chen, Bai, Chang, & Lin, 2006) have used SPS to fabricate pure CS at different temperatures (900, 950 and 970 °C). They have reported that the sample sintered at 970 °C changed into the high-temperature phase (α-CS) completely and fracture toughness was 0.5 MPa $m^{1/2}$. But at 950 °C β-CS was formed with a fracture toughness of 2 MPa $m^{1/2}$, which is four times more than those reported and much higher than that of HA ceramics. The fracture toughness was found to decrease greatly when the sample changed to α-CS ceramics.

Shirazi et al. (Shirazi, Mehrali, et al., 2014) investigated the sintering behaviour and mechanical properties of α-CS which was prepared by cold isostatic press (CIP) and then sintered by pressureless sintering at 1150 and 1250 °C. When increasing the

sintering temperature from 1150 °C to 1250 °C, the density, Young's modulus and hardness were improved, while the fracture toughness was decreased from 0.7 to below 0.5 MPa $m^{1/2}$. According to these results, various possible methods, such as refining the microstructure of CS particles and incorporating reinforcing phases, have been applied to improve the fracture toughness and hardness of CS ceramics. Composite technologies have been used to improve the mechanical properties of CS, and various types of CS composites have been produced.

CS-Al_2O_3 is a kind of CS-ceramic composite. CS and Al_2O_3 interact with each other during sintering (Shirazi, Mehrali, et al., 2014). The XRD results indicated that the third phase formed is calcium aluminum oxide which can be absorbed by the human body. Moreover, the gehlenite (Ca_2Al [$AlSiO_7$]) was also detected in minor amounts which does not have any inhibitory and toxic effect in vitro (Nath, Kalmodia, & Basu, 2013; Shirazi, Mehrali, et al., 2014). Furthermore, the study has shown the effect of Al_2O_3 on increasing dissociation of CS at this temperature. Their results showed that the hardness and the fracture toughness of the CS- 15 wt. % Al_2O_3 composite fabricated at 1250°C reached 7.2 GPa and 0.9 MPa $m^{1/2}$, respectively. Nevertheless, even though the hardness and Young's modulus of CS-Al_2O_3 composites is increased significantly, the fracture toughness is still low. Moreover, the absorption of calcium aluminum oxide in body fluids weakens the mechanical strength of the implants shortly after implantation (Shirazi, Mehrali, et al., 2014).

Long et al. (Long et al., 2008) studied CS-Zirconia (ZrO_2) composites. They employed spark plasma sintering (SPS) method for a ZrO_2 content varying from 0 to 60 wt. % and a sintering temperature from 950 to 1080 °C. The addition of the ZrO_2 inhibited the phase transition of CS and increased its phase transition temperature from β-CS to α-CS. However, this study investigated the mechanical properties of β-CS/ZrO_2 only. They did not investigate the α-CS/ZrO_2 composite as the mechanical properties of

α-CS were very low. They found that 40wt. % ZrO_2 reinforcement improves the fracture toughness of β-CS (4.08 MPa $m^{1/2}$) sintered at 1050 °C. It should be noted that several research demonstrated that α-CS is less degradable than β phase which is more applicable in high load bearing implants (X. Y. Liu et al., 2004; Shirazi, Mehrali, et al., 2014).

Zhao et al. (S. J. Zhao et al., 2008) have studied Ti_3SiC_2 reinforced CS composites with different Ti_3SiC_2 volume fractions, which were fabricated by SPS at 1150 °C. The bending strength and fracture toughness of the Ti_3SiC_2 reinforced α-CS composites, especially the α-CS composites with 30 vol% of Ti3SiC2, were improved, which can be attributed to the toughening effect on the matrix by the Ti_3SiC_2 phase. The bending strength and fracture toughness of the composites reached 271 MPa and 2.47 MPa $m^{1/2}$ when they were sintered at 1150 °C. However, the hardness value was not reported in this research. Several studies have reported that Ti_3SiC_2 reinforced ceramic matrix composites require high temperature sintering to obtain dense and an acceptable hardness (Shi & Pan, 2007; Shi, Pan, Fang, & Fang, 2006). Moreover, there is one study that reports bending strength and fracture toughness of HA/Ti_3SiC_2 composites were increased, while the hardness was reduced with increasing amount of Ti_3SiC_2 (Shi et al., 2006). In addition, an increasing volume fraction of Ti_3SiC_2 reinforced CS ceramic matrix has been shown to reduce apatite-forming ability on these composites.

Wu et al. (C. T. Wu, Ramaswamy, Soeparto, & Zreiqat, 2008) studied the incorporation of titanium (Ti) into CS. Their results showed that pure sphene ($CaTiSiO_5$) powders are produced by the incorporation of Ti into CS using a sol–gel technique. The compact $CaTiSiO_5$ ceramic showed a significantly higher chemical stability in SBF, compared with CS. Moreover, $CaTiSiO_5$ ceramics supported the attachment of human bone derived cells (HBDC) and spreading and enhanced HBDC

proliferation and differentiation compared to pure CS ceramic. Nevertheless, the mechanical properties were not investigated in this study.

Wu et al. (C. T. Wu, Ramaswamy, Kwik, & Zreiqat, 2007) have also reported incorporation of strontium (Sr) into CS ceramic and they investigated the effects on phase transition, sintering property, apatite-formation ability, ionic dissolution, and HBDC proliferation. Their results indicated that the incorporation of Sr promoted phase transition from β-CS to α-CS. Incorporation of low amounts (1 wt.% and 2.5 wt.%) of Sr into CS resulted in enhanced densification of the ceramics, whereas higher Sr contents (5 wt.% and 10 wt.%) had no obvious effect on the densification. In addition, the dissolution of CS ceramics was decreased and pH value of SBF and did not change the mechanism and apatite-forming ability in SBF. Moreover, the Sr addition to CS matrix stimulated HBDC proliferation due to the low concentration range of Ca and Si ions released from material (C. T. Wu et al., 2007). However, the mechanical properties of CS-Sr composites have not been investigated for using them as a high load bearing application.

CS-HA composites were studied by some researchers (Beheri, Mohamed, & El-Bassyouni, 2013; Lin, Zhang, Zhai, Qu, & Chang, 2011; Sprio, Tampieri, Celotti, & Landi, 2009). The HA is considered to be a suitable bioceramic for bone replacement, as it closely mimics the mineral part of the bone tissue (Sprio et al., 2009). The mechanical properties of dense HA are characterized by a fracture toughness slightly below the lower limit of cortical bone (Hench, 1991; C. T. Wu & J. Chang, 2013). On the other hand, the Young's modulus is typically higher (Sprio et al., 2009) and the flexure strength is restricted to ~80 MPa (Kothapalli, Wei, Vasiliev, & Shaw, 2004). Kokubo (Kokubo, 1991) developed apatite/CS bioactive glass–ceramic with high mechanical strength, which contains apatite and β-CS as reinforcing phase in a MgO–$CaO–SiO_2–P_2O_5–CaF_2$ glassy matrix. In the apatite/CS glass–ceramics, the CS phase

consists of a silica chain structure and acts as reinforcement for the apatite crystals. In addition, the presence of CS in these composites also plays an important role in the bioactivity. Lin et al. (Lin et al., 2011) found that when the CS content in the composite increased to 30 wt. %, the proliferation rate of mesenchymal stem cells (MSCs) increased. Hence, CS/HA composites with more than 30 wt.% CS content could be capable of as load bearing, bioactive, and degradable biomaterials for hard tissue repair applications. Furthermore, they have found that once the weight ratio of CS increased, the linear shrinkage of the ceramics decreased, although the porosity increased. The bending strength increased with the increase of the CS component amount and reached ~221 MPa for 90 wt.% CS composite. The elastic modulus of the sintered samples was 14.9 GPa, which is close to that of human cortical bone. However, these mechanical improvements may be suitable for use in scaffold. Recently, Beheri et al. (Beheri et al., 2013) have reported nano sized HA and CS powders prepared by both chemical precipitation and sol‑gel methods, respectively. They used pressureless sintering method for the production CS/HA. The results showed that the hardness and compressive strength were improved with increasing the CS ratio in the composite. But, these studies have not specifically mentioned the fracture toughness of CS/HA composites, which is very important for high load-bearing applications. Additionally, it is noted that the α-CS is sintered at more than 1125 °C, while HA will be decomposed to other phase such as β-TCP and α-TCP at high temperature, which they are all biodegradable materials (Sprio et al., 2009).The high degradation of these bioceramics in physical environments can weaken the composites significantly. Hence, this type of composite can be used for non-load bearing applications. Furthermore, the degradation of β-TCP and α-TCP produced in the sintering procedure must be considered prior to biomedical application.

2.3 Properties and composites of graphenes

2.3.1 Graphene oxide

A report in 2004 by Geim and Novoselov et al. of a technique to prepare individual graphene sheets has initiated enormous scientific activity due to its unique properties (Geim, 2009). Graphene, one of the allotropes (diamond, carbon nanotube, fullerene) of elemental carbon, is a planar monolayer of carbon atoms arranged into a two-dimensional (2D) honeycomb lattice with a carbon‑carbon bond length of 0.142 nm (Geim, 2009; Geim & Novoselov, 2007). It has excellent electronic properties, good thermal stability, optical transparency, large specific surface area and outstanding mechanical strength. Graphene sheets have been applied in various biotechnologies such as bacteria inhabitation (Akhavan & Ghaderi, 2010; Tang et al., 2013), biosensing (Akhavan, Ghaderi, & Rahighi, 2012), drug delivery (L. M. Zhang et al., 2010), cellular imaging (Peng et al., 2010), cancer targeting (Robinson et al., 2011), antiviral materials (Akhavan, Choobtashani, et al., 2012) and tissue engineering (Fan et al., 2014; Liao et al., 2011; K. Zhou et al., 2012). Graphene and its functionalized derivatives can be employed to improve materials and surfaces for culturing human cells for hard and soft tissue engineering applications. Recent research has shown that graphene-incorporated tissue engineering scaffolds exhibit much better mechanical properties. Unlike the case of carbon nanotubes (CNTs), they also presented outstanding mechanical properties with the tissue engineering scaffolds. However, the biocompatibility of CNTs is still under debate due to their cytotoxic responses in organic environment, an important issue in biocompatibility tests of CNTs is their purity. Contaminants, for instance amorphous carbon or residuals of catalytic particles, may considerably influence the living environment (Kalbacova et al., 2010).

Graphene oxide has a similar layered structure to graphite. In contrast to graphite, the plane of carbon atoms in graphene oxide is heavily oxygenated bearing

hydroxyl and epoxy groups on sp^3 hybridized carbon on the basal plane, which not only expand the interlayer distance but also makes the atomic-thick layers hydrophilic. Therefore, these oxidized layers could be exfoliated after sonication in water. If the exfoliated sheets have only one or a few layers of carbon atoms like graphene, these sheets are named graphene oxide (GO) (S. Pei & Cheng, 2012). Graphene oxide is readily prepared through the oxidation of graphite using oxidants including concentrated sulfuric acid (H_2SO_4), nitric acid (HNO_3) and potassium permanganate ($KMnO_4$) based on Hummers method (Huang, Lim, Chia, Yarmo, & Muhamad, 2011).

The restricted solubility of graphene in biologically relevant media limits its application in biology. On the contrary, Graphene Oxide, consisting of chemically exfoliated graphene sheets, is highly dispersible in biological media due to the presence of oxygenated functional groups (carboxyl, epoxide, and hydroxyl groups) (Das et al., 2013). However, recent studies have demonstrated concentration-dependent toxicity of graphene oxide and graphene in human erythrocytes and skin fibroblasts. Involvement of the reactive oxygen species generated by GO was proposed as one of the main mechanisms for the cytotoxicity of GO at high concentrations in neural phaeochromocytoma-derived PC12 and A549 cells, even though some evidences about cell apoptosis of the former were also reported (Akhavan, Ghaderi, & Akhavan, 2012; Das et al., 2013). Interestingly, the GO can be reduced to graphene sheets by eliminating the oxygen-containing groups with the recovery of a conjugated structure (S. Pei & Cheng, 2012).

2.3.2 Reduced graphene oxide

Reduced graphene oxide (rGO) has attracted considerable interest, which partly restores the structure and properties of graphene. Different reduction methods result in different properties of rGO, which in turn affect the final performance of materials or devices composed of rGO (S. Pei & Cheng, 2012). There are three fundamentally

different reduction techniques of GO, generally chemical, thermal and electrochemical reduction (Pumera, 2013). These three techniques can generate rGO with a fairly perfect structure and good properties (S. Pei & Cheng, 2012). Recently, several researchers have proposed the use of hydrothermal method for the reduction of GO to rGO (Pumera, 2013; J. F. Shen et al., 2011). The main advantage of using hydrothermal is that this is an effective route for the synthesis and crystallization of organic–inorganic oxide materials and simultaneously GO is reduced to rGO under the hydrothermal condition (Mo, Lei, Sun, & Rooney, 2014; J. F. Shen et al., 2011). Zhou et al. (S. F. Pei, Zhao, Du, Ren, & Cheng, 2010) reported GO reduction via a water-only route by hydrothermal treatment of GO solutions. The results demonstrate that the water not only partly eliminates the functional groups on GO, but also recovers the aromatic structures in the carbon lattice. It was found that a basic solution (pH = 11) yields a stable rGO solution while an acidic solution (pH = 3) results in aggregation of rGO sheets, which cannot be re-dispersed even in a concentrated ammonia solution (S. F. Pei et al., 2010).

Regarding toxicity of rGO and its related materials, Hu et al. (W. Hu et al., 2010) reported that rGO inhibit bacterial growth with minimal toxicity to human alveolar epithelial A549 cells. Agarwal et al. tested the biocompatibility of rGO with human fetal osteoblast (hFOB) cells, human oligodendroglia (HOG) cells and rat pheochromocytoma (neuroendocrine cell, PC12) cells and found that rGO is biocompatible with all the cells tested (Agarwal et al., 2010). Akhavan et al. (Akhavan, Ghaderi, & Akhavan, 2012) proposed that the rGO sheets have no significant effects on genotoxicity in the human mesenchymal stem cells (hMSCs). However, they found that interaction of rGO with stem cells and probably other biological systems such as organisms and tissues strongly depends on the lateral size of the sheets (average dimension of sheets).

2.3.3 Graphene nanoplatelets

Graphene nanoplatelets (GNP) are multi-layer particles consisting of 10–30 sheets of graphene with a strong retention of single-layer properties (Basavaraja, Noh, & Huh, 2013). The use of GNP may become more attractive as they are cheaper and easier to fabricate than single layer graphene (A. Nieto, Lahiri, & Agarwal, 2012). The major challenges in composite synthesis are the homogeneous dispersion and efficient use of the secondary phase. GNP is easier to disperse than single layer graphene in the matrix of composites (A. Nieto et al., 2012). In addition, single layer graphene has a tendency to curl during dispersion. Graphene is generally promising for strong interfacial bonding with the matrix because it has a very high surface energy due to the high surface area intrinsic to its geometry. In comparison with GO, GNP has a slightly lower relative specific surface area; nevertheless it is still considerably higher than those of CNT. There are four techniques for producing GNP in significant quantities: chemical reduction of graphene oxide in colloidal suspension, epitaxial growth on silicon carbide, growth on metal substrates and chemical vapor deposition (CVD) of graphene powder (Suk, Piner, An, & Ruoff, 2010). Recent studies have shown that GNP and GNP-based composites possess a series of merits, e.g., they are non-toxic for human osteoblasts and mesenchymal stromal cells (Kalbacova et al., 2010), suitable for adhesion and proliferation of osteoblasts (W. Hu et al., 2010) and have excellent antibacterial property (Akhavan & Ghaderi, 2010).

2.3.4 Graphene reinforced ceramic composites

A number of studies have reported on the use of graphene to reinforce the mechanical properties of metals/alloys, polymer and ceramic matrix composites (W. Hu et al., 2010; Yadhukulakrishnan et al., 2013). The application of graphene in ceramic composites has been proposed due to their unique mechanical properties and the interesting biological properties. Although ceramics have high stiffness and excellent

thermal stability with low density, their brittleness impedes the use as structural materials. The introduction of graphene in ceramics was proposed and used to increase the toughness as well as the elastic strength of ceramic composites. However, a key reason why processing graphene reinforced free-standing ceramic composites has been restricted is the thermal stability limitations of graphene at high temperature. Generally, ceramics have a tendency to densify and sinter at temperature over 1000 °C, hence making it challenging to incorporate graphene which has low thermal stability at temperatures in excess of~600 °C (Walker et al., 2011). Therefore, the sintering cannot be carried out in ambient furnace atmospheres. Nieto et al. used SPS to consolidate pure GNP as a bulk structure to study the feasibility of its structure retention at extreme processing conditions (A. Nieto et al., 2012). Their findings indicate that the GNP survived after SPS sintering at an extreme temperature of 1850 °C and a pressure of 80 MPa with minimal damage to the structure. Recently, Rafiee et al. (Rafiee et al., 2010; Walker et al., 2011) have shown that graphene reinforcement in ceramic-matrix composites can provide an excellent toughness, inhibiting the crack propagation and improving mechanical properties. They were the first to report the use of graphene to enhance the toughness of bulk silicon nitride (Si_3N_4) ceramics (Walker et al., 2011). They used CTAB as a surfactant to disperse the GNP into the ceramic matrix. Their results indicated that the GNP was well dispersed between the Si_3N_4 particles. After sintering at 1650 °C by SPS, GNP still existed in the Si_3N_4 matrix, which showed that GNP were stable after sintering at 1650 °C in the Si_3N_4 matrix. The fracture toughness of spark plasma sintered GNP reinforced Si_3N_4 composites increased with increasing of the volume percentage of GNP. Later on, the fabrication of graphene reinforced Si_3N_4 matrix was studied by other researchers (Ján Dusza et al., 2012; Hvizdoš, Dusza, & Balázsi, 2013; Kvetková et al., 2012; Ramirez et al., 2014; Ramirez & Osendi; Tapasztó et al., 2011). Ramirez et al. investigated the effect of the rGO and GNP on the

toughness, strength, hardness and elastic modulus of Si_3N_4. Their studies showed that the rGO/Si_3N_4 composites had a maximum toughness of 10.4 MPa $m^{1/2}$ at 4.3 vol.% rGO content. This value corresponds to a 135% increase when compared to the Si_3N_4 matrix, and it was accompanied by a 10% increase in strength. They have reported that when GNPs were used, the toughening effect was more modest (40% increase) and the strength did not increase, possibly because of the lower degree of exfoliation and the occurrence of weak interactions between the GNP and the Si_3N_4 matrix (Ramirez et al., 2014). Kvetkova et al. have studied different types of GNP with the aim to improve the fracture toughness of Si_3N_4 (Kvetková et al., 2012). They have found that multilayer graphene nanosheets show better fracture toughness in the graphene/ Si_3N_4 system (9.92 MPa $m^{1/2}$) than other GNP reinforcement into Si_3N_4 ceramics. In addition, the toughening mechanisms were similar in all composites, and were in the form of crack bridging, crack deflection, and crack branching. One of the main objectives for adding graphene into Si_3N_4 is to improve its wear resistance. Hvizdoš et al. tested silicon nitride with addition of 1 and 3 wt% of various types of GNP by means of the ball-on-disk method with a Si_3N_4 ball used as the tribological counterpart at room temperature in dry sliding (Hvizdoš et al., 2013). They found that GNP can be integrated into the matrix very strongly and did not participate in the lubricating processes. They have suggested that 3 wt% of larger sized GNP gave the highest wear resistance. Tapasztó et al. used two different sintering methods (SPS and HIP) for GNP/ Si_3N_4 composites to prepare dense materials (Tapasztó et al., 2011). Their comparisons show that the samples sintered by the SPS method are significantly harder and stiffer, whereas the composites prepared by HIP technique provide tougher composites.

Fan et al. were among the first to prepare fully dense GNP/Al_2O_3 composites from ball milled expanded graphene and Al_2O_3 by SPS method (Y. Fan et al., 2010). The GNP after ball milling is 2.5–20 nm in thickness and homogeneously dispersed in

the Al_2O_3 ceramic matrix. The percolation threshold of the as-prepared GNP/Al_2O_3 composites is around 3 vol. %. Moreover, the electrical conductivity of spark plasma sintered GNP reinforced Al_2O_3 composites increased with the increase of the volume percentage of GNP. Wang et al. used SPS to prepare rGO/Al_2O_3 composite and a 53% increase in fracture toughness was obtained with the addition of 2 wt% of rGO and also improved the electrical conductivity (K. Wang, Wang, Fan, Yan, & Wei, 2011). They reported that improvement in the dispersing property of rGO and enhancement of the mechanical properties of Al_2O_3 ceramic can be obtained by the electrostatic attraction between GO and Al_2O_3 powders and subsequent reduction and sintering. An interesting study about the effect of GNP on the microstructure and mechanical properties of the Al_2O_3 based ceramic composites has been carried out by Liu et al (Jian Liu et al., 2013). Their findings suggest GNP dispersed in Dimethylformamide (DMF) and then mixed with Al_2O_3 in a ball milling process as a suitable process for dispersing GNP. The fracture toughness of the GNP/Al_2O_3 composites increased when the GNP content increased from 0 to 0.78 vol%. The fracture toughness of GNP/Al_2O_3 composites with 0.78 vol% of GNP was improved by 27.20% in comparison with monolithic Al_2O_3 ceramics. A further increase in the volume fraction of GNP, led to increased porosity, and adversely affected the flexure strength and fracture toughness because of pores working as fracture initiation sites (Jian Liu et al., 2013). However, most recently, Porwal et al have shown that well dispersed suspensions of GNP can form a percolation network in the Al_2O_3 matrix at very low loadings of graphene (Harshit Porwal et al., 2013). they obtained an improvement of ~40% in the fracture toughness of the composites prepared with the addition of only 0.8 vol% GNP. The GNP was anchored in between the grains of alumina and severed toughening mechanisms were detected including graphene pull out, crack branching, crack deflection and crack bridging.

Liu et al. fabricated graphene platelet/zirconia-toughened alumina (GNP/ZTA) composites sintered by SPS at different temperatures (J. Liu, H. Yan, M. J. Reece, & K. Jiang, 2012). GNP was first dispersed in DMF and sonicated for 1 h and ZTA powder was added then and the mixture was further sonicated. Afterwards, GNP/ZTA powder mixtures were prepared by ball milling using zirconia balls as the milling media. They have shown that the sintering temperature in SPS processing is also found to have a direct effect on the fracture toughness of the GNP/ZTA composite. They have reported that the addition of only 0.81 vol% GNP into ZTA composites resulted in a 40% increase in fracture toughness after sintering at 1550 °C. Lower sintering temperature (1450 °C) leaves significant porosity, however, when sintering temperature rises from 1450 to 1550 °C, both the density and the hardness increase significantly. Once the sintering temperature reaches 1650 °C, a slight decrease in density, hardness and toughness were observed, which may be attributed to weight loss of GNP at the higher sintering temperature.

As regards the hydroxyapatite based composites, Liu et al. investigated the in situ HA/rGO synthesized by a liquid precipitation approach followed by SPS consolidation (Y. Liu et al., 2013). The hardness, elastic modulus and fracture toughness of spark plasma sintered HA/rGO composites increased with increasing of the 1% weight percentage of rGO. The fracture toughness of HA/rGO composites reached 3.94 MPa $m^{1/2}$, showing a 203% increase compared to pure HA. Improvement of elastic modulus in HA/rGO system is due to the high elastic modulus of rGO and good bonding at HA/rGO interface. They have reported that the presence of rGO in HA is able to improve bone cell proliferation and ALP activity (Fan et al., 2014). In the case of ALP activity assay, the level on the HA–1.0 wt% rGO composites is about 2 times of that on the pure HA. The unobvious correlation between the graphene dose and the changes in ALP activity is claimed to cause better differentiation states of the osteoblast

cells. Zhang et al. studied the effects of GNP on the properties of HA composites and reported an 80% increase in fracture toughness over pure HA (L. Zhang et al., 2013). They also reported that hardness and elastic modulus increased by 30% and 40%, respectively, using GNP as compared to pure HA. They have investigated a 7 day incubation period for apatite precipitation on GNP/HA composites when immersed in standard SBF. This study indicates that the presence of GNP reinforced HA composite ceramic should not have a negative effect on its apatite formability. Moreover, HA is reinforced with GNP, the surface of the composite is supposed to not only have more defects, but also cause a change in nanoscale topography because of the presence of obvious wrinkled texture surface of GNP. As a result, the added GNP can be perceived by osteoblasts as extra appropriate locations to adhere, leading to the improved osteoblast adhesion on the GNP/HA composites (L. Zhang et al., 2013).

These results show that the dispersion of graphene in a ceramic matrix plays an important role in the fabrication process of graphene-ceramic composites.

2.4 *In-vitro* Assessment of Biocompatibility

It is known that the implantation of biomaterials into a living organism causes specific reactions in the biological environment. Therefore, prior to clinical testing, it is mandatory to perform an appropriate biochemical screening assays at the cellular and molecular level, to address the issues of biocompatibility and long term performance of the implants. Furthermore, for *in-vitro* studies, the selection of cell types representing the target tissue is important. For example, neuroblastoma cells and Schwann cell lines can be used to evaluate the *in-vitro* cytotoxicity of materials used for nerve regeneration (S. Jain, Sharma, & Basu, 2013). Keratinocytes or fibroblasts can be applied for determining the cytotoxic potential of wound dressing materials (Wilson, Mills, Prather, & Dimitrijevich, 2005). For orthopedic implant materials, human fetal osteoblast or osteosarcoma cell lines can be used to check the cellular compatibility (Tripathi & Basu,

2012). Over the years, it has been documented that the direct use of cell and colony counting as an assay end-point is probably the least reliable method (Thrivikraman, Madras, & Basu, 2014). There are several cytotoxic assays such as MTT 3-(4, 5-dimethylthiazol-2-yl)-2, 5-diphenyltetrazolium bromide, MTS 3-(4, 5-dimethylthiazol-2-yl)-5-(3-carboxymethoxyphenyl)-2-(4 sulfophenyl)- 2Htetrazolium, XTT (sodium 2,3,-bis (2methoxy-4-nitro-5-sulfophenyl)-5-[(phenylamino)-carbonyl]-2H tetrazolium), LDH (lactate dehydrogenase), AlamarBlue® and so on. The MTT assay is a colorimetric assay for assessing cell viability based on the reduction of light absorbing substrates (Kroll et al., 2011). It is useful in the measurement of cell growth in response to mitogens, antigenic stimuli, growth factors and other cell growth promoting reagents, cytotoxicity studies, and in the derivation of cell growth curves. The advantages of this assay are: (1) gives a precise dose–response curve on small cell numbers; (2) simultaneous testing of different parameters can be done; (3) simple; and (5) the high reproducibility.

2.5 Summary

Presently, the implants employed in load-bearing applications are typically made of titanium, titanium alloy and bioinert ceramics which have higher mechanical strength than bioactive ceramics, but lower bioactivity. Bioactive ceramics have been coated on implants made of titanium and its alloys implants in order to improve bioactivity of the titanium alloy implants. Nevertheless, in many cases, the adhesion of the coating is not strong enough, and the "drop-off' of the coating causes detrimental effects (Cheng et al., 2008; X. Liu et al., 2008). Thus, extensive research has been performed to improve bioactive ceramics for use in load-bearing conditions. CS has been considered to be the most promising for this application. The significant disadvantage of CS is its inherent brittleness. For this purpose, various materials such as bioinert ceramics were reinforced into CS ceramic matrix to improve its mechanical

properties. Nevertheless, the bioactivity of CS composites would be diminished with increasing amounts of bioinert reinforcing phases introduced into the CS matrix (Kokubo, 1991; Simitzis & Baciu, 2012).

In this project, we first intend to synthesize calcium silicate hydrate powders by employing a tip ultrasonic irradiation in water solvent containing precursor salts. Initially, the effect of UI time on morphology, crystallite sizes and lattice strain of the obtained powders was analysed. The anionic surfactant SDS was then used in order to investigate the influence on the assembly of the nanosheets and crystallite sizes.

Graphene has recently provided a new inspiration for researchers to fabricate reinforced composites (Ramirez & Osendi; L. Zhang et al., 2013). In the present work, we determined the mechanical properties and biological performance for CS composites containing graphene from two different sources: commercial pristine GNP and rGO. We first report a simple hydrothermal method to synthesize CS nanowires on reduced graphene oxide sheets. CS and CS/rGO composites are densified using HIP. The variation of the mechanical properties of CS/rGO composites with respect to the amount of rGO in the matrix has been systemically investigated. The effect of rGO content on the formation of HA on CS/rGO composites during soaking in a biomimetic system of simulated body fluid (SBF) were also evaluated. In addition, detailed in vitro experiments were performed such as cell adhesion, cell proliferation (MTT) and bone cell differentiation (ALP) experiments to explore the ability of such materials to be successfully used in biomedical applications. In the next investigation, CS and GNP/CS composites are produced using hot isostatic pressing (HIP), and the mechanical properties of the sintered samples and apatite formation in a simulated body fluid (SBF) are evaluated. Moreover, *In vitro* study was used to investigate the influences of GNP reinforced CS on bone cell–materials interactions.

CHAPTER 3

MATERIALS AND METHODS

3.1 Introduction

This section presents the synthesis, fabrication process, characterization, evaluation of mechanical properties, soaking in simulated body fluid and *in-vitro* biocompatibility of composites. The methodology adopted in this research is shown in Figure 3.1.

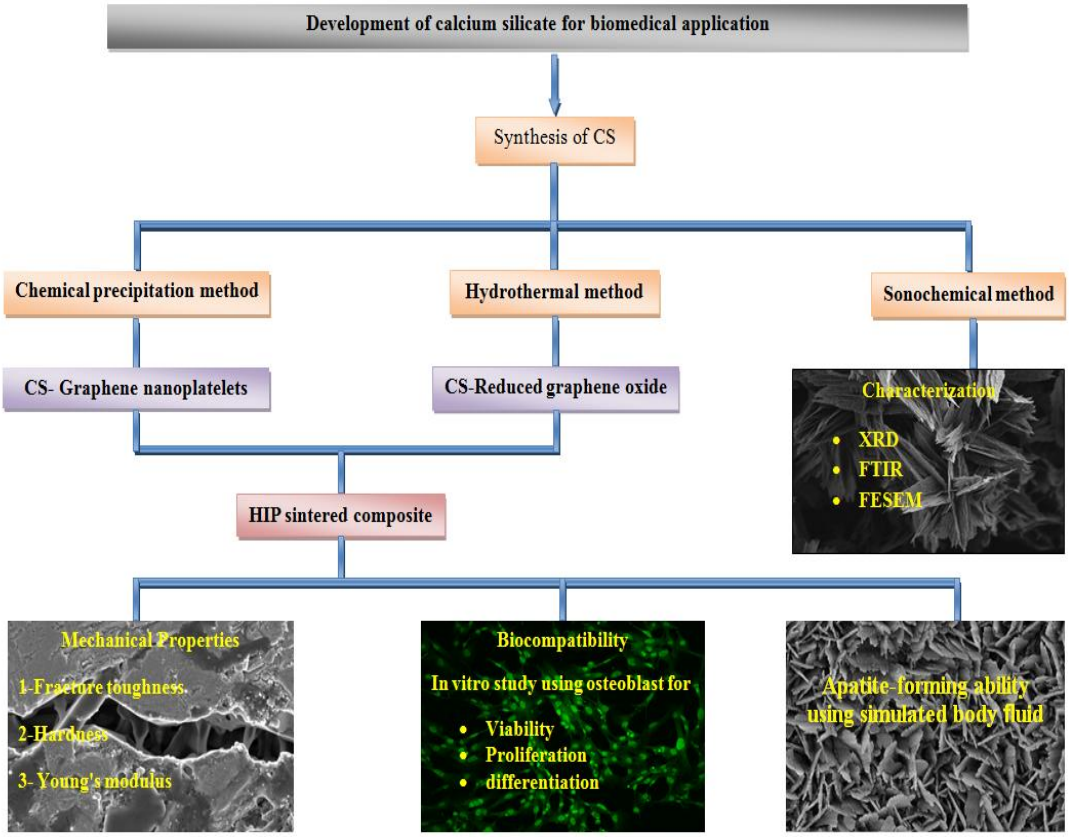

Figure 3.1: Methodology flowchart

3.2 Synthesis of calcium silicate hydrate by sonochemical method

The process of synthesizing calcium silicate hydrate by applying the ultrasonic assisted approach is depicted in Figure 3.2.

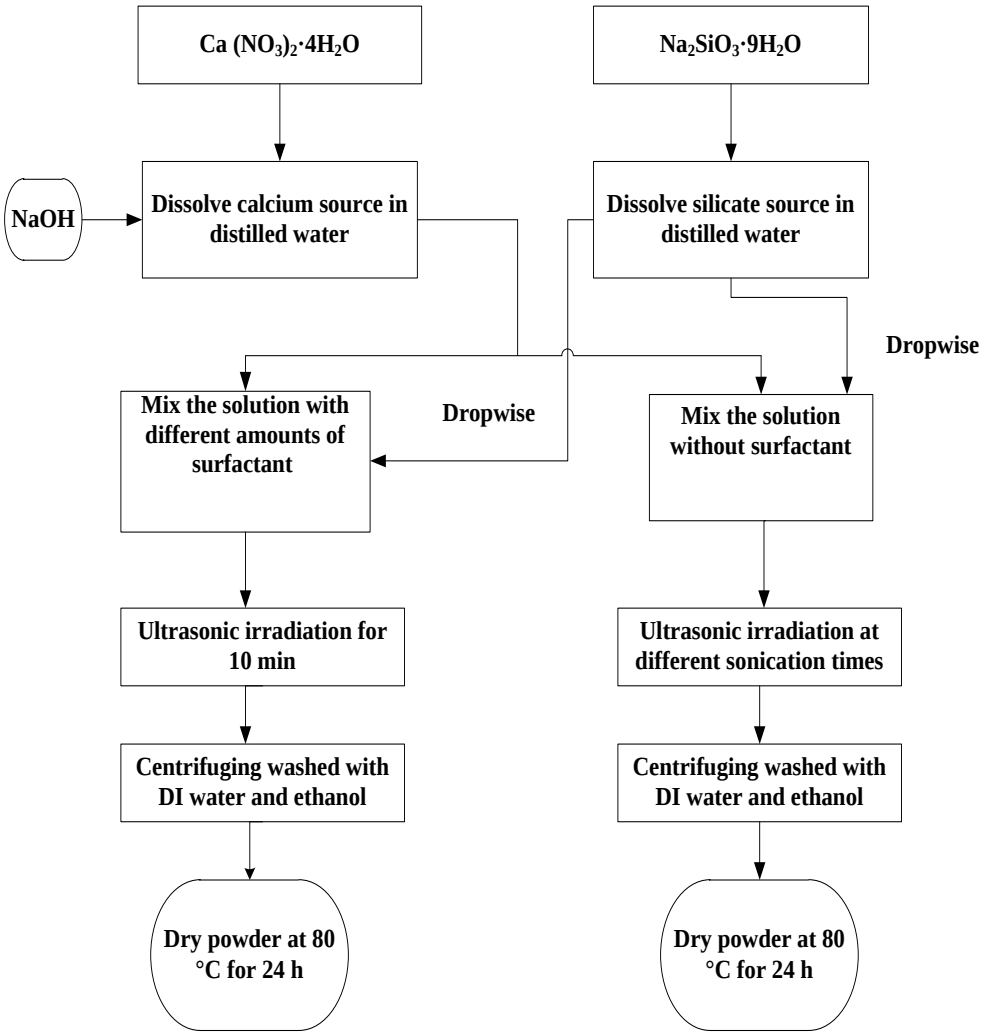

Figure 3.2: Ultrasonic assisted process for synthesis of calcium silicate hydrate

3.2.1 Selection of reagents

Many chemicals can be used as original reactants in the synthesis process of CSH and CS. Generally, Ca $(NO_3)_2 \cdot 4H_2O$, $CaCl_2$, Ca $(OH)_2$ have been used as the source of calcium (Ca^{2+}), and Na_2SiO_3 and Si $(OC_2H_5)_4$ (TEOS) have been used as the source of silicate (SiO_3^{2-}). The most important step in the whole experimental process is a suitable choice of reactants. Several factors must be considered: firstly, the spare anions from the calcium reagent and the cations from silicate should not react with each other to form precipitates. Secondly, the ions should be easily washed from the CS precipitate. Thirdly, the anions from the calcium reagent and the cations from the

silicate should not substitute Ca^{2+} and SiO_3^{2-} in the CS particles. Finally, all the elements from the reagents and solutions should not be toxic or hazardous.

In the synthesis process of CS, calcium nitrate calcium nitrate (Ca $(NO_3)_2 \cdot 4H_2O$) (BioReagent) and sodium metasilicate nonahydrate ($Na_2SiO_3 \cdot 9H_2O$) (BioReagent) supplied by Sigma-Aldrich Ltd were used as the original reagents. The spare ions of NO_3^- and NH_4^+ do not form precipitates, and it is easy to wash them away.

3.2.2 Selection of surfactant

Surfactants, as amphiphilic molecules with a hydrophobic tail and a hydrophilic head, can self-assemble to form micelles as soon as their concentration exceeds the critical micelle concentration. At a certain concentration and pH, micelles with a specific shape are formed and act as nucleation centres for crystal growth (Shanthi et al., 2009; M. Zhang & Chang, 2010). The anionic surfactant sodium dodecyl sulfate (SDS) was the used in this experiment, in order to investigate the influence on the particle growth direction and crystallite sizes. The SDS was procured from Sigma Aldrich Ltd.

3.2.3 Ultrasonic irradiation synthesis process

The calcium silicate hydrate samples for the present study were synthesized by the reaction of calcium nitrate (Ca $(NO_3)_2 \cdot 4H_2O$) and sodium silicate ($Na_2SiO_3 \cdot 9H_2O$). 15 ml of 0.1 ml Ca $(NO_3)_2 \cdot 4H_2O$ with a pH of 11.5 adjusted with NaOH, and 15 ml of 0.1 ml $Na_2SiO_3 \cdot 9H_2O$ were mixed and the solution was stirred to obtain a homogeneous solution at room temperature for 10 min. The ultrasound apparatus was a Sonic Vibra Cell Ks-1220 model (20 kHz, 1200 W) using a direct immersion titanium horn. The sonic horn was dipped into the solution in order to initiate ultrasonic irradiation at different sonication times (5, 10, 15 min) under ambient conditions. Finally, the product was separated from the solution by centrifuging at 6000 rpm,

washed with DI water and ethanol, and dried in a controlled humidity chamber at 80 °C for 24 h. For comparison, a parallel experiment was also performed by mechanical stirring at the same condition such as temperature, pH, etc., in the absence of ultrasonic irradiation.

To study the effect of surfactant micelles, different amounts of SDS (0.1, 0.2 and 0.3 g) were added in 15 ml of 0.1 ml $Ca(NO_3)_2 \cdot 4H_2O$ with a pH of 11.5 adjusted by sodium hydroxide (NaOH) and stirred for 10 min. Afterwards, 15 ml of 0.1 ml $Na_2SiO_3 \cdot 9H_2O$ was slowly added into the same beaker. The solution was sonicated for 10 min at room temperature. For comparison, detailed information for each prepared powder is given in Table 3.1.

Table 3.1: Summary of synthesis conditions and the yields obtained.

	Sample	Ultrasonic Power (%)	Time (min)	Temperature (°C)	SDS Concentration (g)	Yield (%)
G1-Group	S1	70	5	80	-	73
	S2	70	10	85	-	82
	S3	70	15	90	-	84
G2-Group	S4	70	10	85	0.1	85
	S5	70	10	85	0.2	91
	S6	70	10	85	0.3	92

3.2.4 Microstructure and phase analysis

As mentioned in the literature review, the critical characteristics of CSH and CS particles, such as biocompatibility, stability, heat-insulating ability, low dielectric loss at high frequency and mechanical properties of calcium silicates, depend strongly on their microstructure mainly their morphology, stoichiometry, crystallographic structure and

phase purity. Hence, the control over the morphology of CSH is of great importance for biomedical and industrial applications. However, when one considers the nano or micro powder, the morphology and dimensions of particles seem to be highlighted more than other characteristics (Lin et al., 2006; L. Z. Pei et al., 2010; Jin Wu et al., 2010; M. Zhang & Chang, 2010). In this study, the morphology of the synthesized powders was studied by means of field emission scanning electron microscopy (FESEM, CARL ZEISS-AURIGA 60).

In order to assess the phase of the synthesized powder, it was characterized by X-ray diffactometry (CuK_{α} radiation on an Analytical Empyrean diffractometer) to confirm the formation of the correct CSH structure. The current generated in the diffractometer was 30 mA with a voltage of 45 kV. The diffraction range was $2\Theta=20^{\circ}$-60° at 0.1°/S.

3.2.5 Characterization of crystal size and lattice strain of CSH

An ideal crystal would extend infinitely in all directions; thus, no crystals are perfect due to their finite size. This deviation from perfect crystallinity leads to a broadening of the diffraction peaks. The two main properties extracted from peak width analysis from X-ray diffactometry are the crystallite size and lattice strain. Crystallite size is a measure of the size of coherently diffracting domains. The crystallite size of the particles is not generally the same as the particle size due to the formation of polycrystalline aggregates (Khorsand Zak, Abd. Majid, Abrishami, & Yousefi, 2011). Lattice strain is the ratio of atomic interplanar distance of a strained (distance between parallel planes of atoms or ions) to a non-strained specimen.

In this project, the crystallite sizes and lattice strains were determined using the size strain plot (SSP) method. In cases of isotropic line broadening, the size-strain plot method (SSP) is one of the methods used for determining average crystallite size and lattice strain (Khorsand Zak et al., 2011). This method has the advantage of giving less

weight to data from reflections at high angles, where the precision is generally lower(Tagliente & Massaro, 2008). The size-strain plot equation that determines crystal size and lattice strain is:

$$(d_{\mathrm{hkl}}\,\beta_{\mathrm{hkl}}\cos\Theta)^2 = \frac{K}{D}\left(d_{\mathrm{hkl}}^2\,\beta_{\mathrm{hkl}}\cos\Theta\right) + (\frac{\varepsilon}{2})^2 \quad (3.1)$$

where d_{hkl} is the lattice distance between the (hkl) planes, β_{hkl} is the peak width in radian. K, D, ε and Θ are the constant $(\frac{4}{3})$ for non-spherical particles, crystallite size, lattice strain, and half diffraction angle, respectively.

When $(d_{\mathrm{hkl}}\,\beta_{\mathrm{hkl}}\cos\Theta)^2$ is plotted versus $\left(d_{\mathrm{hkl}}^2\,\beta_{\mathrm{hkl}}\cos\Theta\right)$for the all orientation peaks of CSH, the crystallite size is determined from the slope of the linearly fitted data, and the root of the y-intercept gives the strain.

3.2.6 The yield (S) of the CSH powders

The yields of CSH powders with different periods of times and various surfactant concentrations after drying was calculated by the following equation (Zou, Lin, Chen, & Chang, 2012):

$$s = \frac{m}{m_T} \times 100\% \quad (3.2)$$

where m and m_T are the practical and theoretical quantity (g) of the obtained CSH powders.

3.2.7 Structural analysis using fourier transform infrared spectroscopy (FTIR)

Fourier transform infrared spectroscopy (FTIR) was conducted on CSH powders to identify chemical bonds in the powder by producing an infrared absorption spectrum. Moreover, FTIR is an effective analytical instrument for detecting functional groups and characterizing covalent bonding information. The FTIR spectra were obtained using a Perkin Elmer-spectrum100 model FTIR. Transmittance data for all the samples were collected within the range of 400 to 4000 cm^{-1} at a resolution of 4 cm^{-1}.

3.3 Calcium silicate-reduced graphene oxide composites

A simple hydrothermal method to synthesize CS nanowires on reduced graphene oxide sheets. CS and CS/rGO composites are densified using HIP is first described. The variation of the mechanical properties of CS/rGO composites with respect to the amount of rGO in the matrix has been systemically investigated. The effect of rGO content on the formation of HA on CS/rGO composites during soaking in a biomimetic system of simulated body fluid (SBF) were also evaluated. In addition, detailed *in vitro* experiments were performed such as cell adhesion, cell proliferation (MTT) and bone cell differentiation (ALP) experiments to explore the abilities of such materials to be successfully used in biomedical applications. The framework for studying the CS/rGO composites is shown in Figure 3.3.

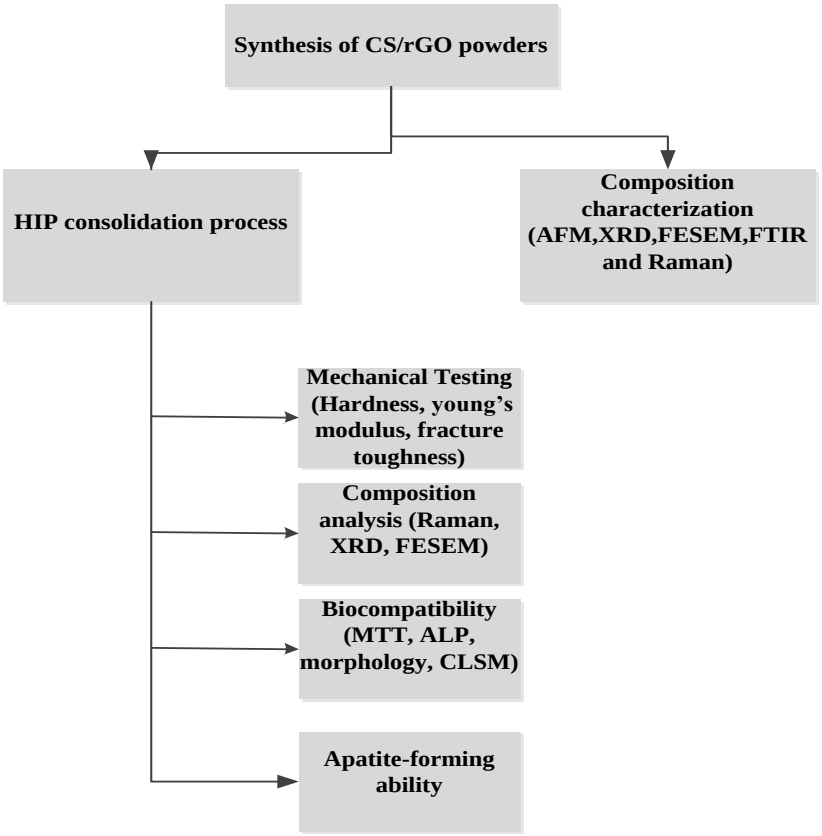

Figure 3.3: Framework for studying CS/rGO composites

3.3.1 Synthesis of graphene oxide

Graphite flakes were purchased from Ashbury Inc. Sulfuric acid (H_2SO_4, 98%), phosphoric acid (H_3PO_4, 98%), potassium permanganate ($KMnO_4$, 99.9%), hydrogen peroxide (H_2O_2, 30%), and hydrochloric acid (HCl, 37%) were purchased from Merck Company.

Graphene oxide was synthesized from graphite using a simplified version of Hummers' method (Lim, Huang, Lim, Harrison, & Chia, 2011). Graphene oxide was obtained by the oxidation of 1 g of graphite flakes which is punchers (Ashbury Inc) with 120 mL of H_2SO_4 and 13 ml H_3PO_4 and the gradual addition of 6 g of $KMnO_4$. The solution was mixed using a magnetic stirrer, and the reaction took less than 5 minutes to complete. Nevertheless, to ensure complete oxidation of the graphite, the mixture was stirred for three days. During oxidation, the color of the mixture changed from dark purplish-green to dark brown. In the final step, the suspension was cooled and diluted with 250 mL of ice. Then, H_2O_2 (30%) was added until the gas evolution ceased to ensure that residual permanganate was reduced to soluble manganese ions. The graphene oxide was repeatedly washed with dilute 1 M HCl and deionized water until a pH of 4-5 was achieved. The product was separated from the mixture by centrifugation at 11000 rpm.

3.3.2 Synthesis of CS-rGO powders

The obtained GO (208.14 mg) was ultrasonically dispersed in 40 ml distilled water for 2 h. In the first step, the GO solution was added drop-wise to 20 ml of 0.2 M Calcium nitrate tetrahydrate ($Ca(NO_3)_2 \cdot 4H_2O$) with stirring for 30 min, and the pH was adjusted to 11.5 with NaOH. Then, 20 ml of 0.2 M sodium metasilicate nonahydrate ($Na_2SiO_3 \cdot 9H_2O$) solution was added drop wise into the first solution, and the suspension was mechanically stirred for 1 h at room temperature to obtain a homogeneous suspension. In the final step, the suspension was transferred into a 60 ml Teflon-lined

stainless-steel autoclave and heated to 200 °C for 24 h, and then naturally cooled to room temperature. Both the reduction of GO to rGO and the in-situ synthesis of CS-rGO nanocomposites were expected to occur during the hydrothermal process. CS-rGO composite powders with different rGO contents (0, 0.25, 0.5, 0.75, 1 and 1.5 wt. %) were typically produced. After the hydrothermal treatment, the suspension was filtered and washed several times by centrifugation and resuspension with distilled water. The resulting powders were dried at 100 °C for 24 h.

3.3.3 Free standing CS/rGO composite synthesis: Hot isostatic pressing (HIP)

The resulting powders were ball milled for 1 h at 300 rpm by planetary ball mill and then uni-axially pressed into disks with diameters of 5 and 10 mm at a pressure of 250 MPa. These compacts were sintered to obtain α-CS by hot isostatic pressing (American Isostatic Presses, Inc.) for 1 h at 1150 °C in a high-purity argon atmosphere at 160 MPa. Heating and cooling rates were less than 5°C/min to prevent the appearance of cracks due to differences in the thermal expansion coefficients of the phases that could form during sintering. Finally, The CS and CS/rGO composite compacts were ground using progressively finer silicon carbide papers (up to 1200 grit size), and then samples were polished to a mirror finish using diamond powders of various grades from 15 to 0.25 μm in an auto polisher (laboforce-3, Struers).

3.4 Graphene nanoplatelets reinforced calcium silicate composites

In this study, GNPs with nano-scale diameters were chosen to reinforce CS ceramics. GNPs possess superior mechanical strength. Moreover, they have proven to be biocompatible materials for the human body. Uniformly networked dispersed GNPs in the CS matrix act as a reinforcing frame work of the composites.

In general, GNPs agglomerate due to their high surface energy and large aspect ratio. The distribution of the reinforcing phases in a matrix can greatly influence the performance of the composites. The reinforcing effect of GNPs decreases greatly if

GNPs are not dispersed uniformly in the matrix. In order to solve this problem, cetyl trimethyl ammonium bromide (CTAB) was used as a surfactant to disperse GNPs in the CS matrix. The framework for studying the CS-GNP composites is shown in Figure 3.4.

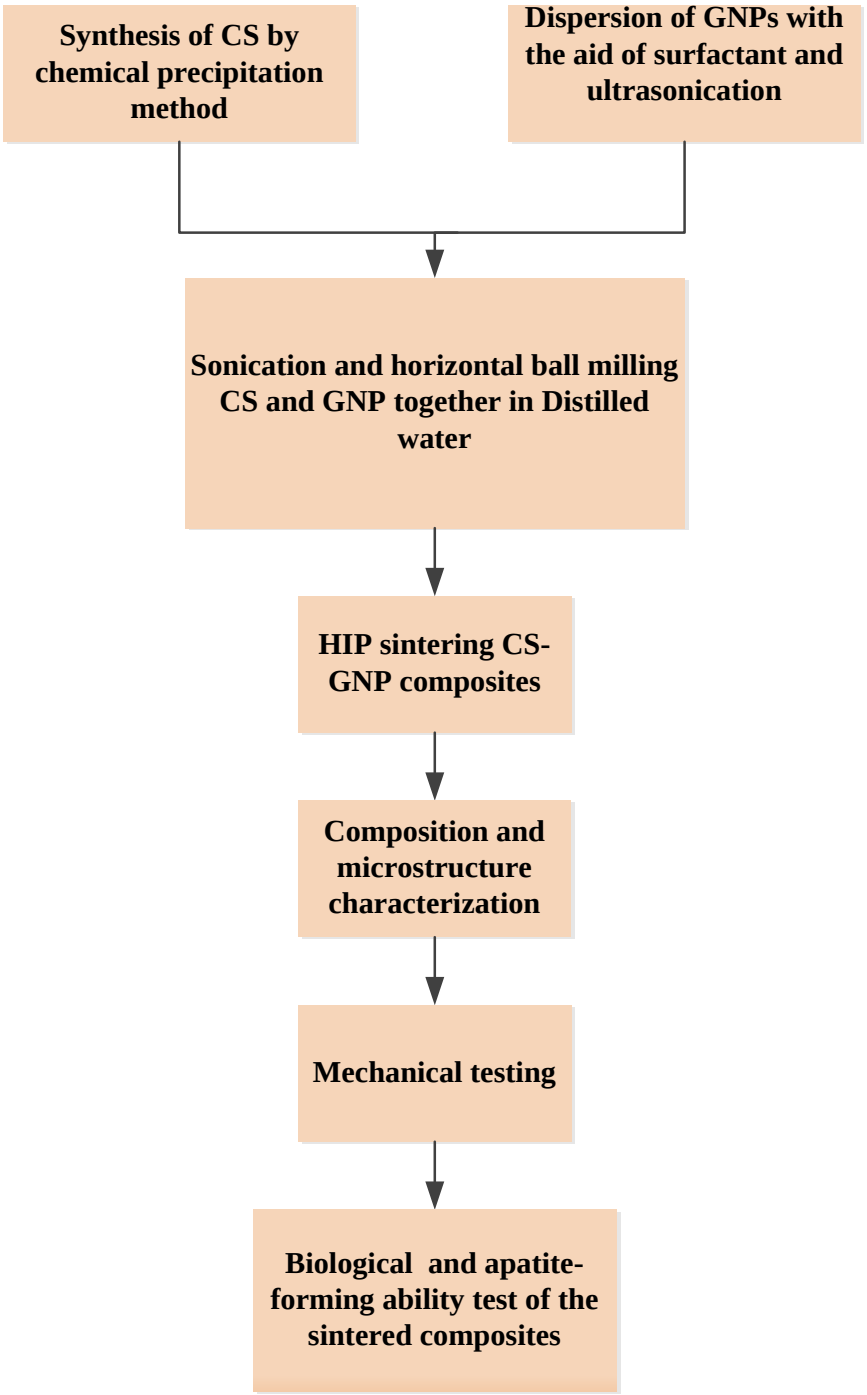

Figure 3.4: Framework for studying GNPs reinforced CS-GNP composites

3.4.1 CS-GNP composite powder preparation

Synthesis comprises of two stages; the first one, synthesis of CS powder and the second one is the mixing of the CS powders and GNPs. Calcium silicate ($CaSiO_3$) powders were synthesized through a chemical precipitation method using reagent-grade calcium nitrate (Ca $(NO_3)_2.4H_2O$) and reagent-grade sodium silicate ($Na_2SiO_3 \cdot 9H_2O$) as precursors (Sigma-Aldrich, Inc., St. Louis, MO, USA). in this experiment, 1000 ml of 0.4 mol Ca $(NO_3)_2.4H_2O$ solution with a pH 11.5 (adjusted by NaOH) was vigorously stirred at room temperature, and 1000 ml of 0.4 mol $Na_2SiO_3 \cdot 9H_2O$ was added dropwise over one hour to give a white precipitate. The white precipitate was then stirred for 12 h followed by washing several times with distilled water by centrifugation to remove $Na^+$and NO_3^- ions, and then washed two times with ethanol to improve the dispersion characteristics. After washing, the remaining liquid was removed by vacuum filtration, and the precipitate was dried at 100 °C for 24 h, calcined at 800 °C for 2 h. Finally, the powders were ball milled for 12 h to obtain a finer powder. The ratio of powder mass to the balls was 1:5. The diameter of balls was 10 mm and the material was zirconia (ZrO_2) (Retch, Germany).

Graphene nanoplatelets were obtained from XG Sciences, USA. The specification of GNPs is listed in Table 3.2. GNPs were firstly ultrosonicated for one hour in distilled water with a concentration of about 0.1 mg/ml, in which CTAB was used as dispersant. CS powder was then added and the mixture was sonicated for another 30 min. The suspension was then mixed using zirconium oxide balls (Retsch GmbH, Haan, Germany) in a horizontal ball mill (9VS, Pascall Engineering Co. Ltd, Suffolk, UK) for 12 h. The milled slurry mixture was dried at 100°C in an oven for 2 days. The chosen composites for the purpose of this study were pure CS and CS/GNP composites with GNP contents of 0.5, 1.0, 1.5 and 2.0 wt%.

Table 3.2: Specifications of the graphene nanoplatelets (GNPs).

Specific surface area (m^2/g)	500 m^2/g
Width (μm)	Less than 2 mm
Thickness (nm)	Less than 2 nm
Thermal conductivity (W/m K) Parallel to surface	3000 W/m K
Thermal conductivity (W/m K) Perpendicular to surface	6 W/m K
Electrical conductivity (S/m) Parallel to surface	10^7 S/m
Electrical conductivity (S/m) Perpendicular to surface	10^2 S/m
Theoretical density	2.2 g/cm^3
Purity	99%

3.4.2 Free standing CS/GNP composite synthesis: Hot isostatic pressing

Green bodies (5 and 10 mm diameter) of cylindrical shape were formed by uniaxial pressing at 250 MPa. The sintering procedure was completed at 1150 °C and 160 MPa pressure applied for 1 h in high-purity argon gas by hot isostatic pressing (American Isostatic Presses, Inc., USA). The heating and cooling rates did not exceed 5 °C/min. It is noteworthy that in order to eliminate the CTAB, the compacted samples were heated to 500 °C for 1h during HIP processing. The sintered samples were polished with SiC abrasive papers (up to 1200 grit size), and polished to mirror finish using diamond powder of various grades from 15 to 0.25 μm in an auto polisher (laboforce-3, Struers). The samples were also thermally etched at 1050 °C for 30 min in a muffle furnace for grain size determination.

3.5 Microstructural characterization

Characterization techniques for evaluating physical properties and microstructure of CS/rGO and CS/GNP composites are described below.

3.5.1 Field emission scanning electron microscopy (FESEM)

High-resolution FEI Quanta 200F field emission scanning electron microscopy (FESEM) was used for the characterization of powders and consolidated composites. Microscopic characterization of powders was performed by dispersing them on a silicon wafer. The consolidated samples were mounted and polished to mirror finish using diamond powder of various grades from 15 to 0.25 μm in an auto polisher (laboforce-3, Struers) for the microstructural observation through cross section. Fracture surfaces of the sintered pellets were also observed under FESEM to analyse the quality of rGO and GNP dispersion and its bonding with the CS matrix. Energy dispersive X-ray analysis (EDAX) using the EDX-System (Hitachi, S-4800) instrument was attached to the FE-SEM instrument to investigate the elemental compositions of the samples.

3.5.2 Atomic force microscopy (AFM)

Atomic force microscopy (AFM) is a very high-resolution type of scanning probe microscopy, with demonstrated resolution on the order of fractions of a nanometer. Atomic force microscopy (AFM, Veeco Dimension AFM) in tapping mode was used to show the size of GO and rGO. Tapping mode AFM operates by scanning a tip attached to the end of an oscillating cantilever across the sample surface. The advantages of using of the tapping mode are: higher lateral resolution, lower forces, less damage to the samples and lateral forces are virtually eliminated, so there is no scraping. In this experiment, the samples for the AFM imaging were prepared by drop casting a diluted suspension (0.05 mg/ml) onto a cleaned silicon substrate and drying at 50°C for 1day. The statistical analysis of the average lateral dimensions (ALDs) of GO and rGO were performed using the SPSS statistical software package version 19 (SPSS Institute, Chicago, IL), with the assistance of image analysis software.

3.5.3 High resolution transmission electron microscopy (TEM)

The powder (rGO, CS/rGO, GNP and CS/GNP) interfaces were observed at near atomic-scale under a transmission electron microscope (TEM, Zeiss Libra 120). The samples were prepared for TEM characterization by dispersing the powders in ethanol, placing it onto a micro grid and letting the solvent evaporate.

3.5.4 X-Ray diffraction

X-ray diffraction (XRD) studies were carried out to determine the CS phases present in powder and consolidated stages. The X-Ray diffraction (XRD) patterns of the powders and composites were obtained using an automated X-ray powder diffractometer (XRD, PANalytical's Empyrean) with monochromated CuK α radiation (λ=1.54056 Å), operated at 45 kV and 40 mA with a step size of 0.026 deg and a scanning rate of 0.1 deg s^{-1} in the 2θ range of 20 to 60 deg.

3.5.5 Fourier transform infrared spectroscopy (FTIR)

Fourier transform infrared (FTIR) analyses were carried out on a Perkin Elmer System 2000 series spectrophotometer (USA) in the frequency range of 4000-400 cm^{-1} to identify the functional groups of the GO, rGO and CS/rGO powders.

3.5.6 Raman spectra

Raman spectroscopy was carried out to confirm the retention of graphene structure in the synthesised powders and consolidated structure after exposure to high temperature and pressure. The Raman spectrum contains a peak for each specific type of bond present in the sample, which can be correlated with the presence of a chemical entity or compound. A shift in wave number (peak position) in Raman spectra signifies a change in the bond length and thus the stress present in material. In addition, the relative intensity of the signature peaks of graphene (D, G, 2D) denotes the defect in graphene structure. All these characteristics are taken advantage of for analysing the composite microstructure in the current research. Raman spectra of powders and

samples before and after sintering are obtained by using a Renishaw Invia Raman Microscope with laser excitation at 514 nm.

3.5.7 Density measurements

Density measurements were performed according to the Archimedes technique in water on sintered bodies. The Archimedes theorem explains that all bodies immersed in a fluid will be buoyed up by a force equal to the weight of the fluid that these displace. Green and sintered bodies' densities were calculated from the following equation:

$$\rho_1 = \frac{A}{A-B}\rho_0 \quad (3.3)$$

Were ρ_1 is density of solid body, A is the weight of the solid body in air and B is the weight of solid body when immersed in water and ρ_0 is density of water, which is $0.9998\ \frac{g}{cm^3}$ at temperature of 25°C. Also, the theoretical density was calculated from the rule of mixture (Amada et al., 1996).

3.6 Evaluation of mechanical properties

Elastic modulus, hardness, fracture toughness and brittleness index of composites were studied. Nanoindentation and microindentation techniques were used to measure mechanical properties at multiple length scales.

3.6.1 Micro-indentation: Hardness and fracture toughness

Microhardness was measured using a Mitutoyo hardness tester (model AVK-C2, Mitutoyo, Kawasaki, Japan). The hardness is a parameter of resistance to deformation of the material. The hardness is calculated with the standard formula:

$$HV = \frac{F}{A} \approx 1.8544\ \frac{F}{d^2} \quad (3.4)$$

Where *F* is the force applied to the diamond, *A* is the area of the indentation and *d* is the average value of the diagonals of the imprint created by the indentations, these are shown in Figure 3.5.

The fracture toughness of a material, in the simplest terms, can be described as the stress required to initiate a crack when a stress is applied. For brittle materials such as ceramics and bioglass, indentation test is considered as a precise procedure to evaluate the fracture toughness. The indentation method has the advantages of simplicity and economy as only a small sample area is required. Thus the technique is suited for comparative assessment (Saadaldin & Rizkalla, 2014). The fracture toughness was calculated from the equation suggested by Anstis (Anstis, Chantikul, Lawn, & Marshall, 1981):

$$K_{IC} = 0.016\left(\frac{E}{H}\right)^{1/2}\left(\frac{P}{C^{3/2}}\right) \quad (3.5)$$

where K_{IC} is the indentation toughness (MPa $m^{1/2}$), 0.016 is the material-independent constant for a Vickers radial crack, E is the elastic modulus (GPa) determined from the nanoindentation experiments, H is the Vickers hardness (GPa), P is the indentation load (N), and C (m) is the half-length of the radial cracks on the surface after Vickers indentation.

Moreover, the micro-indents at the surface of the specimens and the radial cracks generated were observed through high resolution FESEM imaging to understand the role of graphene in toughening of the composite.

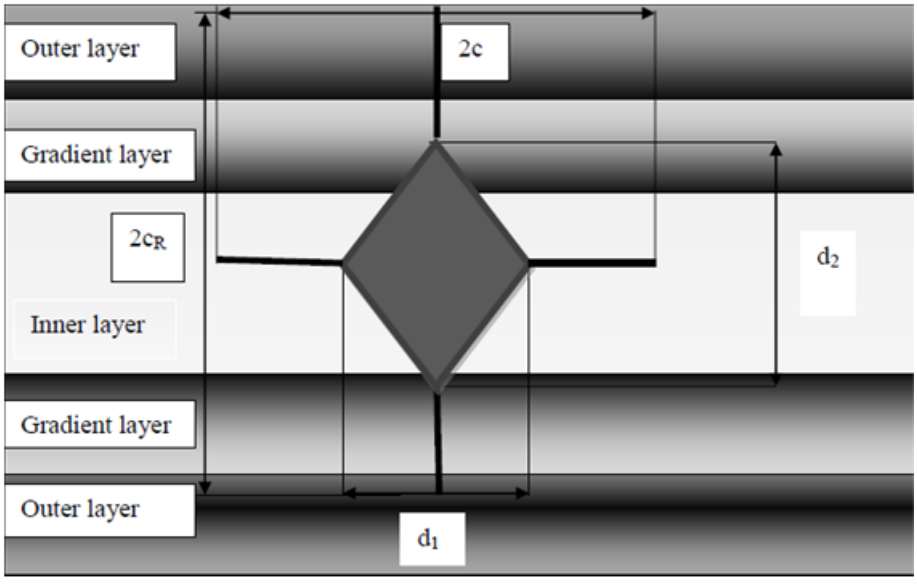

Figure 3.5: Illustration of a crack indentation measures

3.6.2 Assessment of brittleness index

Quantitative evaluation of the machinability of the GNPs/CS composites was performed by calculating the brittleness index (BI). The brittleness index has been determined by the following equation.(Boccaccini, 1997)

Brittleness index (BI): $\frac{H}{K_{IC}}$ (3.6)

In the current study, the average values of HV and K_{IC} were used for calculation.

3.6.3 Nano-Indentation: Elastic modulus and nano-hardness

Nanoindentation experiments were conducted using a nanomechanical testing system (Micro materials Ltd., Wrexham, U.K.) with a Berkovich diamond tip with a radius of 20 nm and a controlled load of 100 mN with a dwell time of 10 s. The indentation velocity was 3 nms^{-1}. At least ten indentations were made to obtain an average value for each sample. The elastic modulus was calculated through nanoindentation. The reduced modulus (E_r) is taken from the nanoindentation data and is related to the sample's elastic modulus (E_s). The equations used to calculate the sample's elastic modulus (E_s) are as follows:

$$\frac{1\text{-}\nu_s^2}{E_s} = \frac{1}{E_r} - \frac{1\text{-}\nu_i^2}{E_i} \quad (3.7)$$

The elastic modulus (E_i) and Poisson's ratio (ν_i) of the indenter are 1140 GPa and 0.07, respectively, which are taken from data sheet of machine. The Poisson ratio of the sample (ν_s) is taken to be 0.25 for the CS (Pattanayak et al., 2006).

3.7 Apatite-forming ability of composites by soaking in simulated body fluid (SBF)

The bioactivities of the fabricated composites were evaluated by examining the formation of bone-like apatite on the samples in simulated body fluid (SBF) solution,

which was prepared according to the well-known Kokubo composition (Kokubo & Takadama, 2006). The reagents used in the SBF synthesis process include: potassium chloride (KCl), magnesium chloride hexahydrate ($MgCl_2$. $6H_2O$), sodium chloride (NaCl), sodium hydrogen carbonate ($NaHCO_3$), di-potassium hydrogen phosphate trihydrate (K_2HPO_4S. H_2O), calcium chloride ($CaCl_2$), sodium sulfate (Na_2SO_4), hydrochloric acid (HCl) and tris hydroxymethyl aminomethane (Tris $(HOCH_2)_3CNH_2$), (l mol/L). All chemicals were procured from Sigma Aldrich Ltd. and used as received. 750 ml deionized water was putted into a 1000 ml plastic beaker. The deionized water was stirred and kept at 36.5 °C on a hot plate. All the reagents were dissolved one-by-one in deionized water in the sequence listed in Table 3.3. The solution was clear, with no precipitate generated during the mixing of the SBF.

Table 3.3: Reagents for preparation of SBF

Step	Reagent	Amount
1	NaCl	7.996 g
2	$NaHCO_3$	0.350 g
3	KCl	0.224 g
4	K_2HPO_4S. H_2O	0.228 g
5	$MgCl_2$. $6H_2O$	0.305 g
6	1 kmol/m^3 HCl	40 cm^3
7	$CaCl_2$	0.278 g
8	Na_2SO_4	0.071 g
9	$(HOCH_2)_3CNH_2$	6.057 g
10	1 kmol/m3 HCl	Appropriate amount for adjusting pH

After all the reagents were completely dissolved, the pH value of the solution was about 2.0. Afterward, Tris was added little by little with less than about 1g, in order to avoid local increase in pH of the solution due to the pH value increased with addition of Tris. When the pH value was about 7.45, Tris and HCl were alternately used to adjust the pH value until it settled at 7.40. After the adjustment of the pH, the solution was

transferred from the beaker to a glass volumetric flask of 1000 mL. The inside of the beaker was washed with deionized water several times before adding the solution to the flask. Finally, the total volume of the solution was adjusted to 1000 mL, and the flask shaken well. The flask was kept at room temperature until its temperature reached approximately 25 °C. Kokubo (Kokubo & Takadama, 2006) reported that the ion concentration in SBF prepared by this method would be close to that of human blood plasma, as listed in Table 3.4.

Table 3.4: Ion concentrations of the simulated body fluid and human blood plasma.

Ion	Ion concentration (mol/dm^3)	
	Simulated body fluid (SBF)	Human blood plasma
Na^+	142.0	142.0
K^+	5.0	5.0
Ca^{2+}	2.5	2.5
Mg^{2+}	1.5	1.5
Cl^-	103.0	147.8
HCO_3^-	27.0	4.2
HPO_4^{2-}	1.0	1.0
SO_4^{2-}	0.5	0.5

The as-sintered samples with a thickness of 3 mm and a diameter of 10 mm were soaked in SBF at 37 °C in a humidified atmosphere containing 5% CO_2 for 1, 3, 7 and 14 days at a surface area to volume ratio of 0.1 cm^2/mL. After various soaking periods, the samples were gently rinsed with deionized water to remove SBF, and then dried in vacuum at 80 °C. The soaked samples were characterized by XRD. The surfaces of the soaked samples were observed by FESEM. At each SBF time point, the samples were removed and the calcium (Ca) and phosphorus (P) ion concentrations in the SBF fluids were measured by inductively coupled plasma atomic emission spectroscopy (ICP-AES;

Varian, USA). Changes in the solution pH were measured by a pH meter (Eutech pH 6+ pH/ORP meter kit (YO-15940-80)). As the SBF does not contain any Si before soaking, the dissolution ratio (*S*) of CS-rGO composites at different time points was calculated by the following equation:

$$S = (c_{\mathrm{Si}}\, v_{\mathrm{S}})/m_{\mathrm{Si}} \times 100 \quad (3.8)$$

where c_{Si}, v_{S} and m_{Si} are the Si concentration in SBF (mg/ml), the volume of SBF (ml) and the Si content (mg) of the samples soaked in SBF, respectively.

3.8 *In-vitro* assessment

In this study, *In-vitro* biocompatibility of composites were assessed using human fetal osteoblastic cell line (hFOB) derived from human osteoblasts. Moreover, the proliferation of the cells cultured on the sterilized pellets was analyzed using the methyl thiazole tetrazolium (MTT) assay.

3.8.1 Cell culture test

The hFOB 1.19 cell line derived from human osteoblasts was purchased from American Type Culture Collection (ATCC, Rockville, MD). Cells were maintained and propagated in DME/F-12 (HyClone, Utah, USA) cell culture medium supplemented with 10% fetal bovine serum (Gibco, NY, USA), 100 U/ml penicillin and 100 µg/ml streptomycin at 37 °C in a humidified atmosphere with 5% CO_2. The ability of the cells to attach and proliferate on the sintered composites was examined by culturing the cells on composite samples. The sintered composite discs, 5 mm in diameter and 2 mm thick, were sterilized by autoclaving at 121 °C for 30 min under a pressure of 15 atm. Composites were then washed by sterile phosphate buffered saline (PBS) to remove all residues. In the next step, the samples were washed with the cell culture medium prior to placement in a 96-well tissue culture plate (NUNC, Denmark). Cells were seeded at 1×10^4 cells/well in wells containing composite discs.

3.8.2 Cell attachment and proliferation assay

The cells were seeded on the sterilized surfaces at 1×10^4 cells ml^{-1} in 96-well culture plates with 200 µl media in each well, and cultured for 1, 3 and 5 days. The proliferation of the cells cultured on the sterilized pellets was analyzed using the methyl thiazole tetrazolium (MTT) assay. A 5 mg ml^{-1} MTT stock solution (Sigma, St. Louis, MO, USA) was prepared by dissolving MTT in PBS and filtering with a 0.2 µm filter and was stored at 4 °C. When the 96-well plates were removed from the incubator, 20 µl of MTT stock solution were added to each well. Cells were incubated for 4 h at 37 °C in an atmosphere of 100% humidity and 5% CO_2. After incubation, the MTT solution was removed and replaced with 100 µl DMSO. At each timepoint (1, 3 and 5 days), the samples were removed to new 24-well tissue culture plates. After three washes with PBS solution, the cells were detached with trypsin/EDTA, stained with trypan blue and the living cells were counted with a hemocytometer (Becton Dickinson, Germany). Dose-response curves were plotted using GraphPad Prism 5 (GraphPad Software Inc., San Diego, CA). Three samples of each composite were tested and each test was carried out in triplicate.

3.8.3 Cell morphology

The observation of a cell–material interaction on the surface of material is an effective approach for assessing the performance of a new biomaterial (Thrivikraman et al., 2014). Cell morphology, spreading and adhesion give clear indication regarding the growth behavior and suitable cellular response to the tested material (Song, Ju, Song, & Morita, 2013). The cell–material interaction can be observed by means of a multitude of microscopic techniques, including confocal microscopy, electron microscopy and fluorescence microscopy. In this regard, to observe the cells adhering to the sample surfaces after incubation for 1, 3 and 5 days using FESEM and confocal laser scanning microscopy, the cells were fixed on the specimen surfaces with 4% glutaraldehyde for 2

h at room temperature followed by three washes in PBS (0.1 M) and dehydration with a series of graded ethanol/water solutions (40%, 50%, 60%, 70%, 80%, 90% and 3×100%, respectively). Then, 0.5 ml hexamethyldisilazane (HMDS) was added to each well to preserve the original cell morphology, and the test plates were kept in a fume hood to dry at room temperature.

3.8.4 Confocal laser scanning microscopy

The specimens were washed with 1X PBS before staining with 100 µg/ml acridine orange (Sigma Aldrich) for 5 minutes at room temperature. Excess stain was removed by washing twice with 1X PBS for 10 minutes each. The stained cells were then analyzed using confocal microscopy (Leica TCS-SP5 II, Leica Microsystem, Mannheim, Germany) and the images were processed with Leica LAS AF software.

3.8.5 Alkaline phosphatase activity assay

Alkaline phosphatase (ALP) is an ectoenzyme, produced by osteoblasts and is believed to be involved in the degradation of inorganic pyrophosphate to provide a sufficient local concentration of phosphate or inorganic pyrophosphate for the mineralization to proceed. Among various biological tests for determining osteoblastic activity on a implant, assessment of the secretion of alkaline phosphatase is an important test (Hosseinkhani, Hosseinkhani, Khademhosseini, & Kobayashi, 2007).

To assess alkaline phosphatase (ALP) activity, hFOB human osteoblast cells were seeded (3×10^3 cells/disc) onto the samples (Ø 5 × 2 mm) and incubated for 7 days. Quantitative ALP activity was measured by an assay based on the hydrolysis of p-nitrophenyl phosphate (p-NPP) to p-nitrophenol (p-NP). Cells were extracted from the samples and permeabilized using Triton X-100 (1 vol. %) solution (Sigma, USA). The cell lysate from each sample was then used for the ALP assays. The absorbance was recorded at 405 nm using a M5 SpectraMax microplate reader (Molecular Devices, Sunnyvale, CA), and ALP activity was calculated from a standard curve after

normalization to the total protein content. Data were expressed in nanomoles of p-nitrophenol produced per minute per microgram of protein. Five replicates were used, and each test was performed independently three times.

3.8.6 Statistical analysis

All data are expressed as the mean ± standard deviation (SD) and were analyzed using a one-way analysis of variance (ANOVA) and a Tukey–Kramer post hoc test. $P < 0.05$ was considered statistically significant.

3.9 Summary

Calcium silicate hydrate (CSH) has been synthesized by a tip ultrasonic irradiation (UI) method using calcium nitrate (Ca $(NO_3).4H_2O$), sodium silicate (Na_2SiO_3.9H2O) and sodium dodecyl sulfate (SDS) in water. The products were characterized by XRD, FESEM and FTIR. The size‑strain plot (SSP) method was used to study the individual contributions of crystallite sizes and lattice strain on the peak broadening of the CSH.

The hydrothermal method was used to synthesize CS nanowires on graphene oxide sheets. CS and CS/rGO composites are densified using HIP at 1150 °C. Moreover, CS ceramic composites reinforced with GNP were prepared using hot isostatic pressing (HIP) at 1150°C. The mechanical properties of the sintered samples such as hardness, fracture toughness, young's modulus and brittleness index were obtained. The apatite-forming ability of composites in a simulated body fluid (SBF) is evaluated. In addition, detailed *in vitro* experiments, such as cell adhesion, ALP and cell proliferation (MTT) are used in order to explore the capabilities of such materials to be successfully applicable as biomaterials in tissue engineering applications.

CHAPTER 4

RESULTS AND DISCUSSION

4.1 Introduction

The objectives of this research are to synthesis CSH and develop a CS based composite with similar mechanical properties to that of natural bone, and biocompatibility for use as bone replacement materials in load bearing conditions. This chapter is the nucleus of the dissertation, which presents a detailed description of the results obtained through experimentations and scientific analysis of the outcomes.

4.2 Microstructural characterizations of the CSH synthesized by ultrasonic irradiation

A tip ultrasonic irradiation in water solvent was used to synthesize calcium silicate hydrate powders. Initially, the effect of UI time on morphology, crystallite sizes and lattice strain of the obtained powders was analysed. The anionic surfactant SDS was then used in order to investigate the influence on the assembly of the nanosheets and crystallite sizes.

4.2.1 Composition characterization

As described previously, in excess of 30 crystalline CSH phases are known, and preparations made near room temperature have structures that range from semicrystalline to nearly amorphous. Moreover, CSH decomposes to β or α-CS after calcination.

Figure 4.1 shows the X-ray Diffraction (XRD) patterns of G1-Group (Table 3.1) obtained at different sonication time and in the non-sonicated sample, which coincided with the calcium silicate hydrate in the JCPDS card 03-0606. No other diffraction peaks were observed other than the main peaks that corresponded to the CSH structure. The width of the diffraction peaks becomes narrower with increasing sonication time, which

means the crystallinity of the CS particles increases with the extending of UI time. This result illustrates that ultrasonic irradiation is very effective to obtain CSH as the main phase and could promote the crystallization of CSH in a short period of time.

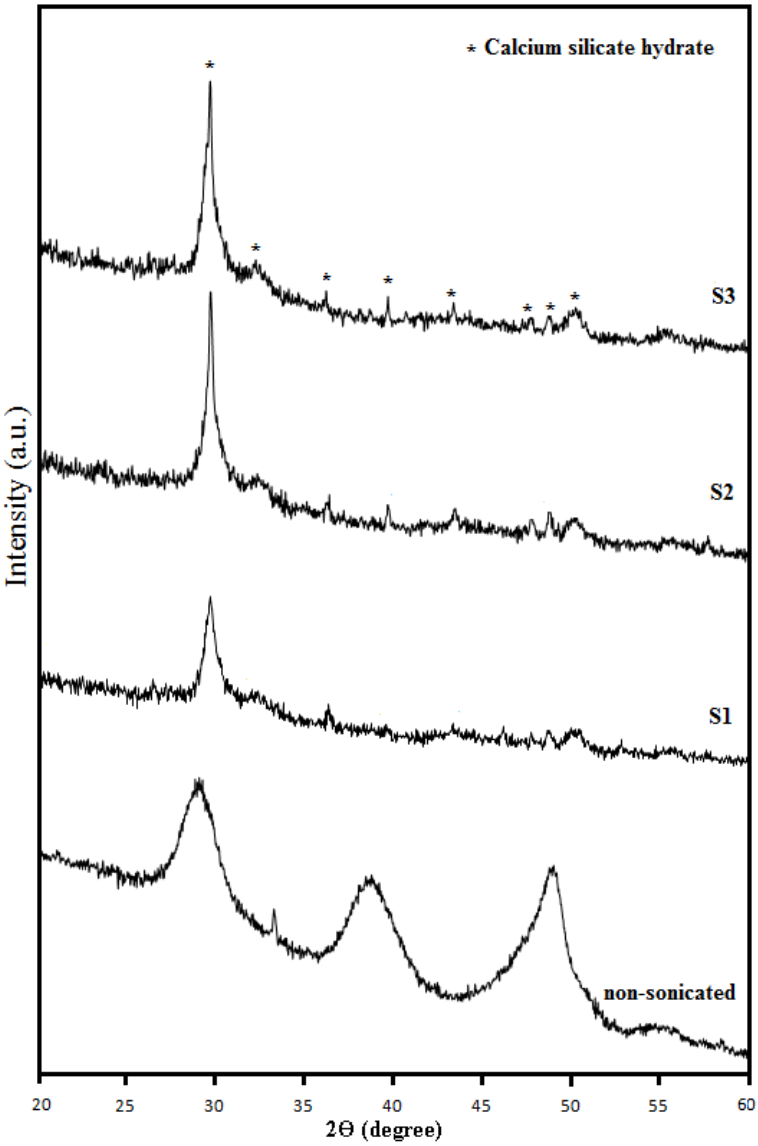

Figure 4.1: XRD pattern of synthesized CSH particles with different periods of time (S1) t =5 mins (S2) t =10 mins (S3) t =15 mins and non-sonicated powders

The experimental results show that CSH cannot be synthesized at the same conditions of concentration, time and temperature with a mechanical stirrer in the absence of ultrasonic irradiation. Due to the CSH powders synthesized by chemical precipitation method, the reaction between Ca $(NO_3)_2$ and Na_2SiO_3 need to take some

time until Ca $(NO_3)_2$ powders are completely converted to CSH. Also, the CSH produced with UI samples show rapid synthesis and suitable yield. This is surprising, because apparently most of the Ca^{2+} and SiO_3^{2-} ions present in the solution reacted to form CSH. In the presence of UI, the ultrasonic irradiation effect on nucleation is the reduction in the elapsed time between the establishment of supersaturation and the onset of nucleation and crystallization. This is caused by the pressure created by bubble collapse, temperature and the highly spatially concentrated regions of extreme energetic agitation and following the release of shock waves. An additional, significant factor associated with UI is reaction kinetics. Since the collapse of the microbubbles is an event during which energy is released in the form of a shock wave this is the moment when the activation energy barrier is surmounted (de Castro & Priego-Capote, 2007). Simultaneously, since the collapse of the bubble arises over a very short time, the nuclei created around this event, while numerous, have their growth confined by the short period of time during which the collapse occurs.

Table 4.1: Crystallite size and lattice strain CSH between G1 and G2 by ultrasonic irradiation. (± Standard deviation)

	Sample	Crystallite size (nm)	Lattice strain (%)
G1-Group	S1	10 (± 1.5)	0.0282
	S2	9 (± 1)	0.02
	S3	9.2 (± 1)	0.0282
G2-Group	S4	15.7 (± 1)	0.017
	S5	13 (± 1)	0.02
	S6	24.7 (± 2)	0.010

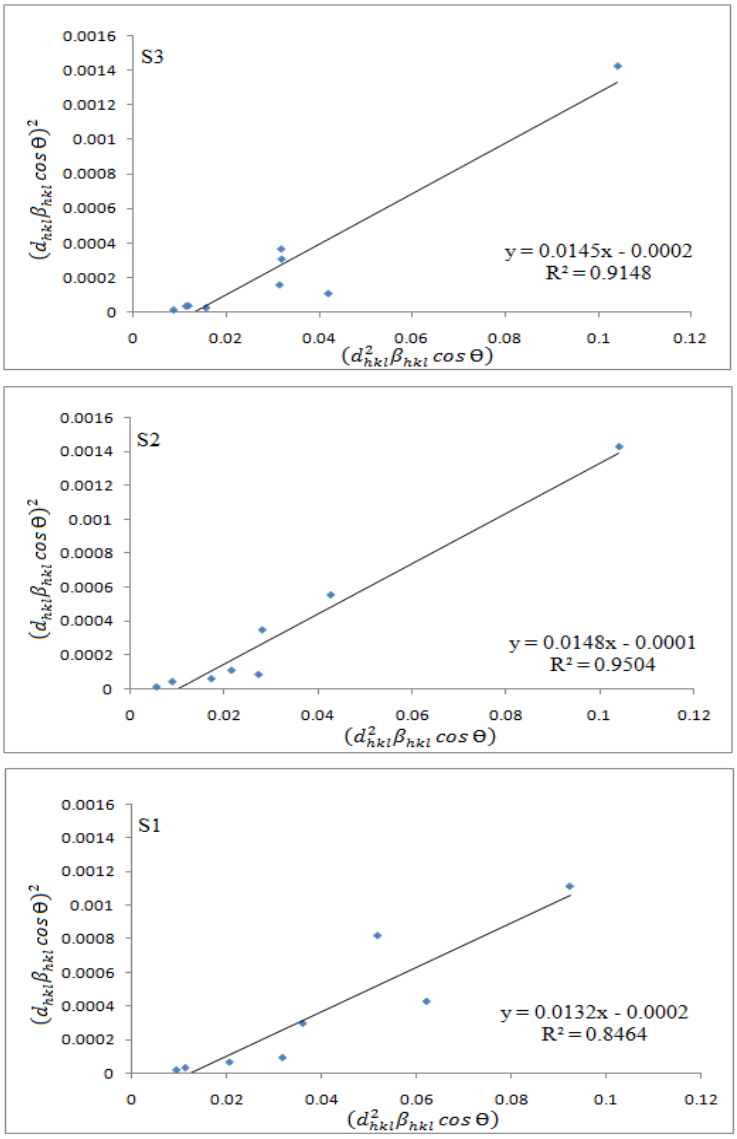

Figure 4.2: The SSP plot of CSH samples at different times. The particle size is achieved from the slope of the linear fitted data and the root of *y*-intercept gives the strain.

As shown in Table 3.1, it was found that the yield of CSH increased when the sonication time was extended from 5 to 15 minutes at the same UI condition. The UI wave is not enough to blend the solution and precipitant uniformly within a short period of time, therefore the yield of CSH powders increased at longer times of insonation.

It was found that sonication time also influenced the average crystallite size and lattice strain. The crystallite size and lattice strain is estimated from the peak broadening of XRD reflection according to the SSP formula (Eq. (1)). The results obtained are listed in Table 4.1.

According to the data presented in Table 4.1, the crystallite size and the lattice strain initially decrease with time from 5 to 10 min sonication; and later both crystallite size and lattice strain increases from 10 to 15 min. These results suggested that it is possible to tailor crystallite size by UI duration alone. Moreover, the decrease of CSH crystallite size compared to the increase of sonication time is not linear. The reaction media of CSH by chemical precipitation method from these sources is an exothermic reaction (Speiser, Baumann, & Niessner, 2000). The present results show that temperature increased to 90 °C after 15 min sonication while the changes in pH of our irradiated samples were negligible. The temperature of the solution rapidly increased from 32°C to 80 °C within 5 min UI and then the temperature were rising at a rate of 1 °C/min from 5 to 15 min. This indicates that long irradiation times increased the temperature of the reaction media. It has been reported that increasing the temperature in UI can be effective in the increase of crystallinity (Baradaran et al., 2013; Rouhani, Taghavinia, & Rouhani, 2010). By comparing the X-ray diffraction (XRD) patterns presented in Figure 4.1, it can be observed that the crystallinities of the resultant CSH increased with increasing synthesis temperature and sonication time and that the improved degree of crystallinity may be due to the raised temperature and irradiation time in the aqueous solution during UI.

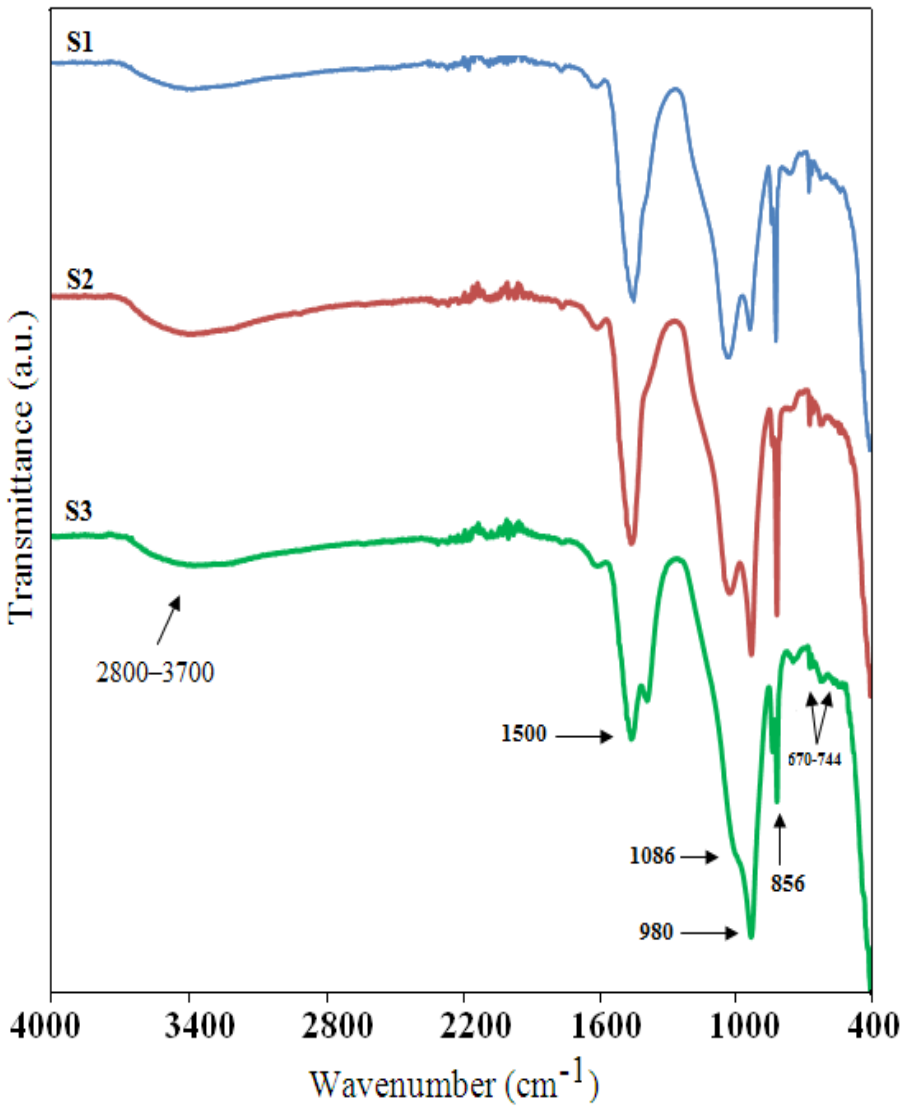

Figure 4.3: FT-IR spectra of G1-Group prepared using different UI times.

Figure 4.3 illustrates the FTIR spectra of the CSH samples synthesized with three different durations 5, 10 and 15 min. The formation of CSH is indicated by a complex group of bands in the range of 800–1200 cm^{-1} (Björnström, Martinelli, Matic, Börjesson, & Panas, 2004; P. Yu, R. J. Kirkpatrick, B. Poe, P. F. McMillan, & X. Cong, 1999). The sharp band at 980 cm^{-1} is characteristic for the Si–OH vibration (Björnström et al., 2004; Delgado, Paroli, & Beaudoin, 1996). The band at 1086 cm^{-1} can be attributed to Si–O stretching vibrations, and the group of bands between 670 and 744 cm^{-1} can be attributed to Si–O–Si bending vibration. These two groups of bands are

features of silicate chains (SiO_3)(Ping Yu et al., 1999). Moreover, the characteristic bands for the CO_3^{2-} group occur in the spectrum at 1500 cm^{-1} (ν_2, asymmetric stretch vibration) and at 856 (ν_2, out-of-plane bend vibration). All the experimental conditions by UI were carried out in air; therefore it is not possible to prevent incorporation of CO_2 if the sample is exposed to air(Ping Yu et al., 1999). The broad band at 2800–3700 cm^{-1} is due to stretching vibrations of O–H groups in H_2O or hydroxyls with a wide range of hydrogen bond strengths. In order to form calcium silicate hydrate, more H_2O molecules become coordinated in the produced CSH structure, participating with Si–O groups to form an intricate network of hydrogen bonds. These results are in good agreement with the X-ray diffraction analysis.

4.2.1.1 Morphological feature

The morphological features of the CSH samples at different times of UI are given in the FESEM images (Figure 4.4) by comparing the micrographs of the obtained powders by UI, it can be shown that the UI duration affected morphologic features. The FESEM micrograph of CSH derived at 5 min shown in Figure 4.4 (S1) suggests that the sample consists of agglomerated nano particles. When the ultrasonication time was increased to 10 min, the needle-like shape morphology dominated, where diameter and length of the CSH varies in the range of 20–30 and 300–500 nm, respectively, as measured by internally supported software (Figure 4.4 (S2)). In addition, when the sonication time was increased to 15 min, the concentration of the needle-like morphology is further increased (Figure 4.4(S3)). Prolonged reaction time of 15 min showed the formation of large number of needle-like shape with well-defined morphology with typical widths of 30 to 50 nm and lengths in the range of 100 to 200 nm.

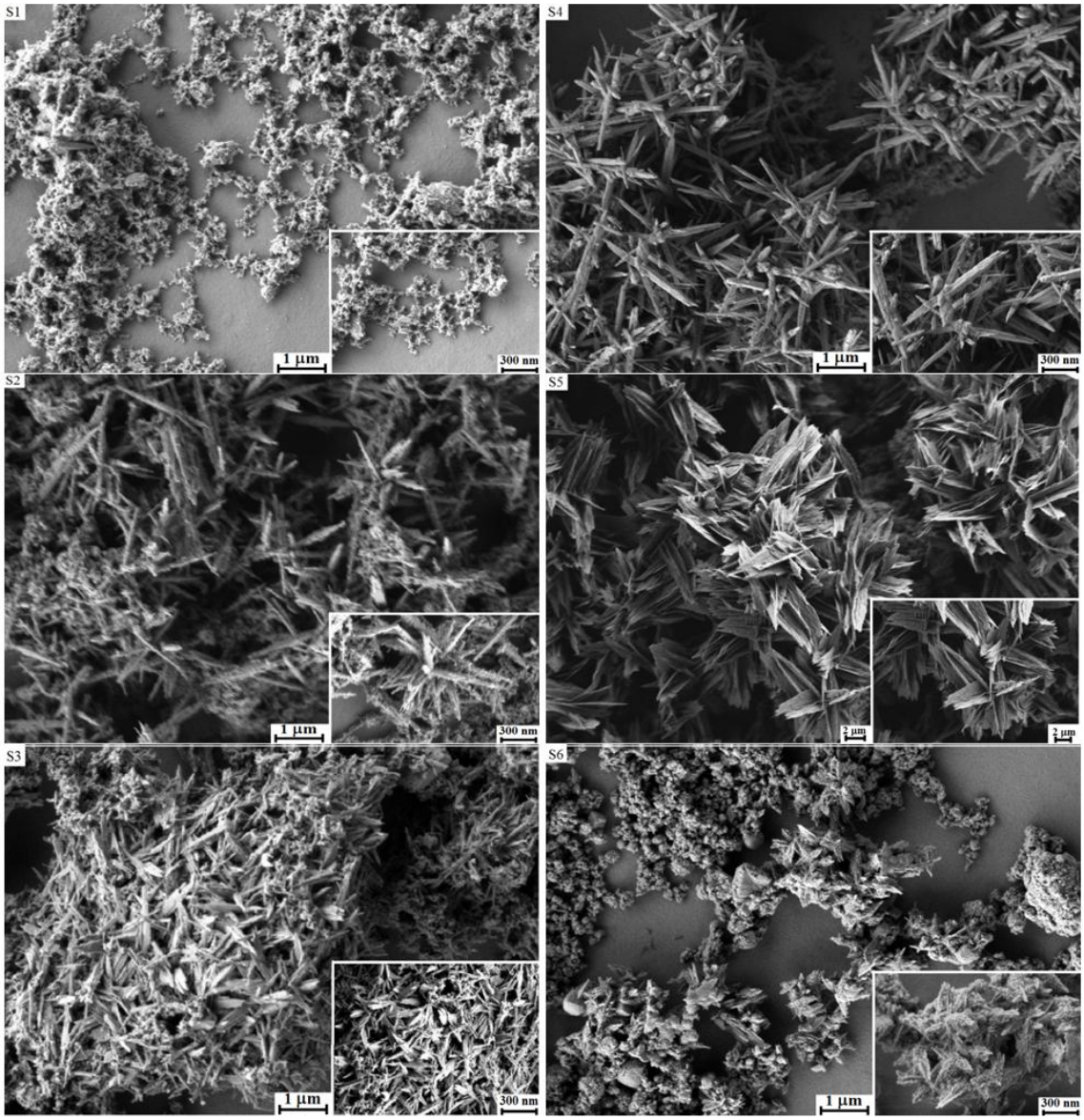

Figure 4.4: FESEM micrographs of the G1-Group (S1, S2, S3) and G2-Group (S4, S5, S6).

There are two regions of sonochemical activity: one is between the cavitation bubble and the surrounding bulk solution, and the other is inside the collapsing bubbles (Jevtic et al., 2008). If the reaction takes place inside the bubble, the powders are amorphous, and if it takes place in the surrounding region, it is supposed to be that the products are nanocrystalline (R. V. Kumar, Koltypin, Palchik, & Gedanken, 2002). In this present case, crystalline powders with needle like morphology were obtained, it is to be expected that the formation of the CSH probably occurs in the interfacial region. The formation mechanism of the needle-like morphology is based on the electrostatic

interaction between Ca^{2+} and SiO_3^{2-} ions at first and then followed by their assembly on the surface of micelles. In the early stage, the examination of intermediate products shows the coexistence of agglomerated nano particles and then needle like formed with increasing irradiation time. The formation process of needle-like particles is schematically illustrated in Figure 4.5.

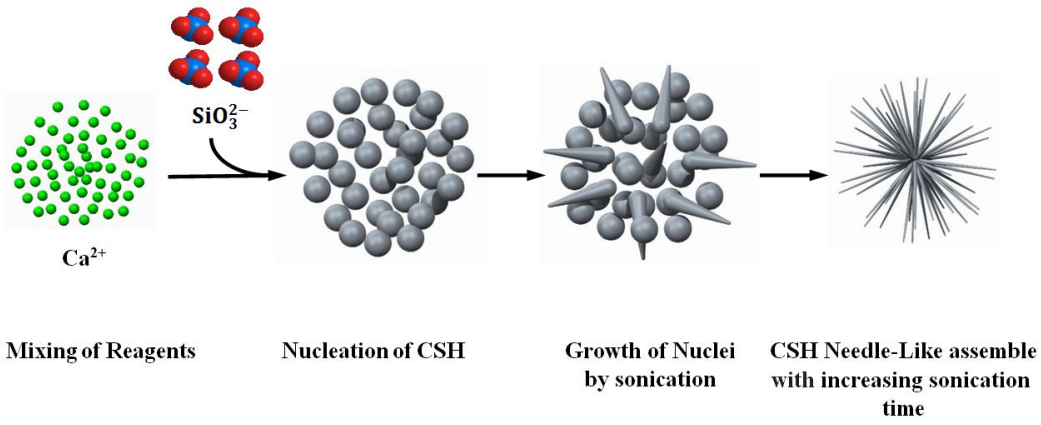

Figure 4.5: Mechanism proposed to be involved in the sonochemical synthesis needle-like CSH with increasing sonication time.

The FESEM results demonstrated the deagglomeration abilities of the UI process. Use of ultrasound as a reaction aid to promote deagglomeration has been studied (Prasad, Pinjari, Pandit, & Mhaske, 2011; Raman & Abbas, 2008) and established and the present results further support the potential use of sonochemistry in synthesis.

The results above show that CSH with different crystallite sizes and morphologies have been prepared successfully at different sonication times, and 10 min of UI was the optimal time for CSH synthesis by ultrasonication technique.

4.2.2 Synthesis of CSH using SDS as a surfactant assisted by ultrasonic irradiation

SDS was used as a surfactant to modify and control the morphology and size of the CSH. In the absence of SDS, the morphologies of CSH were needle-like and not uniform. Therefore, the influence of various concentrations of SDS at 10 min UI on the structure of the final products and the growth-orientation processes were examined.

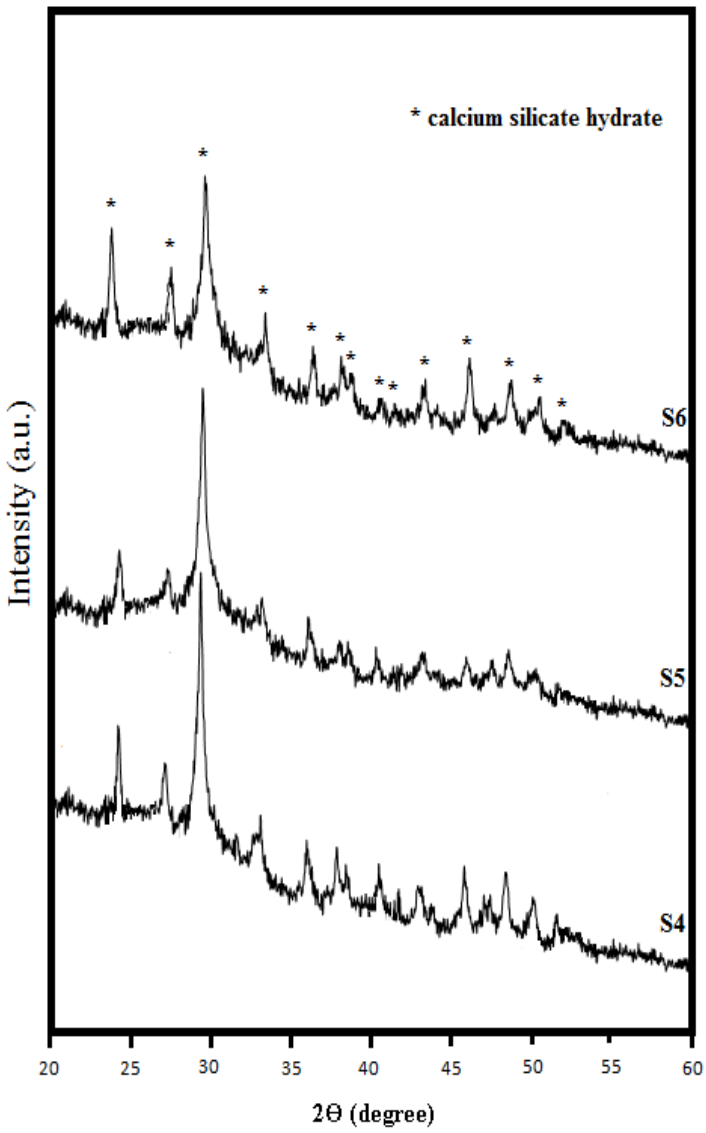

Figure 4.6: XRD patterns of G2-Group (different concentrations of SDS at 10 min) of samples.

A significant effect of SDS was observed on the yield of CSH (Table 3.1), where the yield percentage increased when the concentration of SDS was increased.

Figure 4.6 shows the XRD patterns of samples obtained from varying concentrations of SDS. The resulting diffractogram demonstrates that the sonochemically synthesized product at different amounts of SDS is CSH (JCPDS 03-0606). It was found that sample G2 (added SDS) has higher XRD diffraction intensity and sharper XRD peaks than that of sample G1 (no SDS). This intensification of XRD peaks indicates an increase of crystallinity. In addition, the peak intensity decreases when the concentration of SDS is increased.

Figure 4.7 and Table 4.1 present the crystallite size and lattice strain of the CSH synthesis powders at various SDS concentrations as calculated using the SSP formula (Eq. (3.1)) from the profile of the main peaks of the XRD pattern. It is evident that the crystallite size and lattice strain between different surfactant concentrations is not linear. The crystallite size of CSH powders without the addition of SDS was 9 nm at 10 min by UI, while the sizes in the presence of SDS ranged between 13–24.7 nm as the SDS content rises from 0.1 to 0.3g at 10 min by UI. The rise of crystallite size and reduction of lattice strain with the addition of SDS suggests that SDS may encourage particle growth.

The smallest crystallite size (13 nm) with maximum lattice strain (0.02) was obtained with 0.2 g SDS. Furthermore, the change of the lattice strain of CSH demonstrated that SDS anionic surfactant was structurally incorporated, and did not just cover the surface of the crystals.

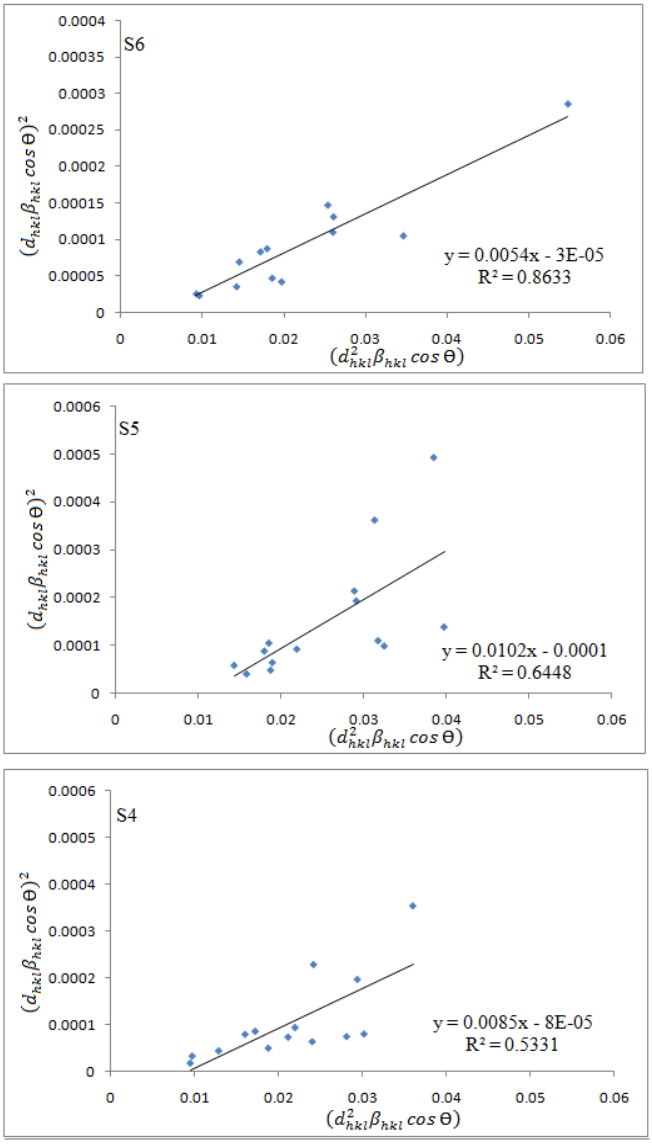

Figure 4.7: The SSP plot of CSH samples G2-Group with different concentrations of SDS at 10 min UI. The particle size is achieved from the slope of the line fitted data, and the root of *y*-intercept gives the strain.

Figure 4.8 illustrates the FTIR spectra of the CSH samples in the G2-group synthesized with various concentrations of SDS at 10 min UI. FTIR analysis reveals the presence of SDS on the surface of the CSH. The characteristic peaks for SDS (C-H) stretching and bending bands in 2853-2965 cm^{-1} and $–OSO_3^-$ bending band at 720 cm^{-1} were found, identifying that the precipitated CSH was covered with template SDS (P. Zhang et al., 2012) and is very weak. The FTIR also identifies the functional groups of

CSH samples that are comparable with G1-group (no SDS) as explained above. On the basis of XRD and FTIR results, one concludes that samples obtained in the different SDS concentrations are CSH.

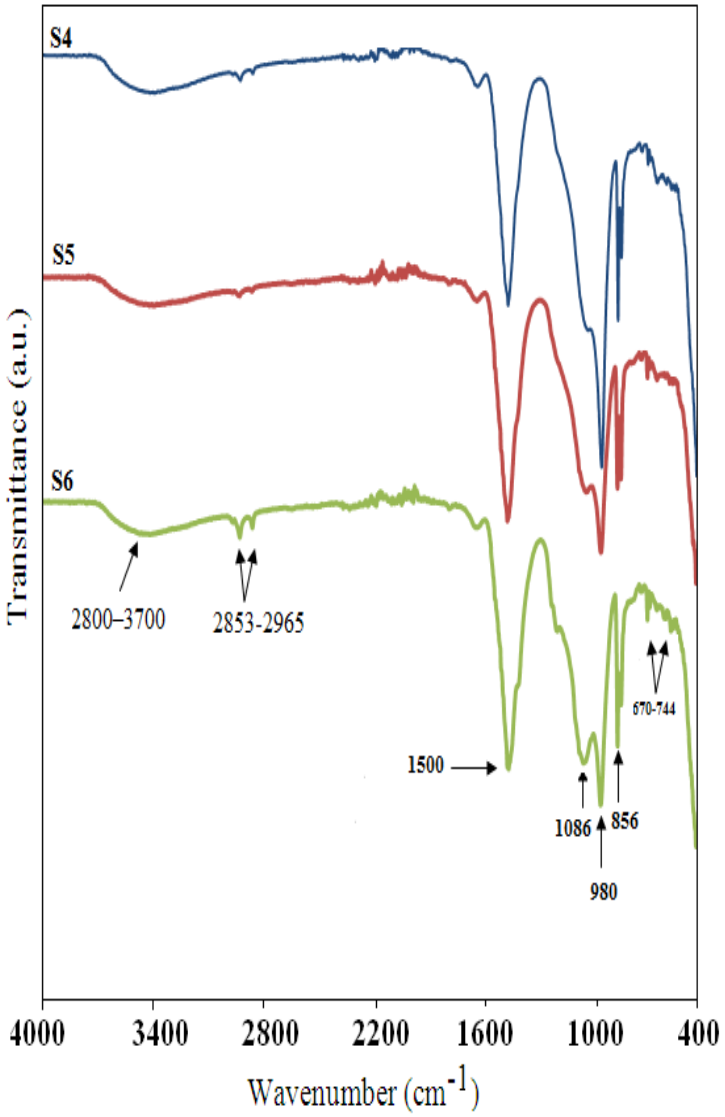

Figure 4.8: FT-IR spectra of G2-Group prepared using different concentrations of SDS at 10 min UI.

4.2.2.1 Effect of SDS surfactant on morphology of CSH

The SDS is an anionic surfactant with a hydrophobic tail and a negatively charged head that dissolves in water to form a colourless solution. Figure 4.4 (G2-group) presents the effect of different concentrations of SDS on the morphology of the CSH powder synthesized with 10 minutes of ultrasonic irradiation time. In the absence of SDS, the morphologies of CSH were needle-like and not uniform. No nanosheet morphology was obtained. However, the uniform needle like and nanosheet morphologies were formed in the presence of SDS. As shown in Figure 4.4 (S4), by comparing the micrographs of the obtained powders with 0.1g SDS (S4) and without SDS (S2), both ultrasonicated for 10 minutes, it can be seen that SDS changed the morphology by increasing the diameter and length of the CSH needle-like particles variably in the range 100–200 nm and 1–2 μm, respectively. When the amount of SDS is increased to 0.2 g, micelles can be formed more easily. As a result, highly oriented needle-like particles were assembled to form bundles with nanosheet morphology. As shown in Figure 4.4 (S5), a smooth surface is observed on the solid nanosheets of CSH. The width and length of the nanosheets are 300- 500 nm and 2-3 μm, respectively. When the amount of SDS in the solution increased to 0.3g (Figure 4.4 (S6)), it had a direct destructive effect on the morphology and irregular morphologies without bundles of nanosheets and needle-like particles were observed (Figure 4.4 (S6)). Therefore, the higher concentration of SDS possibly interfered with the synthesis mechanism, which restricts the formation of the nanosheets or needle-like particles in the present reaction.

Considering all factors, as also schematically illustrated in Figure 4.9. The assembled process of CSH nanosheets under the effects of SDS and ultrasound is proposed as follows: First, due to the electrostatic interaction and stereochemical matching with Ca^{2+} ions, the negatively charged SDS polar groups acted as active sites for nucleation of CSH. Then, Ca^{2+} ions strongly absorbed on the micellar surface of the

opposite charge, leading to a much faster nucleation rate on the surface of the SDS micelles and calcium ions can then react with the SiO_3^{2-} groups. However, with the work done by ultrasonic radiation, the CSH nanosheets arranged and formed an orderly assembled structure along the direction of flow with low energy. Consequently, both SDS and ultrasound had an impact on the orderly layered assembly of CSH nanosheets: SDS as a template ensured the formation and stability of CSH nanosheets, and the ultrasound provided the necessary work and driving force for assembly of CSH nanosheets.

These results confirm that different amounts of SDS are favorable for the synthesis of CSH with various types of morphologies. Moreover, the results indicate that the optimum crystallite size is about 13 nm after 10 minutes of sonication time with 0.2 g SDS and demonstrates bundles of nanosheets morphology with an average diameter and nanosheets length 300- 500 nm and 2-3 μm, respectively.

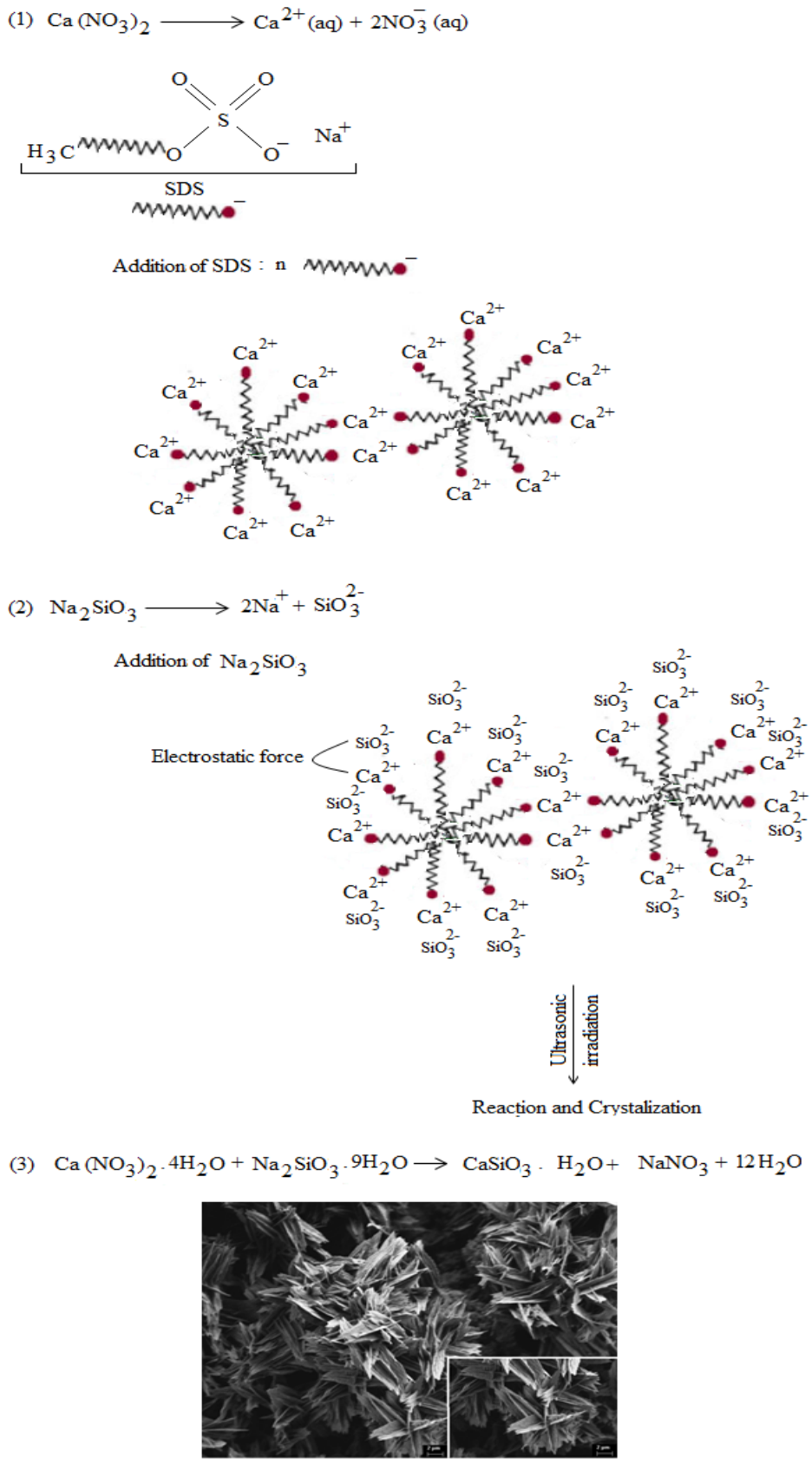

Figure 4.9: Schematic diagram of the formation process of CSH nanosheets with the effect of SDS and ultrasonic radiation.

4.3 Calcium silicate–reduced graphene oxide composites

In this part of the research, a simple hydrothermal method was used to synthesize CS nanowires on reduced graphene oxide sheets. CS and CS/rGO composites were densified using HIP. The variation of the mechanical properties of CS/rGO composites with respect to the amount of rGO in the matrix has been systemically investigated. The effect of rGO content on the formation of HA on CS/rGO composites during soaking in a biomimetic system of simulated body fluid (SBF) were also evaluated. In addition, detailed *in vitro* experiments were performed such as cell adhesion, cell proliferation (MTT) and bone cell differentiation (ALP) experiments to explore the abilities of such materials to be successfully used in biomedical applications.

4.3.1 Characterizations of rGO, CS and CS/rGO composite powders synthesized by hydrothermal method

The hydrothermal process used in this study has a number of advantages over other synthesis techniques and chemical reduction methods: (1) the method uses a very simple setup, that is, essentially an autoclave; (2) the process is facile, rapid, and efficient and is industrially more feasible, as compared to batch processing; (3) the relatively high temperature and internal pressure promotes the recovery of π-conjugation after dehydration, which is favourable for minimizing defects; (4) it is inherently pure since it employs only water, compared to the hydrazine chemical reduction method which inevitably introduces non-carbon impurities into the treated GO (Stankovich et al., 2007); and (5) engineering the parameters of temperature and pressure affords a facile method to organize the degree of reduction of the GO (Y. Zhou, Bao, Tang, Zhong, & Loh, 2009).

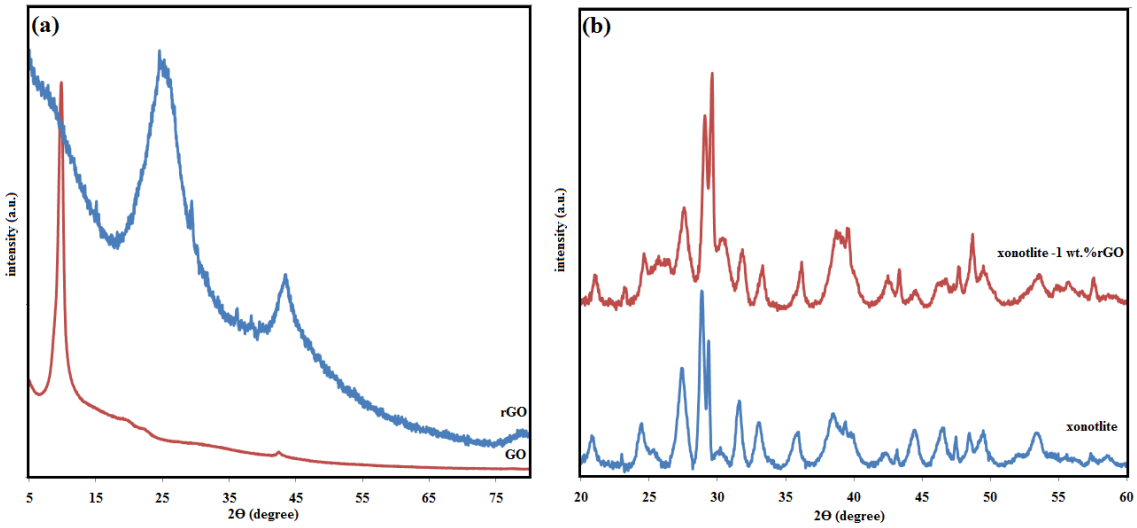

Figure 4.10: (a) XRD patterns of GO and rGO. (b) XRD patterns of pure xonotlite and xonotlite-1wt. %rGO composite.

The XRD spectrum of the GO in Figure 4.10a is similar to those in other reports (Marlinda et al., 2012; Mohammad Mehrali, Latibari, Mehrali, Indra Mahlia, & Cornelis Metselaar). The XRD pattern of GO shows an intense and sharp diffraction peak at 2Θ = 9.85°, attributed to the (001) lattice plane corresponding to a d-spacing of 0.83 nm. This is consistent with the lamellar structure of GO. GO sheets can be reduced under hydrothermal conditions, resulting in the disappearance of this strong peak and the appearance of a broad (002) peak and a weak (100) peak at 2Θ values of 24.53° and 43.45°, respectively, corresponding to d-spacings of 0.36 nm and 0.20 nm, respectively. This implies that the GO was reduced to rGO sheets due to the removal of functional groups from the GO after the hydrothermal process (Muruganandham, Amutha, & Sillanpaa, 2010; Sookhakian, Amin, & Basirun).

Figure 4.10b presents the XRD spectra of the products obtained after hydrothermal processing at 200 °C for 24 h in the absence and presence of rGO, which are dominated by the xonotlite phase reflection peaks (JCPDS card No. 23-0125). However, both in terms of d-spacings and positions (2θ) of the peaks, indicating that the synthesized products are pure xonotlite nanowires. The xonotlite crystal is a calcium silicate-type hydrated calcium silicate.

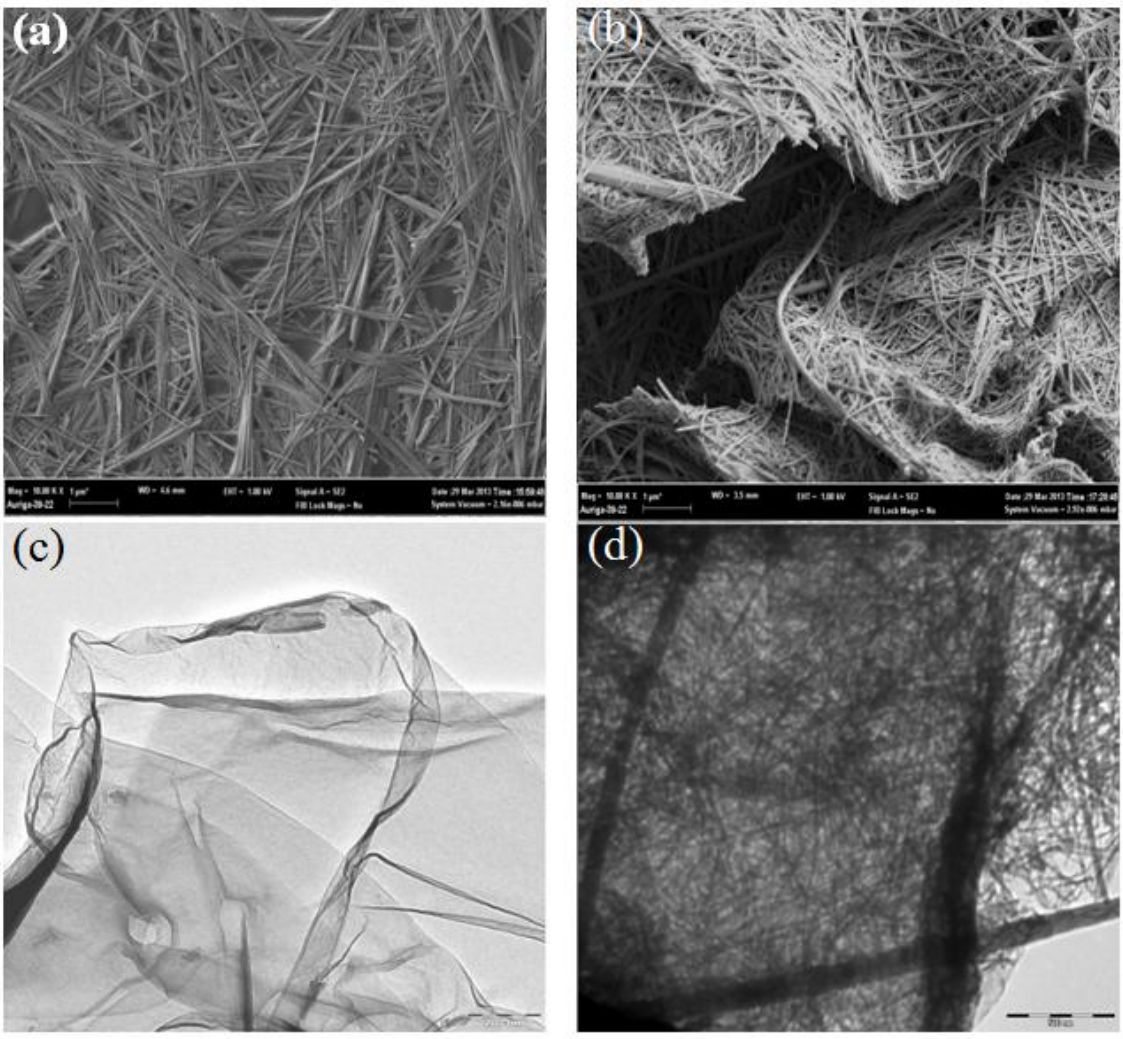

Figure 4.11: FESEM micrographs of pure xonotlite (a), xonotlite-1wt. % rGO composites (b) and TEM images of GO (c) and xonotlite -rGO composites (d) synthesized via the hydrothermal technique.

The XRD analysis further indicates that the main diffraction peaks of the xonotlite phase with GO are similar to those of the pure xonotlite phase. No other reflection peaks are observed, including (001) GO reflections, indicating the formation of a high purity xonotlite phase and hydrothermal reduction of the GO to rGO. Moreover, no typical diffraction peaks of rGO are detected in the composites, which can be explained by the low diffraction intensity of the peaks and the low amount of rGO.

In the absence of rGO, the xonotlite phase appears as nanowires with approximate diameters of 10-30 nm and lengths of up to several micrometers, similar to the results reported by Kaili Lin et al. (Lin, Chang, Chen, et al., 2007). As depicted in Figure 4.11, no other morphologies are observed in the FESEM images. Figure 4.11b shows similar morphological features in the xonotlite-rGO composites. The TEM observation presented in Figure 4.11c and d show that the rGO sheet is very thin, with few wrinkles and folds. Moreover, the rGO nanosheets are efficiently decorated with xonotlite nanowires on both sides of the translucent sheets as shown in Figure 4.11b and d. This validates that the nanowires are formed via the growth of xonotlite crystals through an Ostwald ripening mechanism, that is, a highly supersaturated solution was adopted and irregular nanoneedles acted as the precursor for the synthesis of crystallized xonotlite nanowires. In the hydrothermal reaction, crystallization process is a transformation process that amorphous fine nanoparticles act as the precursor. The formation of tiny crystalline nuclei in a supersaturated medium occurred at first, and then followed by crystal growth. The large particles will grow at the expense of the small ones because of a superior solubility of the small particles than that of large particles.

AFM was used to analyze the lateral dimensions of the graphene oxide and reduced graphene oxide sheets, as shown in Figure 4.12. The as-prepared GO sheets with average lateral dimensions (ALDs) of 3.88±0.99 μm are presented in Figure 4.12a and c. The pure rGO prepared by hydrothermal technique at 200 °C for 24 h resulted in partial fragmentation of the sheets and consequently smaller ALDs (2.37±0.65 μm) as shown in Figure 4.12b and d for the hydrothermal rGO sheets.

To verify the formation of graphene oxide, reduced graphene and xonotlite nanowires in the absence and presence of rGO, the infrared spectra of the samples were measured and are compared in Figure 4.13.

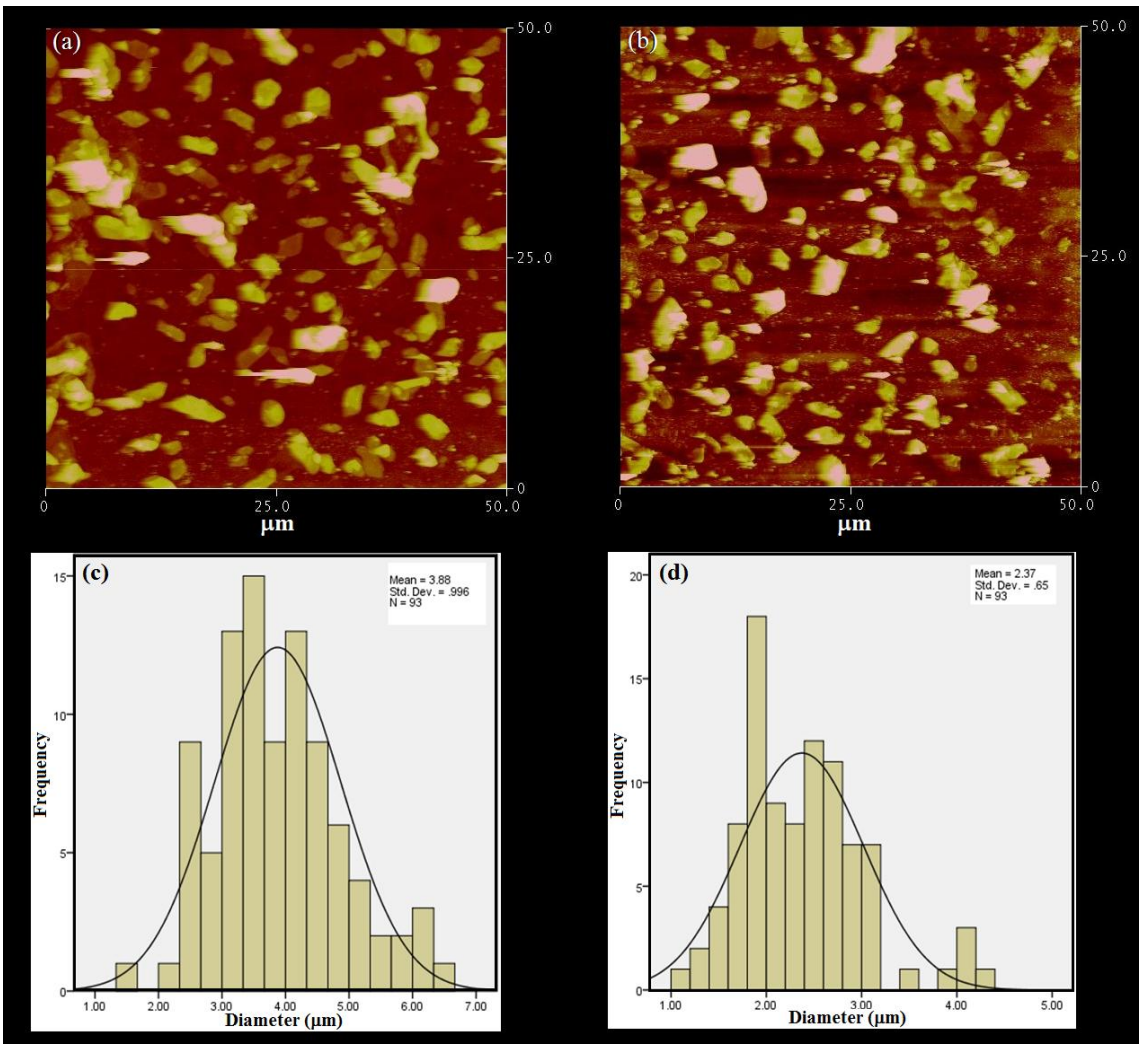

Figure 4.12: AFM images of the as prepared GO sheets (a), pure rGO prepared by hydrothermal technique at 200 °C for 24 h (b), size distribution diagram of GO (c) and rGO (d).

The FTIR spectrum presents all the characteristic bands for GO including the appearance of the broad peak from 900 to 1200 cm^{-1} attributed to C−O stretching and the peak at 1370 cm^{-1} representing tertiary alcoholic C−OH bending. Other features include the stretching vibration of the sp^2 hybridized C=C bond at 1625 cm^{-1}, the C=O stretching vibration at 1720 cm^{-1} and common hydroxyl stretching around ~3430 cm^{-1} (Lim et al., 2011; Sookhakian et al.). Figure 4.13 presents the FTIR spectrum of the rGO following hydrothermal reduction, including absorption peaks representing the C−O stretching vibrations of epoxy groups at 1050 cm^{-1} and the deformation of C−OH at ~1430 cm^{-1}. Moreover, the characteristic peaks of rGO nanosheets are usually

recognized as the asymmetric stretching of CH_2 at 2920 cm^{-1} and the symmetric stretching of CH_2 at 2850 cm^{-1} at the edges/defects (D. W. Wang, Wu, Gentle, & Lu, 2012).

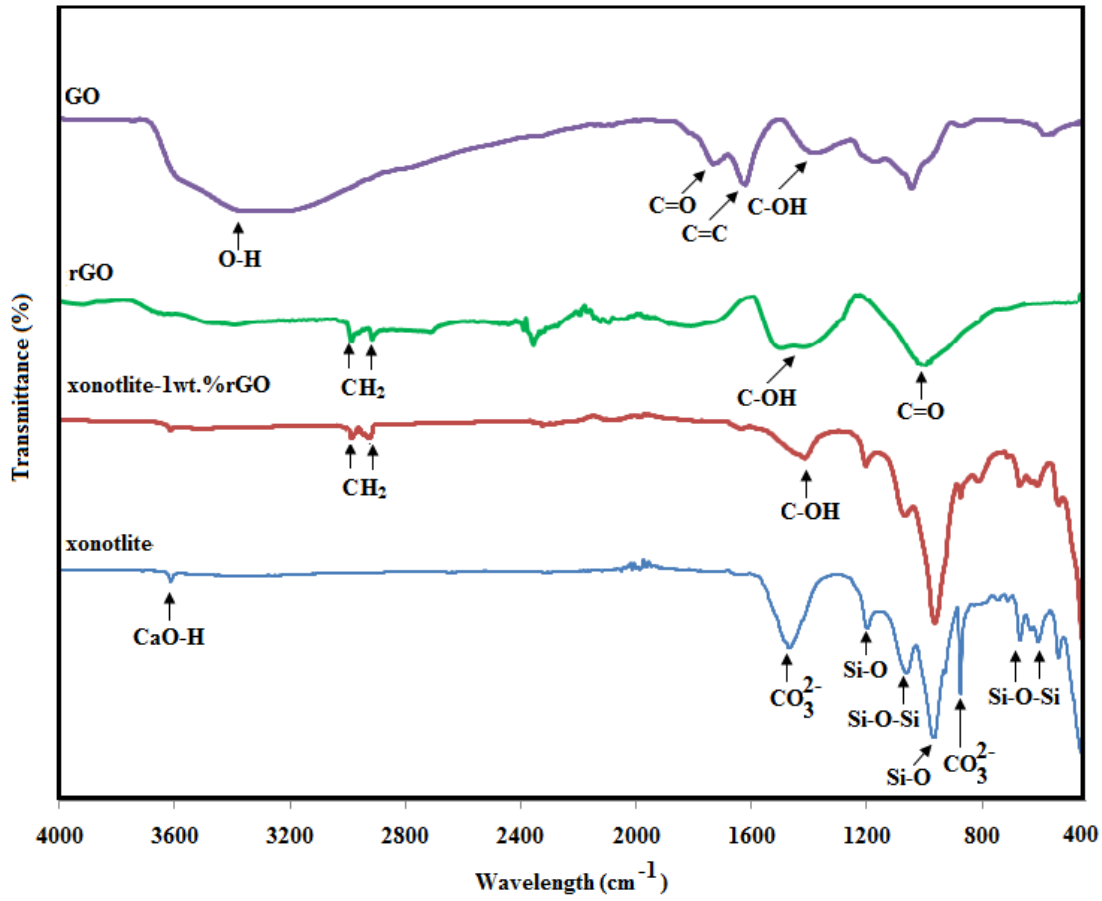

Figure 4.13: FTIR spectra of the GO, rGO, pure xonotlite and xonotlite -1wt. % rGO composites.

The FTIR spectrum of the pure xonotlite sample shows a sharp spike at 3610 cm^{-1} due to the CaO–H stretching vibration, and its bending mode is observed at 630 cm^{-1}. The characteristic bands for the CO_3^{2-} group occur in the spectrum at 1470 cm^{-1} (ν_2, asymmetric stretch vibration) and at 875 (ν_2, out-of-plane bend vibration). Note that no carbonates are detected by XRD analysis, while CO_3^{2-} bands appear in the powder spectra. This may be due to contamination with CO_2 during powder preparations and drying. Generally, xonotlite has a characteristic band at approximately 1200 cm^{-1}; this band is due to the Si–O stretching of vibrations in Q^3 sites (silicate tetrahedra linking

two silicate chains) (Mostafa, Shaltout, Omar, & Abo-El-Enein, 2009). The bands at 1065 and 970 cm^{-1} can be attributed to the symmetric stretching modes of Si–O–Si and Si–O, respectively. The bands observed at 670 cm^{-1} and 607 cm^{-1} are related to the Si–O–Si bending vibrations. The CS/rGO composite exhibits clear absorption bands resulting from the asymmetric stretching of CH_2 at 2920 cm^{-1} and the symmetric stretching of CH_2 at 2850 cm^{-1}, which are inherent to reduced graphene oxide. The peak at approximately 1430 cm^{-1} was attributed to the deformation of CO–H, and this band has been observed in pure rGO. The other absorption bands are attributed to the xonotlite.

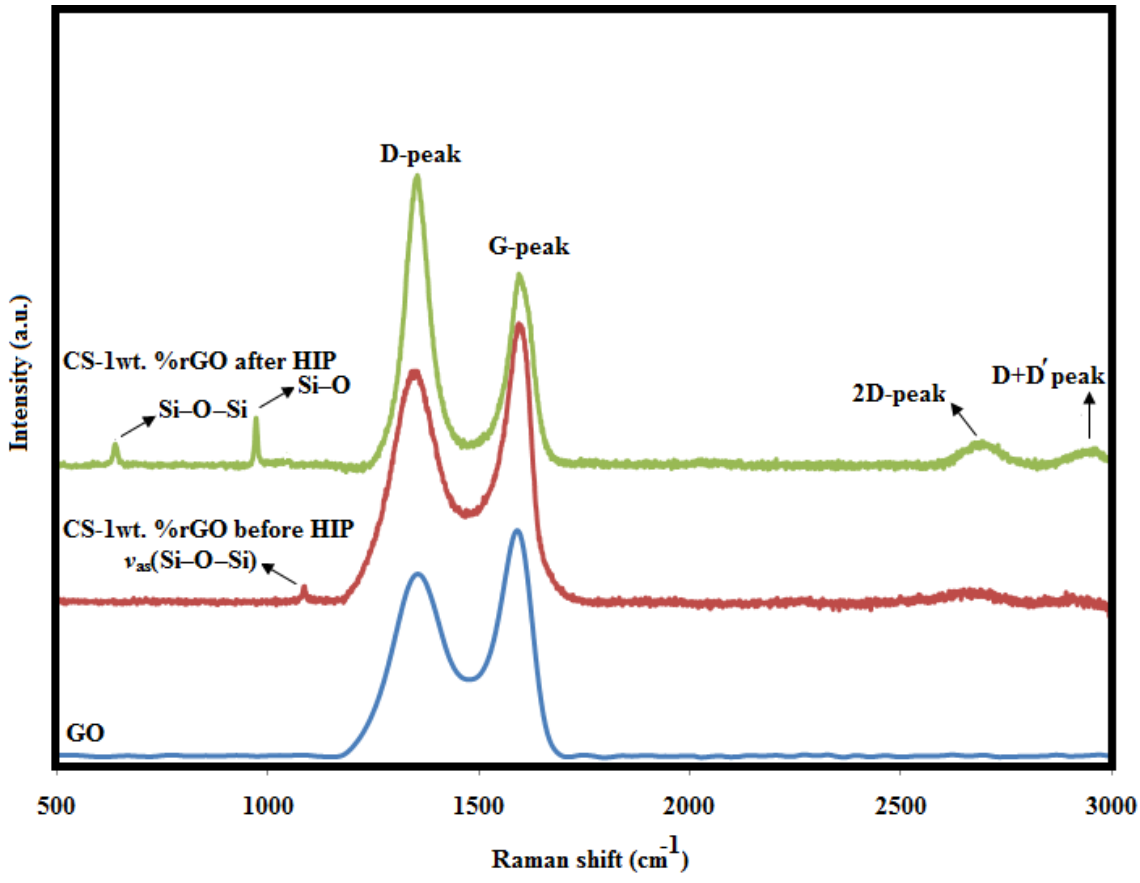

Figure 4.14: Raman spectra of GO and CS-1wt. % rGO composites before and after HIP.

The structure, defect levels and crystallinity of the reduced graphene oxide sheets in the composites were studied by further structural characterization using Raman spectroscopy. For comparison purposes, the Raman spectrum of graphene oxide is also shown in Table 4.2 and Figure 4.14. The Raman spectrum of GO displayed a band at 1595 cm^{-1} named the "G band" and another band at 1360 cm^{-1} named the "D band". The G-band represents the planar configuration sp^2 bonded carbon that makes up graphene, and the D-band is due to the breathing modes of six-atom rings and requires a defect for activation (Ferrari & Basko, 2013).

The Raman spectrum of the xonotlite/rGO composite exhibits significant changes compared to the spectrum of GO. Both the G-band and D-band are shifted towards lower wave numbers of 1346 cm^{-1} and 1593 cm^{-1}, respectively, and a 2D peak at approximately 2688 cm^{-1} indicates an increase in the number of layers in rGO compared to GO. The intensity ratio of the D to G-bands (I_D/I_G) is a measure of the degree of disorder and the average size of the sp^2 domains in graphene materials (Geim & Novoselov, 2007). The I_D/I_G ratios for GO and xonotlite/rGO composites were found to be 0.79 and 0.83, respectively, as shown in Figure 4.14. The increase in the I_D/I_G ratio after the hydrothermal reaction suggests that there the graphene lattice contains structural defects and that the reaction decreases the average size of the sp^2 domains (Zeng et al., 2013). This result is in agreement with that of the AFM observation mentioned above (Figure 4.12). As seen in Figure 4.14, the spectrum of the xonotlite/rGO composite before sintering exhibits a single peak representing the xonotlite phase at 1088 cm^{-1}, which can be attributed to the Si–O–Si asymmetric stretching mode (ν_{as}(Si–O–Si)) (Garbev et al., 2007).

Table 4.2: Peak position of the D, G and 2D bands and intensity ratios of I_D/I_G and I_{2D}/I_G.

Sample	D band Raman shift	G band Raman shift	2D band Raman shift	I_D/I_G	I_{2D}/I_G
Graphene Oxide (GO)	1360	1595	-	0.79	-
Unsintered (Xonotlite/rGO)	1346	1593	2688	0.83	0.43
Sintered (CS/rGO)	1355	1598	2690	1.24	0.12

4.3.2 Raman and XRD characterization of CS/rGO composite sintered by hot isostatic pressing

Exposure to high temperature during sintering makes it necessary to test for the survival of the rGO structure in the final samples. The presence of G and 2D peaks in the CS/rGO composites indicates the survival of rGO after HIP processing. As shown in Figure 4.14 and Table 4.2, the I_D/I_G ratio of the bulk xonotlite /rGO composite increased from 0.83 to 1.24 after HIP, demonstrating that the HIP process introduces structural defects into rGO. The intensity ratio of I_{2D}/I_G decreased and the 2D peak became narrower, sharper and shifted to higher wavenumbers compared with before sintering, indicating that rGO bonding may also occur during the HIP of the CS/rGO composites and that the number and thickness of layers may be increasing (Ferrari & Basko, 2013; A. Nieto et al., 2012). The broad peak at approximately 2940 cm^{-1} was assigned to the combination of the D and D′ bands (D + D′) (D. W. Wang et al., 2012). Thus, Raman spectroscopy demonstrates that the rGO structure is retained after HIP consolidation. Furthermore, two characteristic Raman peaks for the CS at 635 and 970 cm^{-1} were detected in CS /rGO composites after the HIP process and are attributed to the Si–O–Si bending vibration and the Si–O stretching vibration, respectively (Garbev et al., 2007; Osticioli et al., 2009).

To verify the phase after HIP, the samples were investigated by XRD as shown in Figure 4.15. The peaks in all six patterns are indexed as $CaSiO_3$ (standard card no. JCPD 31-0300), which illustrates that the xonotlite transformed to α-$CaSiO_3$ phase during HIP. XRD analysis confirmed that rGO and HIP processing did not induce the formation of any other phase. In the CS/rGO composites, it is difficult to detect the rGO by XRD due to its small content.

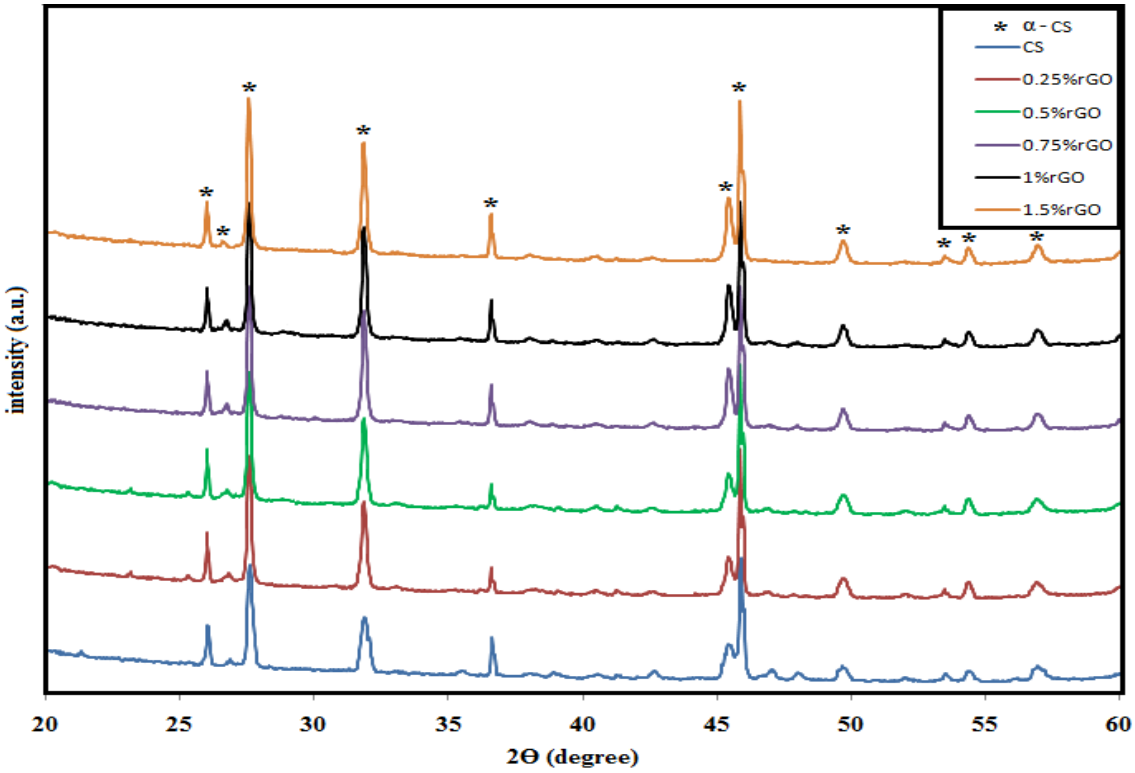

Figure 4.15: XRD patterns of CS-rGO composites sintered at 1150 °C by HIP.

4.3.3 Microstructural and mechanical properties of CS/rGO composites

High densification of the composites is necessary to obtain enhanced toughness, hardness and elastic modulus. As shown in Table 4.3, CS and CS/rGO have densities greater than 94% up to 1 wt. % rGO in the CS matrix, as determined using the Archimedes method. In addition, the density decreases with increasing rGO content in the composites because rGO separates the grains of the matrix, preventing pore closure.

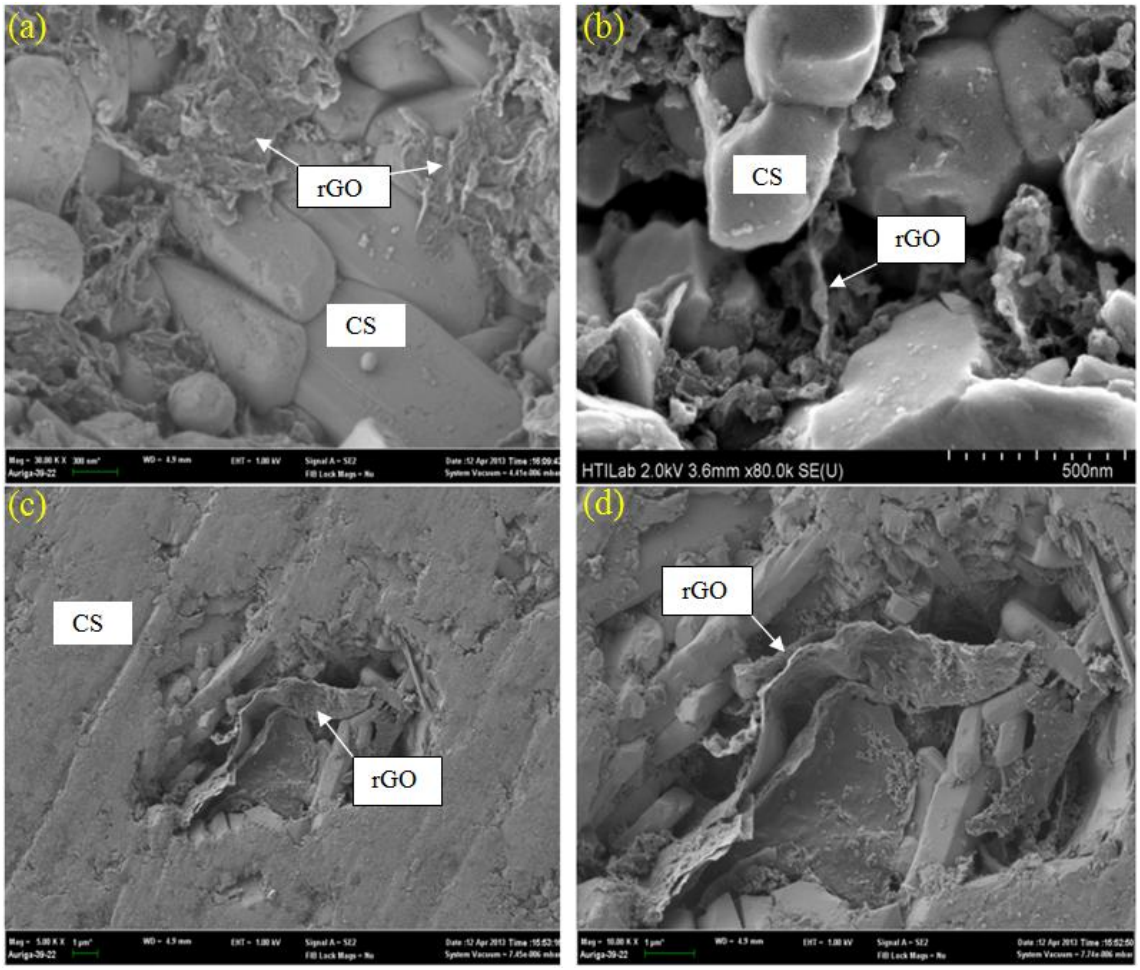

Figure 4.16: FESEM micrographs of CS/rGO composites after HIP consolidation. (a) and (b) Fracture surface of rGO-reinforced CS composites at 1150 °C by HIP. (c) and (d) Pores in the polished surface of CS-1.5 wt. %rGO, with visible graphene sheets.

Table 4.3: Mechanical properties of pure CS and GNP/CS composites

Sample	Relative density (%)	Elastic modulus (GPa)	Micro-hardness (GPa)	Nano-hardness (GPa)	Fracture toughness (MPa $m^{1/2}$)	Brittleness index ($\mu m^{-1/2}$)
CS	98±0.3	76.2±3.4	3.24±0.17	3.55±0.2	1.24±0.09	2.61
CS-0.25wt.%rGO	97±0.5	81.38±2.8	3.84±0.11	4.07±0.25	1.46±0.07	2.63
CS-0.5wt.%rGO	96.5±0.8	97.14±3.7	3.91±0.06	4.2±0.33	1.70±0.02	2.3
CS-0.75wt.%rGO	96±0.5	98.6±3.9	4.57±0.10	4.76±0.15	2.29±0.08	1.99
CS-1.0wt.%rGO	94±0.7	115.72±4.6	4.54±0.16	4.83±0.11	2.76±0.07	1.65
CS-1.5wt.%rGO	85±0.8	74.55±2.45	2.97±0.11	2.95±0.3	1.83±0.11	1.62

Figure 4.16c and d illustrate that the pores on the surface of the CS-1.5 wt. % rGO composite are open. The relative density is the lowest at 1.5 wt. % rGO, at approximately 85%. This is probably because the rGO tends to be distributed in the grain boundaries of the CS matrix, which hampers the densification process. Moreover, at a high concentration of rGO, pores are likely to be formed when a good bond between rGO and CS matrix is not formed, which makes it difficult to accommodate different shrinkages in the interface between rGO and CS matrix during cooling proces. In addition, overlapping of rGO exists in the sample containing 1.5 wt. %rGO as is observed in Figure 4.16c and d, which indicate agglomeration of rGO occurs. The agglomeration of rGO significantly affects the sintered body, reducing the density and mechanical properties (Lv Zhang et al., 2013). Although increasing the porosity of the CS/rGO composite might decrease its mechanical properties, these pores contribute to osteoblast ingrowth into the composite. Figure 4.16a and b show the fracture surfaces of sintered CS/rGO pellets at 1150 °C. These highly magnified images show that many

rGO pellets are well distributed in the composite matrix, indicating good dispersion of rGO.

Table 4.3 reports the variations in mechanical properties with the amount of rGO. Microhardness is an important mechanical property for ceramics and is critical when abrasive or grinding action is required.

The Vickers hardness and nano-scale hardness for the composites containing 0.75 wt. % and 1 wt. % rGO were ~40% and ~35% higher than those of pure CS. The absolute hardness values differ between nanoindentation and Vickers experiments due to the vast differences in applied load, tip geometry and measurement length scale (Lahiri, Singh, et al., 2011). The advantage of the microindetation test is that a much larger volume is being indenter and a higher volume fraction of rGO is encountered as compared to nanoindentation. The addition of rGO improves the hardness of CS up to 1 wt. % rGO. The hardness is reduced at 1.5 wt. % rGO because of increased porosity of the composite. As shown in Figure 4.16a and b, rGO is observed to wrap around CS grains. The high specific surface area of rGO can result in an increased contact area with the matrix. This could significantly increase the bonding strength between rGO and CS grains, requiring more energy to pull the nanofiller out from the CS matrix. The elastic modulus values of the HIPed pellets increased from 76.2±3.4 GPa for the pure CS to 115.72±4.6 GPa for the CS-1 wt% rGO, but decreased again to 74.55±2.45 GPa for CS-1.5 wt% rGO pellets. The increase in the elastic modulus of CS-rGO pellets is due to the high elastic modulus of graphene, the appropriate relative density of CS-rGO composites, homogeneous distribution of rGO in CS matrix and good bonding at the CS-rGO interface. Porosity has been reported to be a major factor governing the elastic modulus for some ceramic materials, with greater porosity correlated with a lower elastic modulus (X. J. Zhao, Chen, Ru, & Zhang, 2011). This explains the reduction of the elastic modulus in CS-1.5 wt. % rGO pellets. It is notable that the elastic modulus of

human cortical bone is reported to be in the range of 15–25 GPa, while the modulus is much higher for consolidated pure CS and our composites. A mismatch of the elastic modulus at the bone–implant interface might pose a risk of fracture or delamination of the implant (Shirazi, Mehrali, et al., 2014). Nevertheless, the osseointegration ability of CS creates strong bonding at the CS–bone interface, decreasing the chance of fracture and delamination. Likewise, an increase in the elastic modulus directly influences the improvement in the fracture toughness in ceramic based composite systems (Lahiri, Ghosh, & Agarwal, 2012).

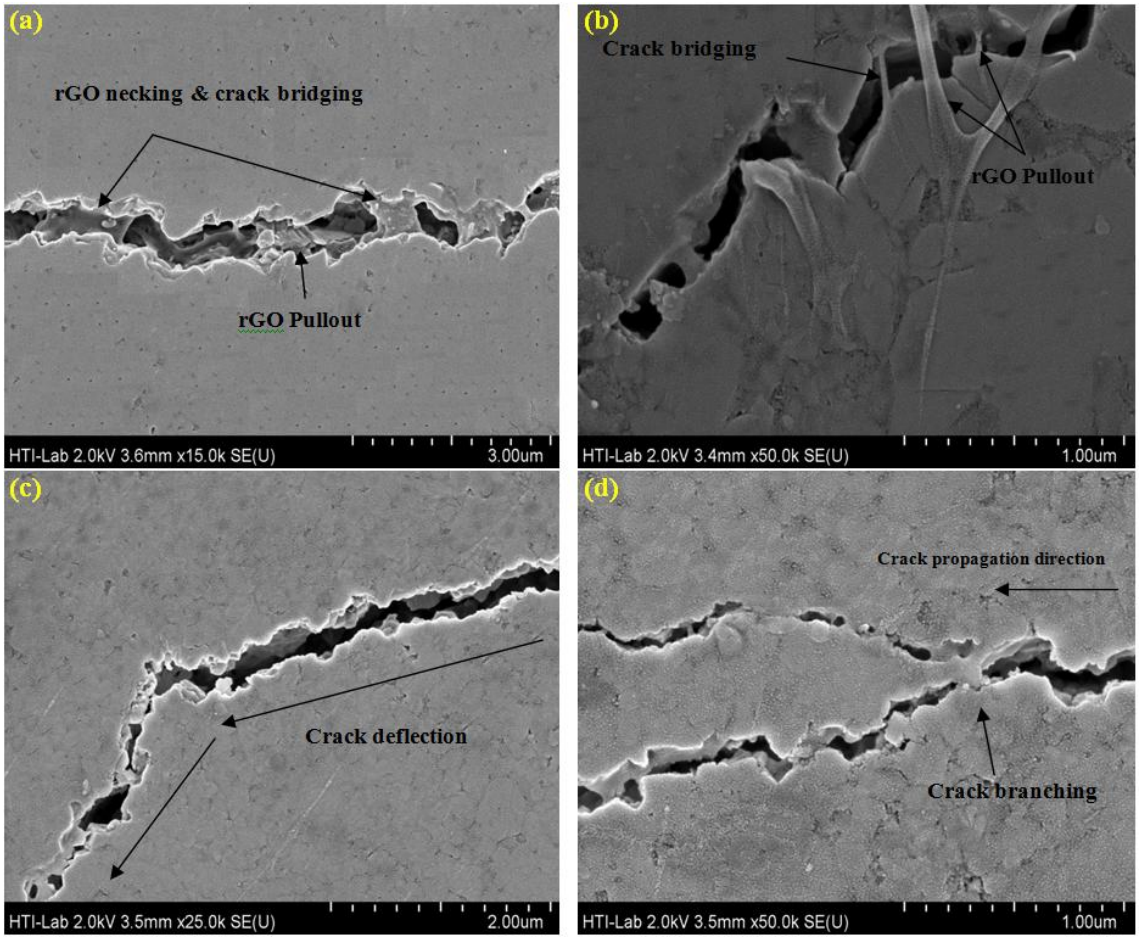

Figure 4.17: Toughening mechanisms in CS-rGO composites: (a) and, (b) crack bridging and rGO pull-out, (c) crack deflection and (d) rGO crack branching.

The addition of rGO to CS results in an improvement in the indentation fracture toughness as shown in Table 4.3. The fracture toughness is increased by 123% in the

CS-1wt. %rGO composite. The increase in toughness correlates with increasing rGO content, but this trend does not continue for CS-1.5 wt. %rGO due to the lower fracture toughness of the composite caused by the increasing porosity (Lahiri, Ghosh, et al., 2012). Four distinct rGO toughening mechanisms have been observed in CS-rGO composites as shown Figure 4.17. These mechanisms are (a) crack bridging, (b) rGO pull-out, (c) crack deflection and (d) rGO crack branching. Crack bridging is a frequently observed toughening mechanism in the CS-rGO composites. As seen in Figure 4.17a and b, rGO sheets can act as bridges and restrict the widening of the cracks. The rGO bridges increase the energy required to open the cracks and toughen the material. Other studies have also shown evidence of graphene bridging as an effective mechanism for the toughening of composite structures (J. Liu et al., 2012; Andy Nieto, Lahiri, & Agarwal, 2013; Lv Zhang et al., 2013). Pulling rGO out of the composite matrix can dissipate energy because of binding and friction, leading to toughening. Figure 4.17b presents FESEM images of rGO pull-out from the fracture surfaces of CS-rGO composites. Recent studies have shown that the highest fracture toughness could be obtained composites containing graphene with a small average lateral size, as graphene with larger lateral size are connected causes porosity, which probably results in a weak adhesion bond of graphene/matrix and low energy dissipation during the pull-out (Kvetková et al., 2012; Ramirez et al., 2014). As shown in Figure 4.17c, the resistance of rGO can be so strong that the crack seeks a lower energy path, resulting in crack deflection and energy absorption, resulting in the toughening of the matrix. Crack branching of rGO can be observed in Figure 4.17d, which consumes more energy and leads to an increase in the resistance to crack propagation. Crack branching is a very frequently observed toughening mechanism in all studied composites containing graphene (J. Dusza et al., 2012; J. Liu et al., 2012; Y. Zhao et al.). Dusza et al.(J. Dusza et al., 2012) investigated the influence of the addition

of graphene with different lateral size on the fracture toughness of graphene reinforced Si_3N_4 composites. They found that the origin of the branching mechanism is the interaction of the propagating crack and graphene with smaller size which was between 0.5 and 3μm. As mentioned earlier, in our case, the average lateral size for the rGO sheets is 2.37±0.65 μm. Thus, crack branching can cause an increase in the fracture toughness of CS-rGO composites. Based on these observations and analysis, we can infer that rGO pull-out, crack deflection, crack branching and crack bridging by rGO are responsible for the improved fracture toughness of CS-rGO composites.

Brittleness index (BI) can be used to quantitatively assess the machinability of ceramics. Boccaccini reported that the good machinability occurs when the brittleness index of the ceramic is lower than 4.3 $\mu m^{-1/2}$ (Boccaccini, 1997). Meanwhile, the lower the brittleness index, the higher the machinability of the ceramics. As regarding the hardness and fracture toughness values in the present study, our results show that the rGO are effective in the BI of CS. In the case of CS-1wt. %rGO composite the BI value decreased from 2.61 to 1.65 $\mu m^{-1/2}$, corresponding to a ~37% decrease compared to pure CS. Another interesting observation is that the plot shows a systematic decrease in BI with increasing rGO concentration. Porwal *et al*.(H. Porwal et al., 2013) reported that graphene oxide nanoplatelets (GONP) have a significant influence to reduce the BI and consequently improve the machinability performance in silica/GONP composites in comparison with pure silica. Overall, our results are in good agreement with results of Porwal *et al* (H. Porwal et al., 2013)**.**

4.3.4 *In vitro* HA forming ability of CS/rGO composites

Figure 4.18 presents the XRD patterns of CS/rGO composites after soaking in SBF for 14 days. The intensity of the CS diffraction peaks decreased, and hydroxyapatite peaks (Standard Card No: JCPD 24-0033) were obvious after soaking in SBF. When the rGO content in the composite increased, most diffraction peaks of CS disappeared and broad peaks at 2Θ= 31.7°, 2Θ= 49.5°, and 2Θ=53.2° and a strong peak 2Θ= 26° corresponding to the (2 1 1), (2 1 3), (0 0 4) and (0 0 2) planes of hydroxyapatite (HA), respectively, became more obvious. These results suggest that more HA is formed on the surface of composites with more rGO content, and the peak shapes indicate that this HA should be nanocrystalline. Furthermore, no cristobalite or other peaks were observed in any samples soaked in SBF.

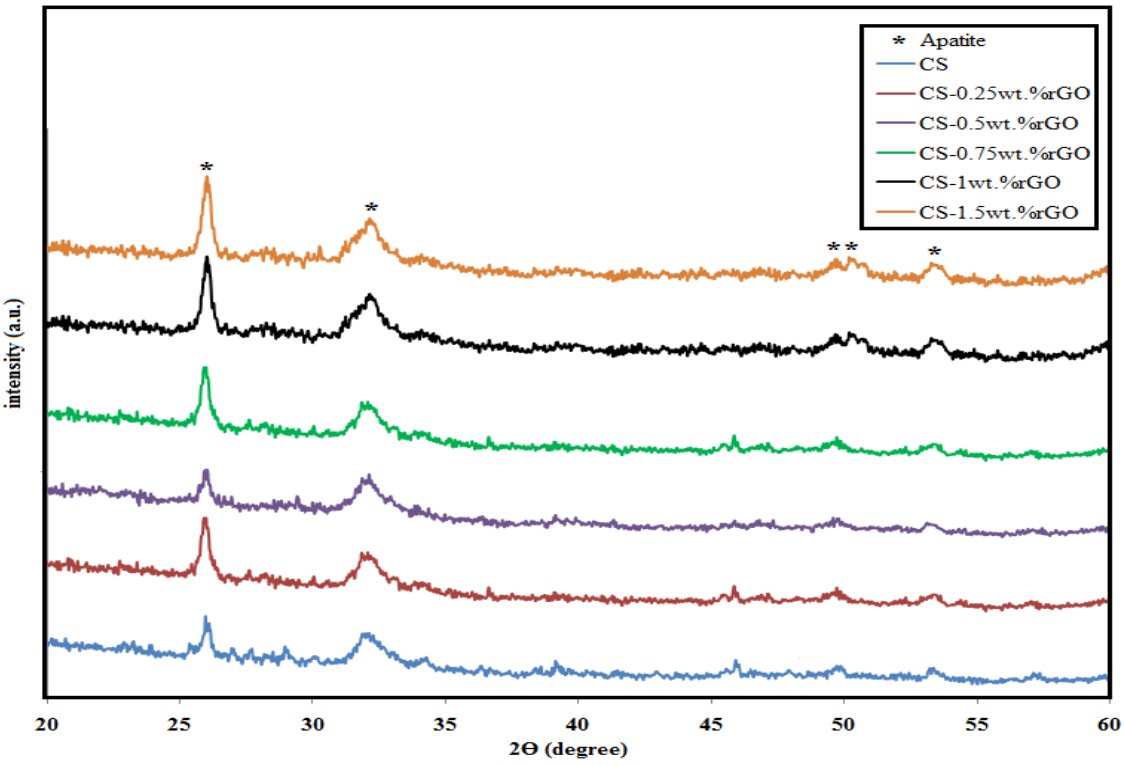

Figure 4.18: XRD patterns of CS-rGO composites after soaking in SBF for 14 days.

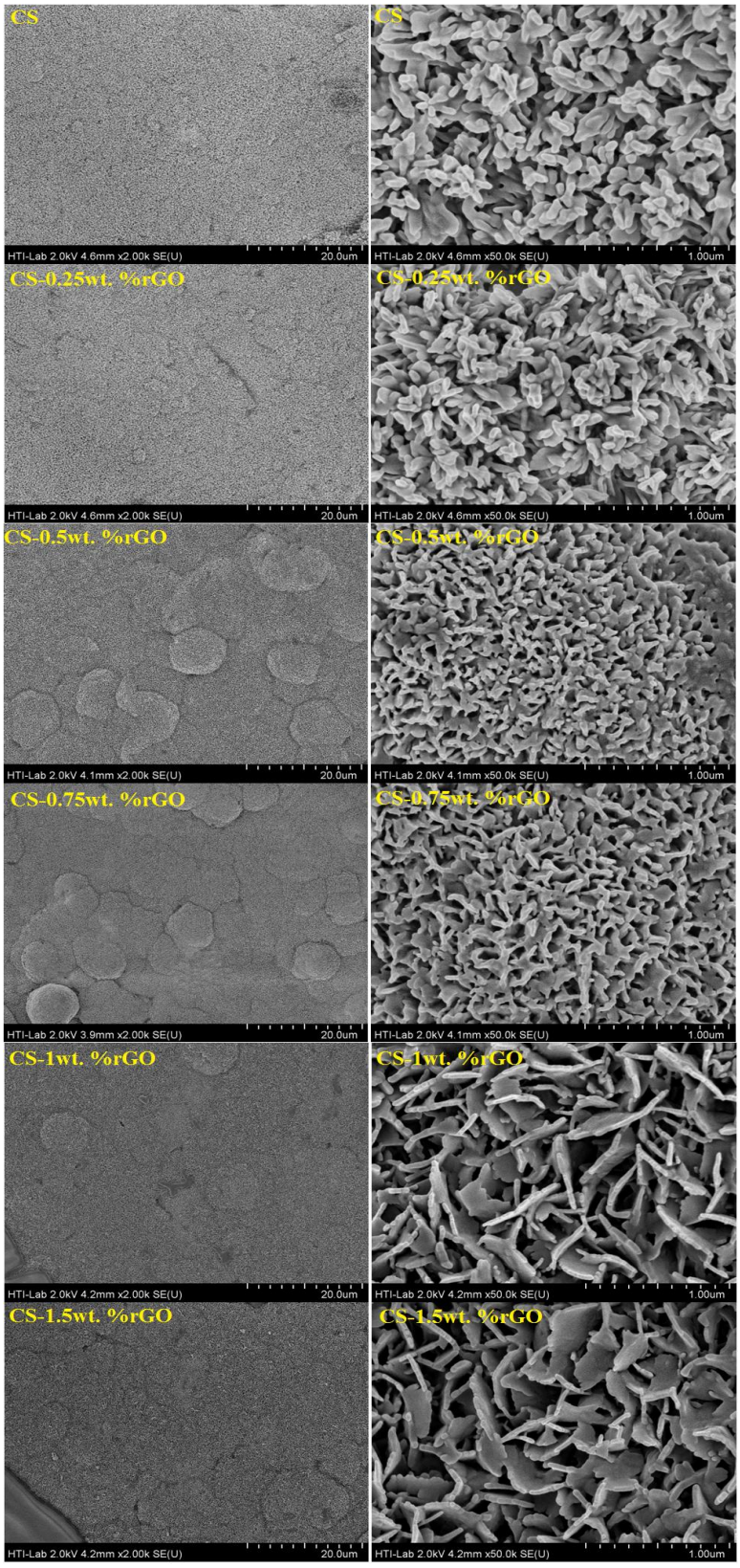

Figure 4.19: Low and high magnification FESEM images of apatite formation on CS-rGO composites immersed in SBF for 7 days.

FESEM micrographs of CS/rGO composites soaked in SBF for 7 and 14 days are presented in Figure 4.19 and Figure 4.20, respectively, at both high and low magnification. The high magnification images in Figure 4.19 demonstrate that after soaking in SBF for 7 days, the surface microstructure varied with rGO concentration. Increasing concentrations of rGO promote the growth of nanosheet-like apatite, while pure CS ceramic exhibited worm-like crystals with the typical HA morphology. After 14 days of soaking, a densely packed HA layer covered the whole surface of the rGO containing samples, while some micro-cracks could also be observed on the composite surfaces due to the shrinkage and desiccation of the soaked samples in air, suggesting the formation of a thick deposit (Ni, Chang, & Chou, 2008; Zhong et al., 2011).

A higher magnification examination of the samples after 14 days of soaking showed that the morphologies of the specimens were similar to those of the samples soaked for 7 days. According to the EDX spectra shown in Figure 4.20, the elements detected were mainly Ca, P and no Si peaks were detected. The Ca/P molar ratio was analyzed for all the samples. The Ca/P molar ratio of the apatite formed on the pure CS and CS/rGO composites is in range of 1.72 and 1.58, close to that of HA, which is 1.67, suggesting that apatite formed on the CS-rGO composites. These results are consistent with the results of XRD analysis and FESEM observation. Altogether, the ability to form apatite on calcium silicate ceramics has not been negatively influenced by the incorporation of reduced graphene oxide.

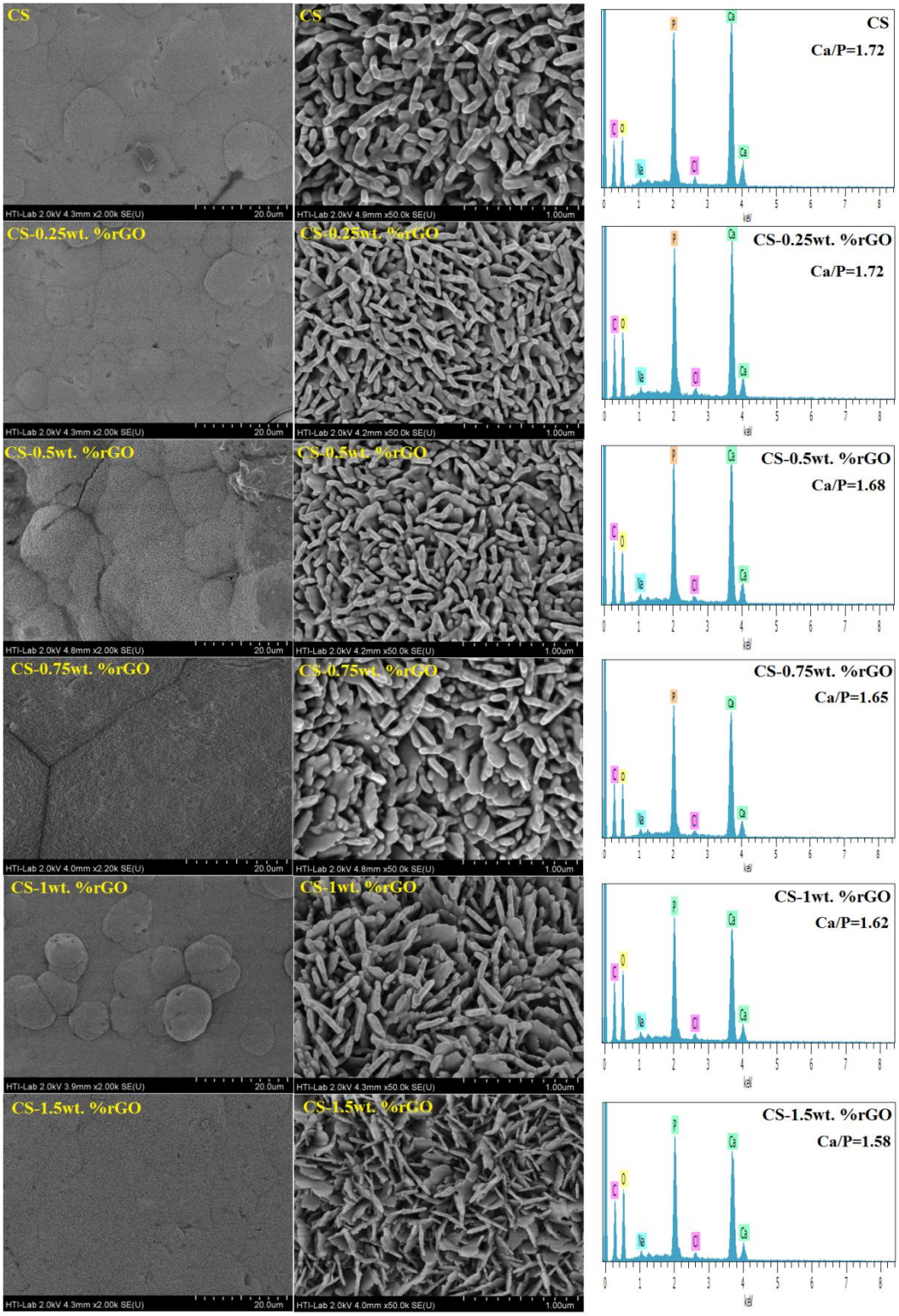

Figure 4.20: Low and high magnification FESEM images of apatite formation on CS-rGO composites immersed in SBF for 14 days.

The concentrations of Si, Ca and P in SBF and the pH of the immersion solutions as a function of soaking time are presented in Figure 4.21. The concentration of Si ions increased slightly with an increasing amount of rGO in the ceramic (Figure 4.21b), while no significant differences were observed in Ca concentration between pure CS and CS/rGO composites as the rGO content was increased (Figure 4.21a). The P concentration continuously decreased during the soaking of the samples in SBF. As shown in Figure 4.21c, the P ion concentration decreases with increasing rGO content. The reduced phosphate concentration can be attributed to the formation of amorphous calcium phosphate and the subsequent formation of HA by incorporating OH^- ions from the SBF, providing an indirect indication that a precipitation reaction occurred (Wei, Heo, et al., 2009). Figure 4.21d shows that the pH of the immersion solution increased for all samples. Previous studies have shown that the release of Ca and Si ions from CS can lead to increased pH of the SBF solution (Y. H. Shen et al., 2011; Shirazi, Moghaddam, et al., 2014; C. T. Wu et al., 2007). In this study, it is observed that the pH of the SBF used to soak rGO-containing CS was lower than that used to soak pure CS ceramic, especially for CS/rGO composites with higher amounts of rGO. This indicates that some acidic by-products were produced during the soaking.
As discussed in FTIR results, for the rGO, the bands associated with the oxygen functional groups decrease in relation to those of GO. Nevertheless, the elimination of these bands is not complete. Furthermore, The FTIR analysis indicated that carboxyl groups and a small fraction of hydroxyl functionalities still remain in the rGO, which can react with atmospheric humidity to form acids. These functional groups may have been the cause for the lower pH upon exposure of rGO to SBF.

CS has been recommended as a material to promote bone tissue regeneration, as it could facilitate the formation of HA layers between living tissue and the implant material (Pan, Zhao, Darvell, & Lu, 2010; C. T. Wu et al., 2007). The bone-like HA

plays a vital role in forming a chemical bond between the bioactive material and the living tissue, and the *in vitro* formation of bone-like HA in SBF predicts a useful bone bonding ability (Gandolfi et al., 2010; Kaur et al., 2014; Pan et al., 2010).

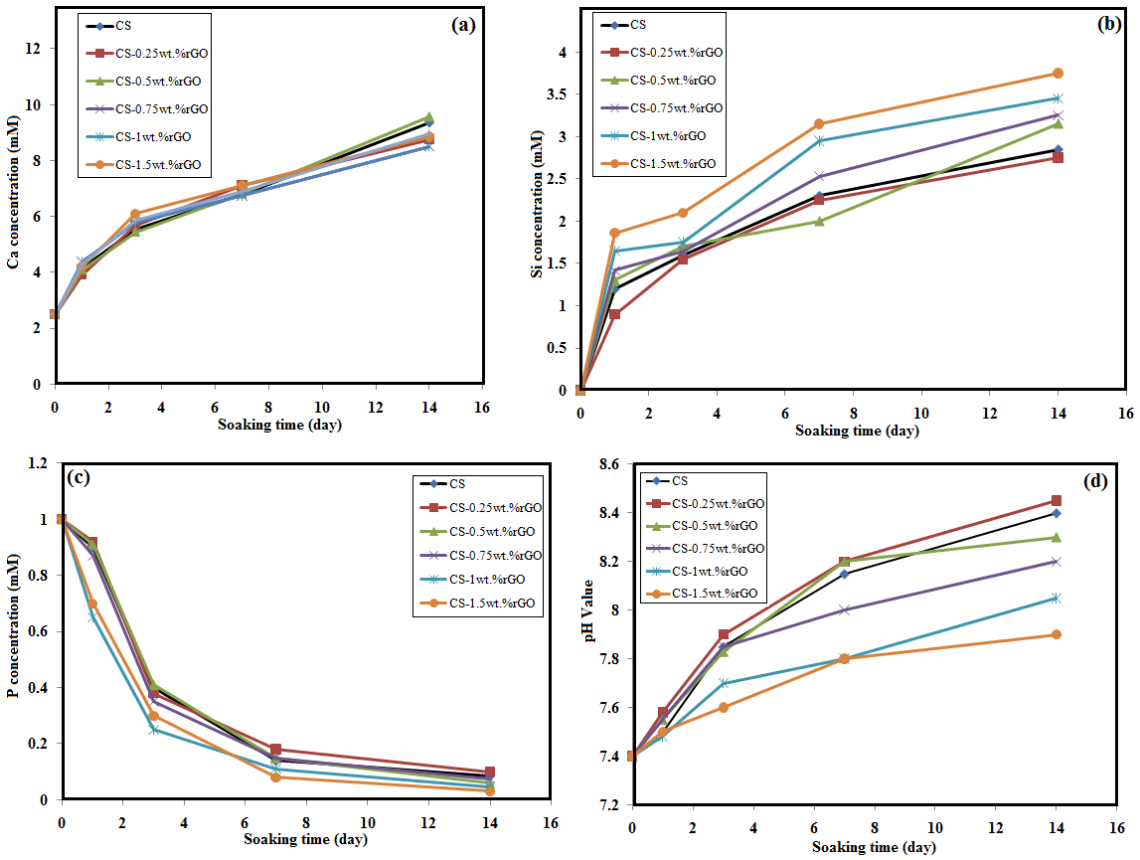

Figure 4.21: The effect of rGO content in CS composites on the Ca (a), Si (b), P (c) ion release, and the change in the pH value (d) in the SBF solution after soaking for various durations.

A number of groups have reported the mechanisms of HA formation on CS surfaces through *in vitro* incubation in SBF solution. Some reports state that an ionic interchange of Ca^{2+} for $2H^{+}$ occurs at the surface, resulting in the formation of an amorphous silica layer on the surface of CS, which provides favorable sites for apatite nucleation (X. Y. Liu et al., 2004; X. Y. Liu et al., 2001). Additionally, the degree of supersaturation of the solution with respect to apatite increases with ion dissolution. Therefore, apatite nuclei are rapidly created on the sample surface, and they

spontaneously grow by consuming calcium and phosphate ions from the surrounding fluid (X. Y. Liu et al., 2004).

In the present study, while the increase in rGO content from 0 wt% to 1.5 wt% did not increase the Ca^{2+} ion concentration in the SBF, a slightly higher Si^{4+} ion concentration was observed in SBF for the composites compared to pure CS. When bone forms, the crosslinking of the collagen chain and the subsequent precipitation of HA are pH-dependent and require an optimal pH at the site of bone formation.(C. T. Wu et al., 2007) Solution pH is also a key factor affecting cell vitality (Pan et al., 2010). These results showed that greater amounts of rGO in CS/rGO ceramics decreased the pH of the SBF due to the exposure of rGO to the SBF. Interestingly, the HA morphology varied among different rGO-containing CS ceramics. This morphological difference of HA grown in SBF-based solutions can be attributed to changes in the ion concentrations and pH in SBF after the soaking of different rGO-containing CS ceramics. These results indicated that CS/rGO composites sintered by HIP also possessed excellent bioactivity and could develop a bone-like HA layer on their surface when soaked in SBF. Moreover, the ability to form apatite on CS ceramics was not influenced by increases in rGO content up to 1.5 wt%, as illustrated by the intensity of the HA peaks on XRD and FESEM. In addition, these results suggest that CS/rGO ceramics have potential applications for *in vitro* bone cell culture.

4.3.5 *In vitro* biocompatibility of CS/rGO composites with osteoblasts

The CS/rGO composite is intended for use in orthopedic implant applications. Therefore, the orthopedic implant should promote cellular adhesion, proliferation, and differentiation. Osteoblasts are able to attach to the orthopedic implant surface. They actively participate in new bone formation by first forming a collagen matrix and then assisting in the deposition of apatite crystal on that matrix. Thus, the growth and proliferation of osteoblast cells on an implant surface plays a crucial role in

osseointegration and in determining the life-time of an implant (Lahiri, Singh, et al., 2011). Thus, the effect of rGO on the growth and proliferation of human osteoblast cells (hFOB) was assessed qualitatively by observing the population of osteoblast cells on the surface after 1, 3 and 5 days of culture.

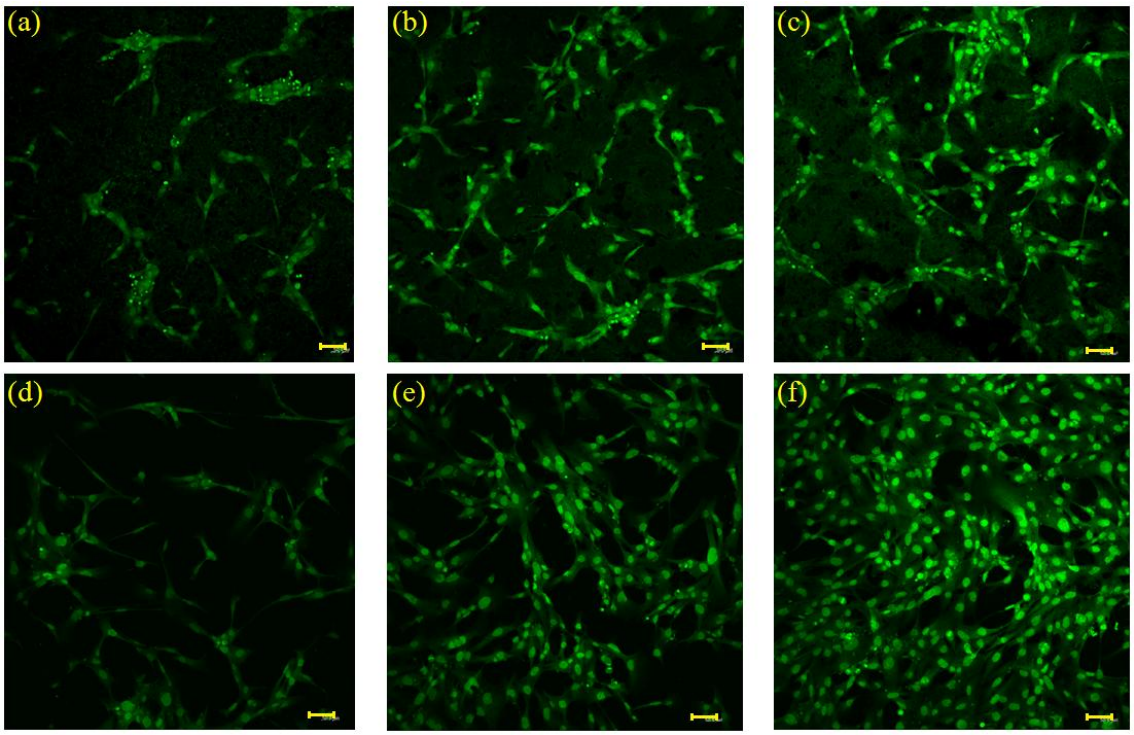

Figure 4.22: Confocal images of adherent hFOB cells on pure CS for 1 (a), 3 (b) and 5 (c) days and CS- 1 wt. %rGO composites for 1 (d), 3 (e) and 5 (f) days incubation. The scale bar represents 50 μm.

Figure 4.22 presents confocal laser scanning microscopy (CLSM) images of hFOB cells cultured on the surface of pure CS and CS-1.0 wt% rGO pellets. The cells exhibit a typical lens shape suggesting normal cell growth. The osteoblast population clearly increases from 1 to 5 days on both surfaces. This observation indicates that CS and CS/rGO surfaces are suitable for osteoblast cell proliferation. Interestingly, more osteoblast cells are attached to the CS/rGO surface than the pure CS surface after 3 and 5 days of culture. Figure 4.23 shows the osteoblast cell morphology on pure CS and CS/rGO composites after 24 hours of culture. In general, the hFOB cells on all the CS/rGO composites are observed to be globular, flat and actively spreading with a

number of filopodia protrusions, an indication of a normal cell attachment and growth process (A. Kumar, Webster, Biswas, & Basu, 2013).

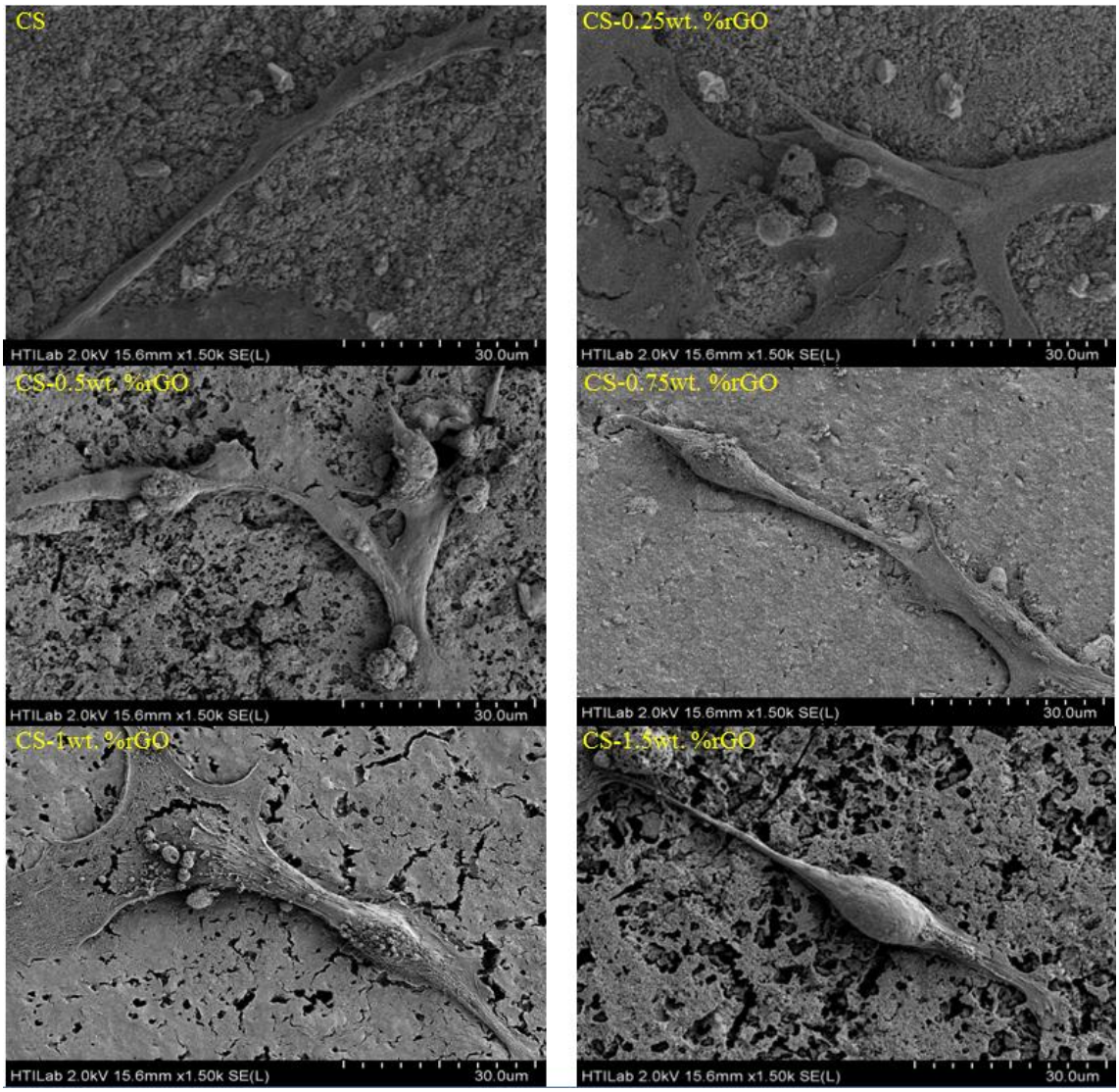

Figure 4.23: FESEM illustrating the morphology of hFOB cells seeded on pure CS and CS-rGO composites after 24 hours.

Extracellular matrix (ECM) was secreted by the seeded hFOB cells, and the cells merged on the surface of CS/rGO composites to form cell layers. Merging induced the formation of a rich ECM, indicative of high cell activity on the CS/rGO composites. Bone is produced by the mineralization of an organic matrix (largely collagen) through the nucleation and growth of a mineral similar to HA (Gandolfi et al., 2010). Thus, the presence of calcium phosphate in the ECM acts as a key factor in the regulation of bone remodelling and cartilage (A. Kumar et al., 2013). Mineralization of hFOB cultured on

CS-1wt. %rGO composite after 3 days cell culture was observed by FESEM, as shown in Figure 4.24b. In the present study, the EDX pattern of hFOB cells on the CS-1wt. %rGO indicated the formation of a calcium phosphate based on the preponderance of Ca and P elements as presented in Figure 4.24c. In addition, the Ca/P molar ratio on the surface of merging cell layers was 1.64 and was approximately equal to the 1.67 ratio of HA, suggesting that the calcium phosphate formed in the ECM mainly consisted of apatite, which is the major inorganic composition of bones and cartilages. Therefore, it is plausible to suggest that the CS/rGO composite is expected to be suitable for bone regeneration.

Cell viability was studied with an MTT assay by seeding osteoblasts onto the rGO- containing CS for 1, 3 and 5 days, and the results are summarized in Figure 4.25. The MTT activity increased with incubation time, indicating that proliferation proceeded on all specimens. In other words, rGO addition did not exhibit any obvious effects on cell proliferation. Interestingly, the number of cultured cells increased significantly with increasing rGO concentration. As an increase in cell number is preferred over an increase in osteoblast activity, the initial proliferation and recruitment of cells to the implant surface is important. This finding is consistent with recent reports by other researchers that incorporation of graphene or rGO into silica, HA and chitosan leads to better adherence and stimulated proliferation of human osteoblasts and mesenchymal stromal cells than on pure silica, HA and chitosan (H. L. Fan et al., 2010; Kalbacova et al., 2010; M. Li et al., 2013).

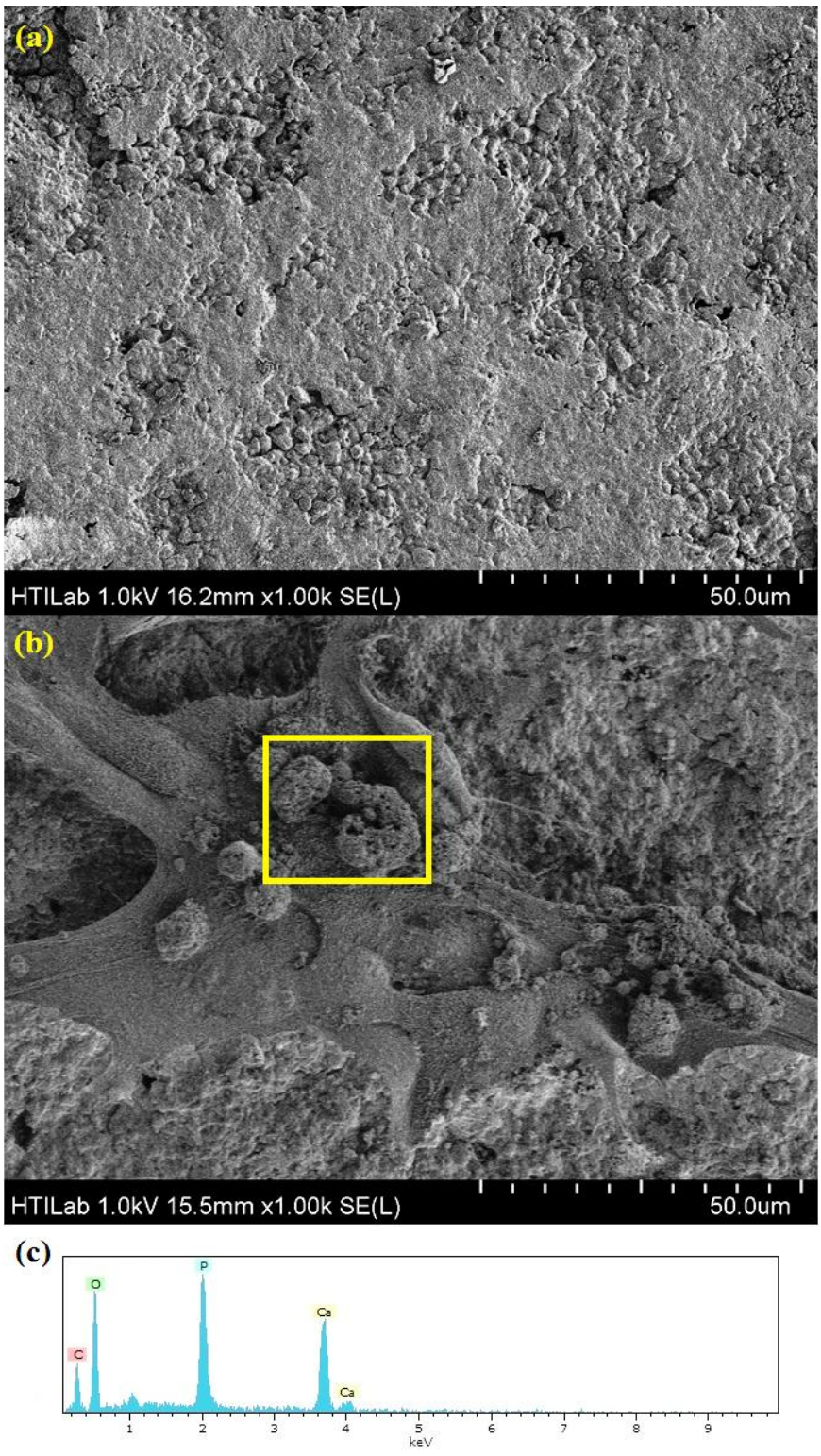

Figure 4.24: (a) CS-1 wt% rGO composite without cells. (b) hFOB cells grown on CS-1 wt% rGO composite after 3days. (c) EDX spectra of the hFOB cells in the boxed region that is showing a significant presence of P and Ca on the CS-1 wt% rGO composite after 3days seeding.

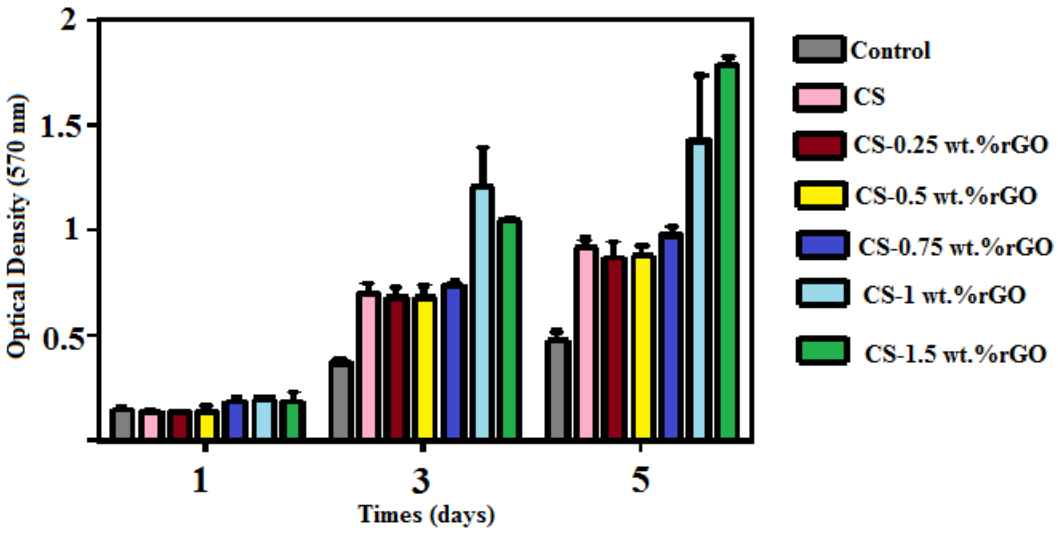

Figure 4.25: Cell culture results for the CS-rGO pellets. The hFOB cells cultured on the sample surfaces exhibit enhanced proliferation with an increased content of rGO in the composites.

To better understand the effect of rGO on the behavior of the hFOB cells, osteoblast differentiation is one of the most important steps in overall cellular activity and thus bone formation ability. Thus, the effects of rGO on osteoblast differentiation were evaluated using an alkaline phosphate activity (ALP) assay, which is an early marker of osteoblast differentiation. Figure 4.26 shows the proliferation and ALP activity of the hFOB cells cultured on pure CS for 7 days. The cells cultured for 7 days on the pure CS and CS/rGO composites exhibited significantly higher ALP activity than the blank well plate. The ALP activity of the cells on the composites markedly increased with increasing rGO content in the composites. The ALP expression level on the CS–1 wt. % rGO composite was approximately 1.5 times higher than that on the pure CS ceramic.

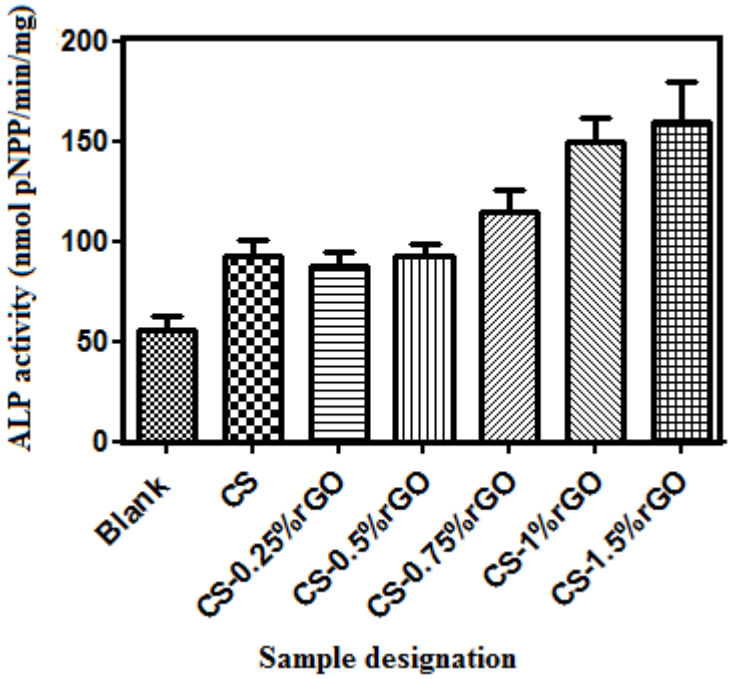

Figure 4.26: The ALP acftivity of hFOB cells after cultivation on different CS-rGO composites for 7 days.

The cell attachment, proliferation and differentiation data for pure CS and CS/rGO composites demonstrate a high degree of CS/rGO composite–osteoblast interaction and indicate that this is a successful *in vitro* model to study bone cell–biomaterial interactions. Previous studies found that the Ca and Si ions released from materials stimulate osteoblast differentiation, gene expression and proliferation, which can be regarded as one of the evaluation criteria for bioactivity (Gandolfi et al., 2010; Xynos, Edgar, Buttery, Hench, & Polak, 2000). Furthermore, the ALP activity and osteocalcin levels increased when Si was exposed to human osteoblasts (C. T. Wu et al., 2008). These results showed that Si concentrations in SBF increased with increasing rGO content, while the amount of Ca ion released was approximately equal to that of pure CS. Note that the pH value has multiple effects on osteoblast metabolism and function, with a pH value of 7.6 increasing osteoblastic collagen synthesis (Silver, Deas, & Erecinska, 2001; C. T. Wu et al., 2008). These results indicated a smaller increase in the pH of SBF due to increased rGO content in the CS ceramic, which can be desirable

for cell growth. Moreover, recent reports indicate other influences of graphene on the cell viability, proliferation and gene expression of osteoblasts. Chen et al. (G. Y. Chen, Pang, Hwang, Tuan, & Hu, 2012) reported that graphene can support induced pluripotent stem cell (iPSC) culture and allow for spontaneous differentiation. The graphene surface led to distinct cell proliferation and differentiation characteristics.

Their data demonstrated that the surface properties of graphene governed the iPSC behavior and indicated the potential of graphene-based materials as a platform for iPSC culture and other applications. Kalbacova et al. (Kalbacova et al., 2010) indicated that the electrical conductivity of graphene is particularly important because electricity, cocktails of growth factors, and substrate properties are able to stimulate cell growth and differentiation. Additionally, a very recent study suggested that the cell viability of rGO depended on the lateral size of the sheets (Akhavan, Ghaderi, & Akhavan, 2012; H. Zhang et al., 2013).

Taken together, the results of the present work demonstrate that rGO possesses sufficient biocompatibility for use as a biomaterial and that the addition of rGO into the CS matrix is remarkably effective in improving the cellular response to the CS ceramic.

4.4 Calcium silicate– graphene nanoplatelets composites

In this part of the research, GNP-reinforced calcium silicate composites are studied to understand the role of GNP in microstructural evolution of CS-based composite during HIP process. This is carried out by studying the grain size and porosity and correlating with the physical properties of GNPs. The effect of GNP modified microstructure and CS/GNP interface on elastic modulus, hardness and fracture toughness of the composite is also elucidated.

The effect of GNP content on the formation of HA on CS/GNP composites during soaking in a biomimetic system of simulated body fluid (SBF) were also assessed. Moreover, the effect of addition of GNP on cytotoxicity, cell attachment,

morphology of cells and proliferation of human osteoblast cells (hFOB) was measured in vitro by an MTT assay.

4.4.1 Selection of surfactant and mixed powders

The pristine GNP and CS /1wt. % GNP composite powders were analysed prior to sintering in order to evaluate the effectiveness of the mixing and processing. As revealed by TEM analysis, GNP exhibits a flake structure with various in-plane sizes and indicated well-ordered graphene layers. Moreover, the thickness of GNP is less than several nanometres. Figure 4.27b shows the dispersion of GNPs, which were distributed homogeneously in the CS powder. In this experiment, CS powder without any surfactant does not show a good dispersion with GNP. Therefore, we employed 1.0 wt % CTAB as a dispersant to disperse GNP in the CS powder. CTAB is a cationic surfactant. It can completely ionize in solution. Walker *et al*. (Walker et al., 2011) reported that the dispersion of GNP using CTAB occurs because the hydrophobic GNP is attracted to the hydrophobic tails of the surfactant. As a result, GNP is covered in positively charged surfactant molecules. On the other hand, CS generally has a negative charge due to a deficiency of calcium ions, resulting in CS powders that are attracted to the GNP surface owing to electrostatic interaction once the GNP suspension was mixed, hence avoiding the agglomeration of the graphene nanoplatelets and leading to uniform dispersion of GNP in the CS powders.

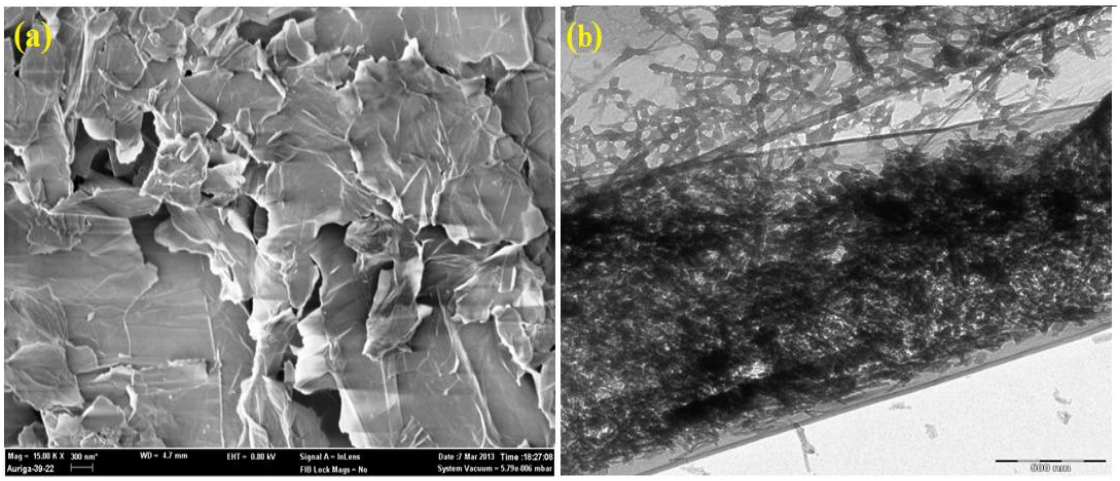

Figure 4.27: (a) FESEM micrograph of wrinkled top surface of GNPs, (b) TEM of CS/GNP powder mixture showing the CS particles are well-dispersed throughout the surface area of the graphene sheets.

4.4.2 XRD and Raman characterization of CS/GNP composites

The XRD patterns of the CS/GNPs composites sintered at 1150 °C by HIP with different amounts of GNP are shown in Figure 4.28. These diffraction patterns demonstrate that only α-$CaSiO_3$ phase existed (Standard cards no JCPD 31-0300) in pure CS and CS /GNPs. The patterns are similar, indicating that the incorporation of GNP has no effect on the crystal phase composition of CS. Meanwhile, GNPs are present in minor quantities and are difficult to detect by XRD.

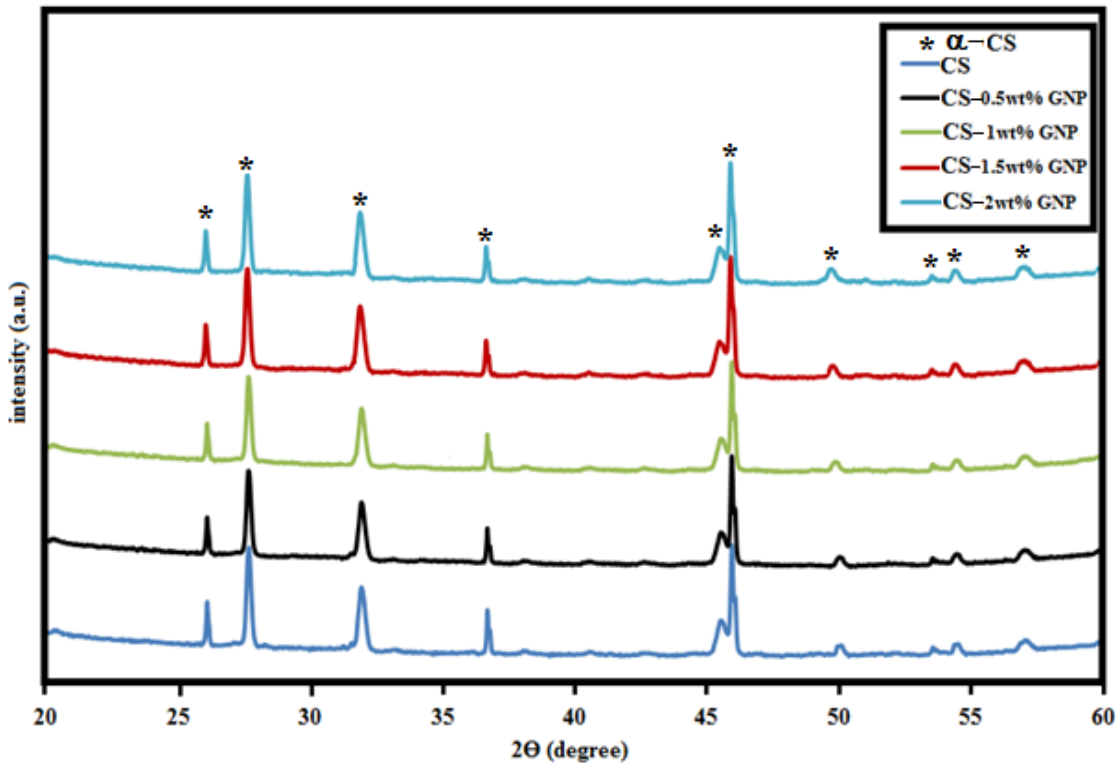

Figure 4.28: XRD results of pure CS and CS/GNP composites with different amounts of GNP after sintering at 1150 °C by HIP.

The pristine GNPs and CS/1 wt %.GNPs before and after HIP consolidation were analysed using Raman spectroscopy to verify the existence, and evaluate the structure of GNP in the consolidated structure after exposure to high temperature and pressure. Figure 4.29 and Table 4.4 display the presence of D, G and 2D peaks. The D peak was associated with the presence of disorder in the aromatic structure or the edge effect of graphene, the G peak is from in-plane C-C bond stretching in graphene, and the 2D peak is related to the thickness and also used to determine the number of graphene layers (Ferrari & Basko, 2013; Lv Zhang et al., 2013).

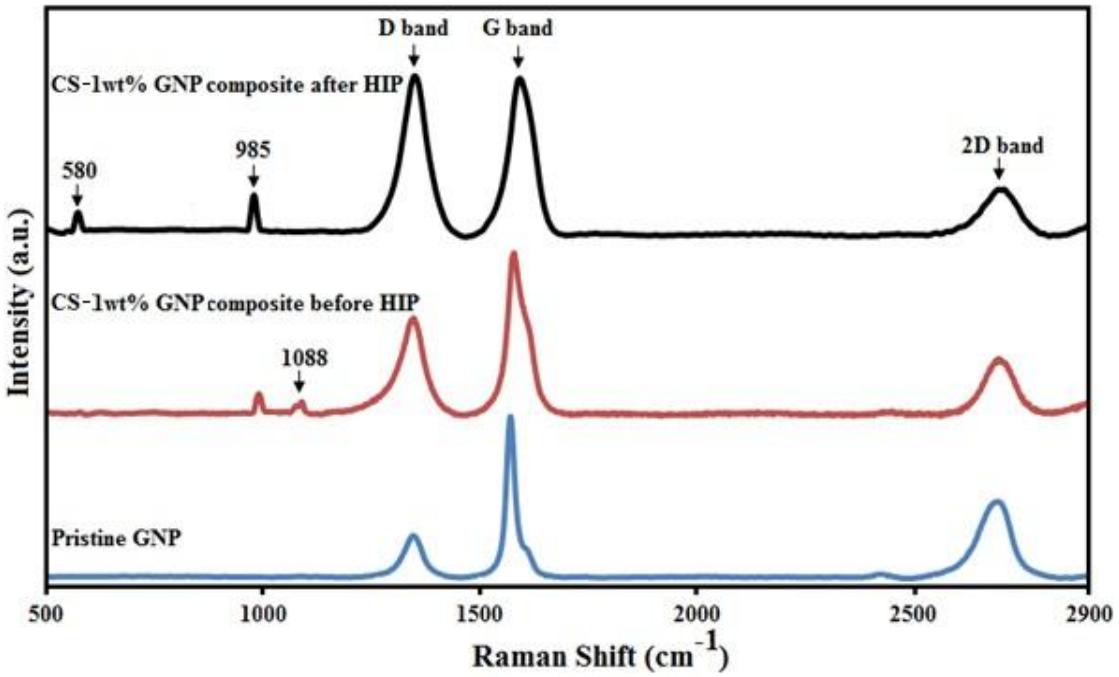

Figure 4.29: Raman spectra of pristine GNP, CS/GNP composite (1 wt. % GNP) before HIP and CS/GNP composite (1 wt. % GNP) after HIP.

The presence of G and 2D peaks in the GNP/CS composite confirms the retention of GNP after HIP consolidation. The pristine GNP showed a D-band around 1347 cm^{-1}, G-band around 1570 cm^{-1} and 2D peak ~2690 cm^{-1}. After mixing of GNP and CS powders by ball milling, D and 2D peaks have shifted to higher wave numbers of 1580 cm^{-1} and 2700 cm^{-1}, respectively. Moreover, It can be seen that the D, G, 2D peaks in the CS/1wt.% GNP composite after sintering have shifted to higher energies, especially the G band exhibited a blue-shift from 1570 to 1595 cm^{-1} after HIP . The spectral blue-shifts could be ascribed to the disturbing of the graphene structure caused by the compressive stresses acting on GNP, incurred during thermal contraction of CS matrix (Tsoukleri et al., 2009). The intensity ratio of the D to G-bands (I_D/I_G) is a measure of the degree of disorder, the larger the ratio the more defects present (Geim & Novoselov, 2007).

Table 4.4: Peak position of the D and G bands and intensity ratios of I_D/I_G and I_{2D}/I_G.

Samples	D band (Rman shift)	G band (Rman shift)	2D band (Raman shift)	I_D/I_G	I_{2D}/I_G
GNP	1347	1570	2690	0.26	0.48
CS/1wt% GNP before HIP	1347	1580	2700	0.59	0.34
CS/1wt% GNP after HIP	1350	1595	2700	1	0.3

As shown in Figure 4.29 and Table 4.4, the I_D/I_G ratio of pristine GNP, CS/1wt.% GNP powder and CS/1wt.% GNP composite after HIP were 0.26, 0.59 and ~1, respectively, implying that the ball milling and HIP process introduces structural defects into GNPs. The ball milling of GNP/CS powders leads to strong interactions between GNP and CS particles. These interactions appear to have adverse effects on the GNP resulting in a higher I_D/I_G ratio indicating partial loss of the graphene-like structure. Nevertheless, the presence of G and 2D peaks in the CS/GNP powder exhibited the existence of a graphene-like structure. Also, the I_{2D}/I_G intensity ratio of 1wt. % GNP/CS powder before HIP processing decreased from 0.48 to 0.34 compared to pristine GNP, indicating an increase in the number of graphene layers due to mixing process (Baradaran et al., 2014). Furthermore, our results indicate that the I_{2D}/I_G values of CS/1wt.% GNP powders and CS/GNP slightly decreased from 0.34 to 0.3, illustrating a further increase of the number of graphene layers after HIP process (A. Nieto et al., 2012). Thus, Raman spectroscopy demonstrates that the GNP structure is retained after HIP consolidation. The spectrum of the CS/GNP powder before sintering exhibits peak representing the β-CS phase at 1088 cm^{-1}, which can be attributed to the Si−O−Si asymmetric stretching mode (ν_{as}(Si−O−Si)) and 985 cm^{-1} is attributed to Si-O stretching vibration (Garbev et al., 2007). In addition, two characteristic Raman peaks

for the α-CS at 580 and 985 cm^{-1} were detected in CS/1wt.% GNP composites after the HIP process and are attributed to Si-O-Si bending vibration and at the Si-O stretching vibration, respectively (Colomban, 2004).

4.4.3 Physical and mechanical properties of CS/GNP composites

Pure CS and CS/GNP achieved high degrees of densification after HIP, with relative densities ranging from ~90% to 98.5%. Figure 4.30b is a plot of the relative density of the CS/GNP composites, shown as a function of the GNP concentration.

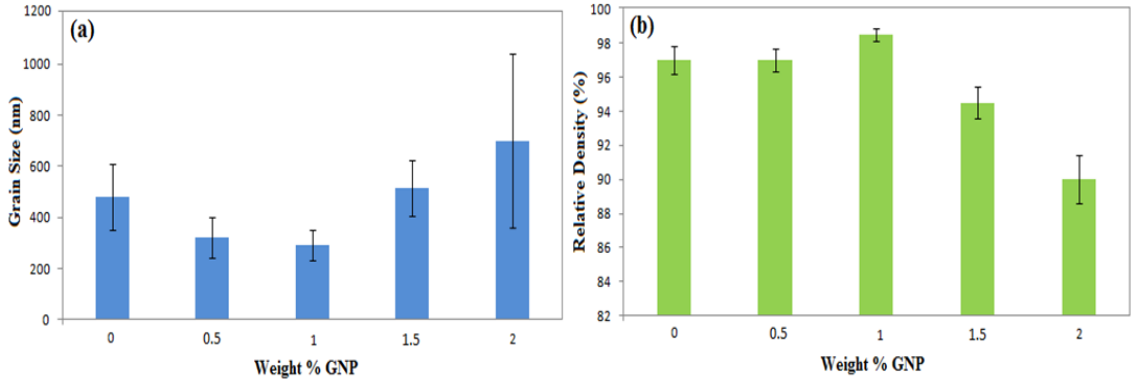

Figure 4.30: The effect of the GNP on the grain size and densification. (a) Grain Size vs. GNP content. (b) Densification (relative to theoretical density) vs. GNP content.

The addition of GNP influences the density of the composite; the pure CS sample reached a density of ~97 % whereas 1 wt% GNP containing CS has a density of ~98.5 %, however when the content GNP increases further (1.5 and 2 wt %) the relative density of the composite decreases. GNP has a much higher thermal conductivity (5300 W/mK) (A. Nieto et al., 2012) than CS, which makes it possible for the composite to have a more uniform distribution of the temperature during sintering. The consistent heating of the powders leads to improved densification. However, these results indicate that the incorporation of 1 wt% GNP into CS achieved the highest density.

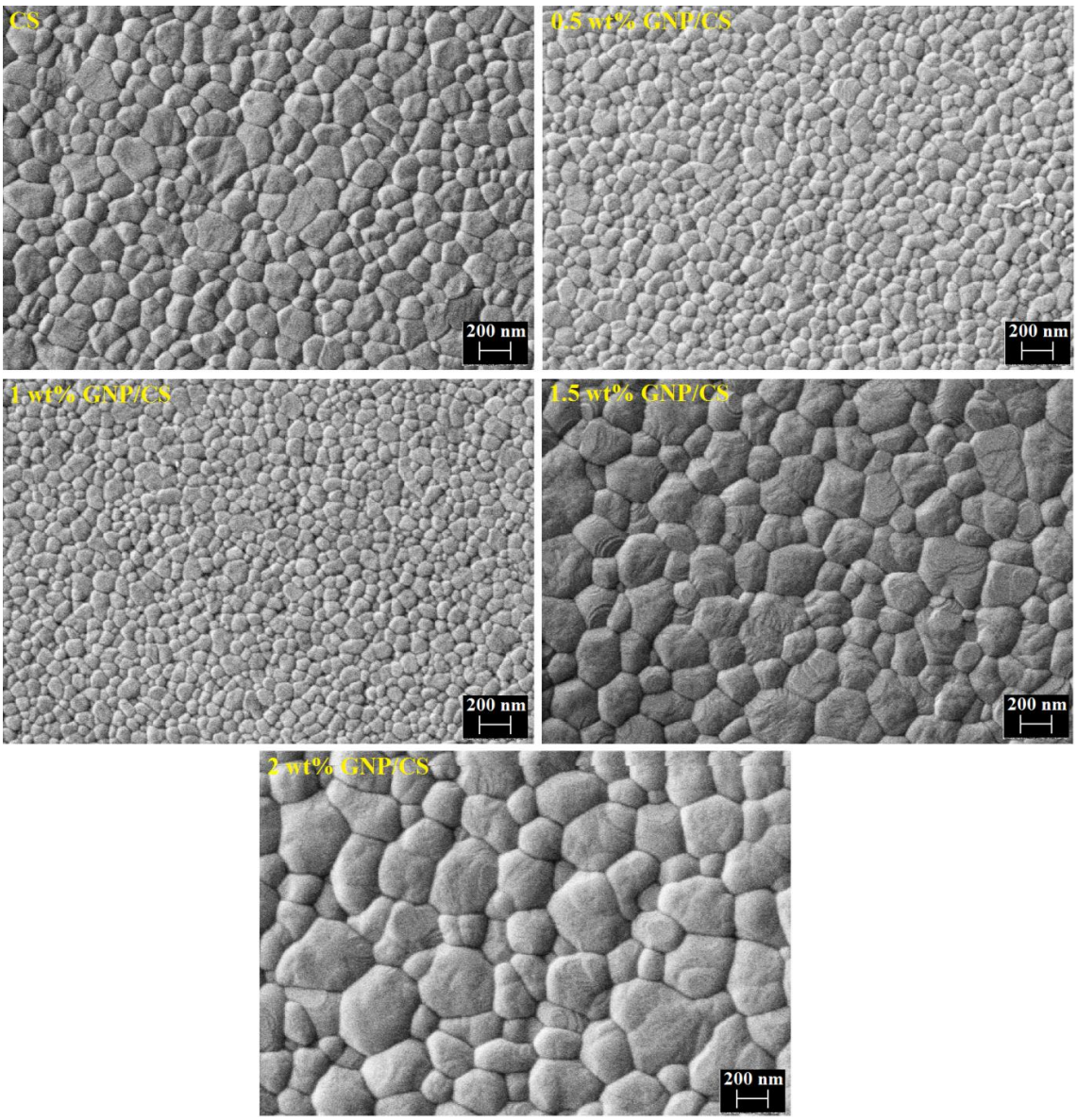

Figure 4.31: FESEM images of thermally etched surfaces for pure CS and CS/GNP ` composites.

Figure 4.31 shows the polished and thermally etched surfaces of CS/GNP composites. In addition, the mean grain size with varying GNP content is plotted in Figure 4.30a. As can be seen from the FESEM images and the grain size analysis, the different amounts of GNP have an effect on the grain size. Significant grain refinement occurred for 0.5 and 1 wt% GNP composites, where the grain sizes were reduced by over 40% relative to the pure CS. Similarity, a recent study by Nieto *et al.* (Andy Nieto

et al., 2013) has shown that the GNP can influence and reduce the grain size of tantalum carbide.

This is attractive for ceramics, as grain size refinement could simultaneously increase fracture toughness and hardness of the ceramic due to the change of cracking mode from transgranular to intergranular and the deflection of propagating cracks (Lahiri, Ghosh, et al., 2012). The concentration of GNP in CS/1 wt% GNP is satisfactory for grain refinement and to hinder grain growth throughout the structure. The generated fine-grained structure is due to the grain boundary pinning action of GNP. Moreover, the high thermal conductivity and high surface area of GNP allow for strong interfacial bonding between CS grains and GNP, which minimizes porosity formation. On the other hand, at high amounts of GNP (1.5 and 2 wt %), the grain size increased. Further increase in GNP content causes agglomeration, which may lead to increasing thermal conductivity but not necessarily of providing effective grain pinning and wrapping.

Table 4.5: Mechanical properties of pure CS and CS/GNP composites

Sample	Elastic modulus (GPa)	Micro-hardness (GPa)	Nano-hardness (GPa)	Fracture toughness (MPa m1/2)	Brittleness index ($\mu m^{-1/2}$)
CS	110±9	5.75±0.06	6±0.6	0.78±0.18	7.37
CS/0.5 wt% GNP	112±8	6.38±0.03	6.88±0.15	1.08±0.07	5.9
CS/1 wt% GNP	121±8	7.45±0.11	7.71±0.19	1.71±0.05	4.21
CS/1.5 wt% GNP	104±8	5.58±0.19	5.7±0.5	1.35±0.07	4.13
CS/2 wt% GNP	94±5	4.6±0.3	4.9±0.8	1.30±0.13	3.54

The mechanical properties of pure CS and the GNP reinforced CS composites are compiled into Table 4.5. The modulus of elasticity of pure CS (110±9) in the high-temperature phase (α-CS) is at the higher end of values reported in the literature (Long et al., 2006; Long et al., 2008; Shirazi, Mehrali, et al., 2014). The modulus of elasticity increased slightly for 0.5 and 1 wt. % GNP composites, but decreased for 1.5 and 2 wt. % GNP content. The increase in the modulus of elasticity of 0.5 and 1 wt. % GNP samples is due to the high modulus of elasticity of graphene, the high relative density, and smaller grain sizes. On the other hand, porosity has been reported to be a major factor governing the modulus of elasticity for some ceramic materials, with greater porosity correlated with a lower modulus of elasticity (X. J. Zhao et al., 2011). This explains the reduction of the modulus of elasticity in 1.5 and 2 wt. % GNP/CS samples. The modulus of elasticity of human cortical bone is reported to be in the range of 15–25 GPa , while the modulus is much higher for consolidated pure CS and our composites. A mismatch of the modulus of elasticity at the bone–implant interface might pose a risk of fracture or delamination of the implant (Shirazi, Mehrali, et al., 2014). Nevertheless, the osseointegration ability of CS creates strong bonding at the CS–bone interface, thus decreasing the chance of fracture and delamination. Likewise, an increase in the modulus of elasticity directly influences the improvement in the fracture toughness in ceramic-based composite materials (Lahiri, Ghosh, et al., 2012).The hardness was assessed using Vickers indentation method at load 1 *K*g and nanoindentation experiments, and illustrated in Table 4.5. It is clearly seen that the hardness for CS/1 wt. % GNP composite shows an improvement of ~30%, as compared to pure CS. Our results indicate that addition of up to 1 wt. % GNP improves the hardness of CS due to strengthening of the matrix and grain size refinement, both of which prevented plastic deformation. It is noteworthy that the hardness is reduced at 1.5 and 2 wt. % GNP/CS composites due to increased porosity and growing average grain size (Figure 4.31).

In this study, the addition of GNP to CS results in an improvement in the indentation fracture toughness as shown in Table 4.5. The fracture toughness is increased by ~130% in the CS/1 wt. % GNP composite. The increase in toughness correlates with increasing GNP content, but this trend does not continue for 1.5 and 2 wt. % GNP due to the high porosity, which is believed to provide nucleation sites for fracture and to weaken the strength of the ceramic composites. This may explain the fact that the addition of more than the optimum amount of GNP led to less strong composites (J. Liu, H. X. Yan, & K. Jiang, 2013).

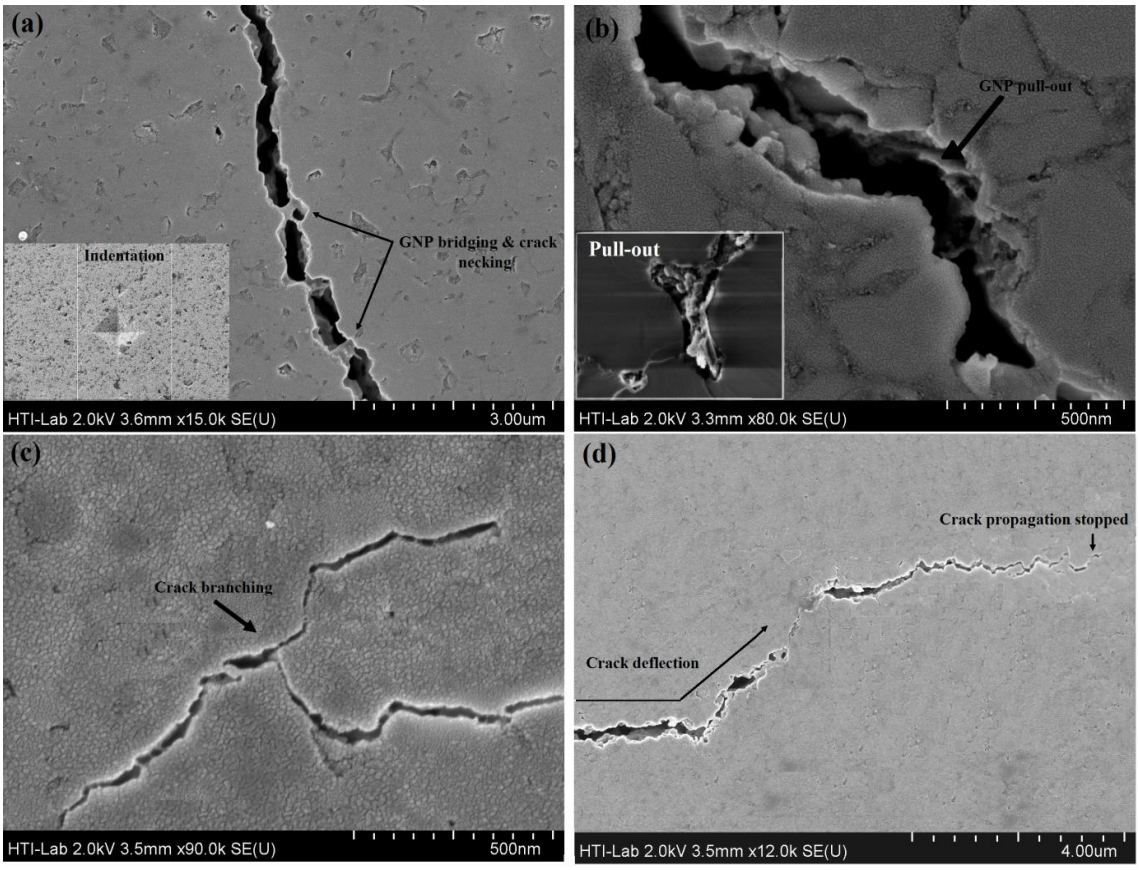

Figure 4.32: GNP toughening mechanisms in CS, (a) Micro hardness indent resulting in the creation of radial cracks (inset image). Closer examination of the radial cracks revealed GNP bridging, (b) sheet pull-out, (c) crack branching, (d) crack deflection.

The surfaces of the CS/GNP composites were analysed using FESEM in order to develop a comprehensive understanding of the contribution of the added GNP to the improved fracture toughness. As depicted in Figure 4.32a illustrates the indentation-induced crack propagation on the polished surface of GNP/CS composite, when a crack propagates and meets with GNP, which acts as a bridge and restricts the widening of the crack. GNP bridges need more energy for opening up of the cracks and this caused toughening. Hence, the crack propagating through CS gets restricted when it comes in the proximity of GNP, and consequently a higher energy is required for GNP debonding. Other studies have also observed that graphene bridging is an effective mechanism for the toughening of ceramics–graphene composite structure (J. Liu et al., 2012; Walker et al., 2011; Lv Zhang et al., 2013). Figure 4.32b shows that once a crack propagates through the CS matrix and finds a GNP across its path, the ridges on the GNP surface may be the first to experience pull-out resulting in energy dissipation, because of binding and friction which, subsequently, leads to toughening. Moreover, probing within the cracks (inset image), one can observe direct evidence of GNP pull-out and GNP sheets that are bridging the cracks. Figure 4.32c and d show the intrinsic GNP branching and deflection mechanisms. It is believed that when a crack propagates through the matrix and reaches a GNP across its path, the crack gets deflected and absorbs some energy by creating a more tortuous path to release stress, resulting in toughening of the matrix. Moreover, Deflection of crack and transition of cracking mode from transgranular to intergranular are the reasons for the improvement in fracture toughness of CS with refined grain size.

The brittleness index can be used to quantitatively assess the machinability of ceramics. Boccaccini reported that the good machinability occurs when the brittleness index of the ceramic is lower than 4.3 $\mu m^{-1/2}$ (Boccaccini, 1997). Meanwhile, the lower the brittleness index, the better the machinability of the ceramics. Our results

show that the GNPs are very effective in lowering the BI of CS. In the case of 1 wt. % GNP/CS composite the BI value decreased from 7.37 to 4.21 $\mu m^{-1/2}$, corresponding to a ~40% decrease compared to pure CS. Another interesting observation is that the plot shows a systematic decreased in BI with increasing GNP concentration. Porwal *et al*.(H. Porwal et al., 2013) reported that the graphene oxide nanoplatelets (GONP) has significant influence to reduce the BI and consequently improve the machinability performance in silica/GONP composites in comparison with pure silica. Overall, our results are in good agreement with results of Porwal *et al* (H. Porwal et al., 2013).

4.4.4 *In vitro* HA forming ability of CS/GNP composites

The principal consideration for a biomaterial to be used for hard tissue replacement implants depends on two factors: good osseointegration of the implant in pristine bone, and admirable biocompatibility of the implant material for the growth promotion of osteoblast cells (Kaur et al., 2014). A homogeneous distribution and fast apatite formation rate implies a strong bone-bonding ability between the implant and surrounding tissues. Figure 4.33 shows the XRD patterns of pure CS and GNP/CS composites after soaking in the SBF solution for 14 days. Only the characteristic peaks of hydroxyapatite (Standard Card No: JCPD 24-0033) were obvious and there was no difference in the intensity of peaks with different GNP contents in CS matrix after a prolonged soaking time of 14 days. All diffraction peaks of CS disappeared and broad peaks were detected at 2Ɵ= 31.7°, 2Ɵ= 49.5°, 2Ɵ=53.2°, with a strong peak at 2Ɵ= 26°, corresponding to the (2 1 1), (2 1 3), (0 0 4) and (0 0 2) planes of hydroxyapatite (HA), respectively. This suggests that more HA is formed on the surface of composites; and based on the shape of the peaks, this HA should be nanocrystalline in nature. Furthermore, no cristobalite or other peaks were detected in any samples soaked in SBF.

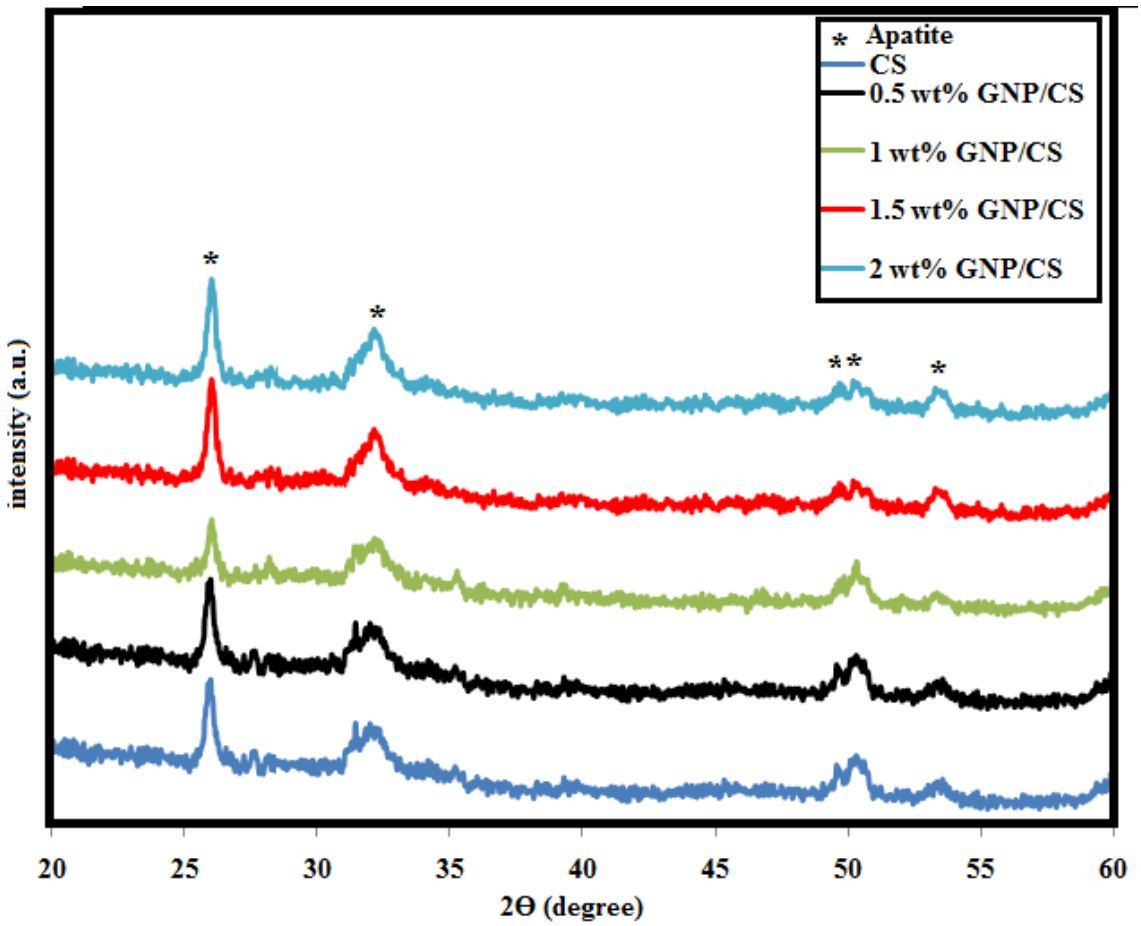

Figure 4.33: XRD patterns of pure CS and CS/GNP composites after soaking in the SBF solution for 14 days.

Figure 4.34 demonstrates the representative surface morphologies of pure CS and the CS/GNP composites after being soaked in SBF for 14 days. At low magnification, the apatite deposits on all samples showed typical spherical granules in density packed HA layers and the surfaces were fully covered by apatite. The higher magnification FESEM micrographs revealed that the morphology of mineralization product varies with addition of GNP into the CS matrix. Worm-shaped-like HA was formed on pure CS sample, whereas nano-sheet-like apatite forms on CS/GNP composites. Liu *et al.* (X. Y. Liu et al., 2004) demonstrated that the mechanism of apatite formation on the CS surface involves dissolution of Ca^{2+} ions from the CS surface and leaving a Si-OH layer, which provided favourable sites for HA nucleation.

On the other hand, the degree of supersaturation of the solution with respect to apatite increased with the dissolution of ions. Thus, the apatite nuclei were formed on the sample surface, and they spontaneously grew by consuming Ca^{2+} and HPO_4^{3-} ions from the surrounding fluid. Figure 4.35 shows that the incorporation of GNP into CS decreases the pH value in SBF solution compared to pure CS. Several research groups reported that the pH value has multiple effect on HBDC metabolism and function, where a pH value of 7.6 increased osteoblastic collagen synthesis, which is also critical factor for osteoporotic bone regeneration (Y. H. Shen et al., 2011; Silver et al., 2001). The most significant and interesting finding is that when bone forms, the cross linking of the collagen chains and the subsequent precipitation of HA are pH dependent and require an optimally alkaline pH at the bone formation site (Silver et al., 2001). Liu *et al.* (X. Y. Liu et al., 2004) believed that the pH value of the resultant SBF solution increased, due to the ionic exchange between calcium ions in CS and H^+ in SBF. The results showed that, the value of pH of the SBF is higher over pure CS than over CS/GNP composites. For instance, the addition of 0.5 or 2 wt. % GNP into CS reduces the pH value of SBF from 8.75 to 8.40 and 7.65, respectively. This is because the graphene nanoplatelets have naturally occurring functional groups like ethers, carboxyls, or hydroxyls that can form acids and reduce the pH when the exposed GNPs are in contact with the SBF. On the other hand, the morphology of apatite formation depended drastically on the pH of the SBF solution (Kobayashi, Ono, Hirakura, Oaki, & Imai, 2012). Therefore, the difference in obtained morphologies between pure CS and GNP/CS composites is likely due to different pH values. This finding indicates that the incorporation of GNP in CS decreased the pH value in SBF, suggesting a potential preferable material for *in vitro* bone cell culture. These results also showed that GNP/CS ceramics sintered by HIP possessed good bioactivity and could develop a bone-like HA layer on their surface when soaked in SBF.

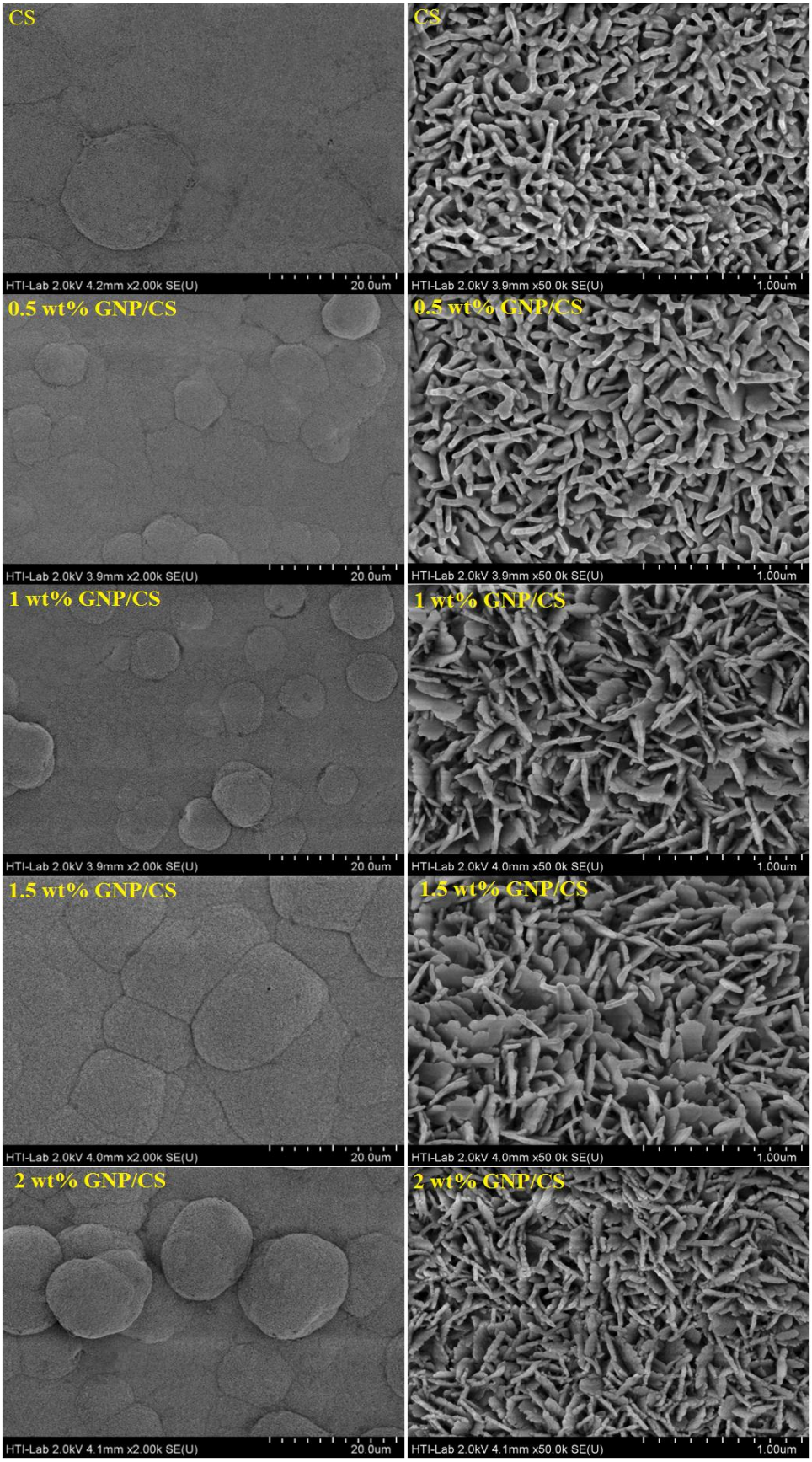

Figure 4.34: Low and high magnification FESEM images of apatite formation on pure CS and CS/GNP composites after soaking in the SBF for 14 days.

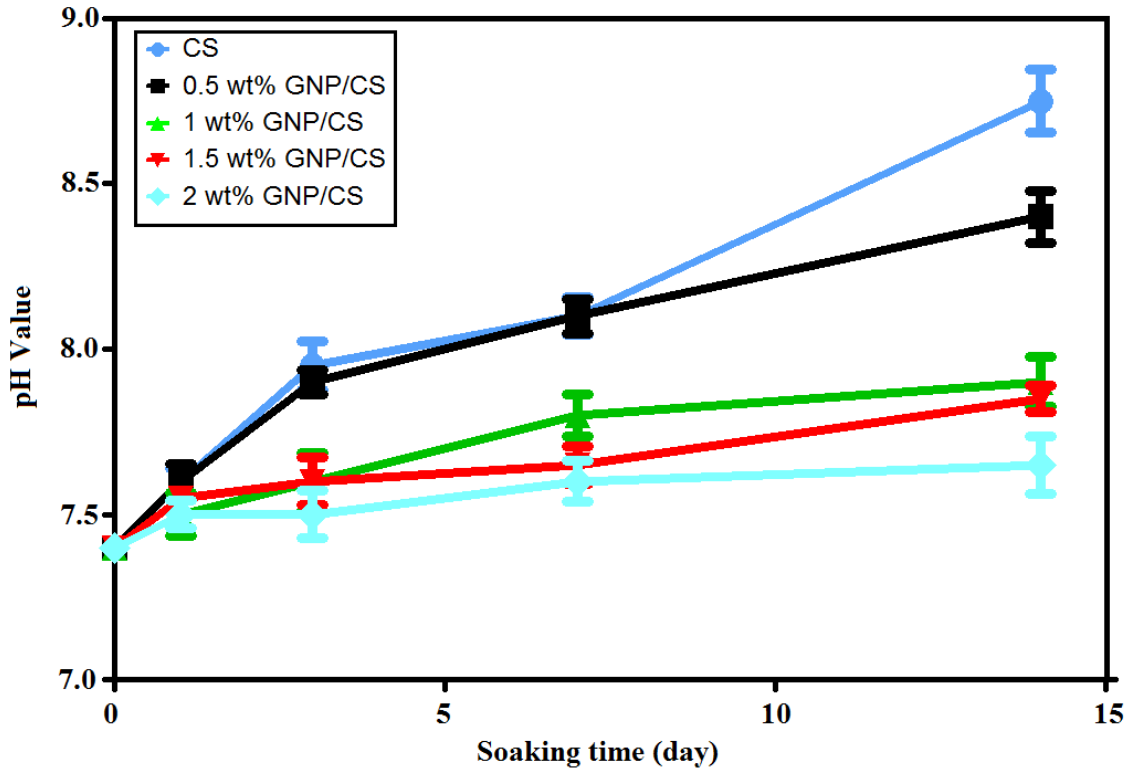

Figure 4.35: The change of pH value in SBF solution after soaking for various time periods.

4.4.5 Osteocompatibility characterization of CS/GNP composites by *in vitro* osteoblast culture

An orthopedic implant is expected to promote cellular adhesion, proliferation, and differentiation. Once the osteoblasts cover the implant surface by proliferation and growth, they deposit collagen in the intercellular region, known as osteoids. Moreover, osteoblasts collect salt ions from the blood to release them on the osteoid matrix for mineralization and bone formation (Bruinink et al., 2014; Lahiri, Benaduce, et al., 2011). This plays an essential role in osseointegration to determine the life-time of the implants (Lahiri, Ghosh, et al., 2012). Figure 4.36 shows the cellular morphology of human fetal osteoblastic cell line (hFOB) cells grown on pure CS and CS/GNP composites matrices after 1 day of culture. The cells adhered and spread on the pure CS

ceramic surface by means of thin cytoplasmic digitations as illustrated by the flattened morphology, and presented a close contact with the ceramic surface.

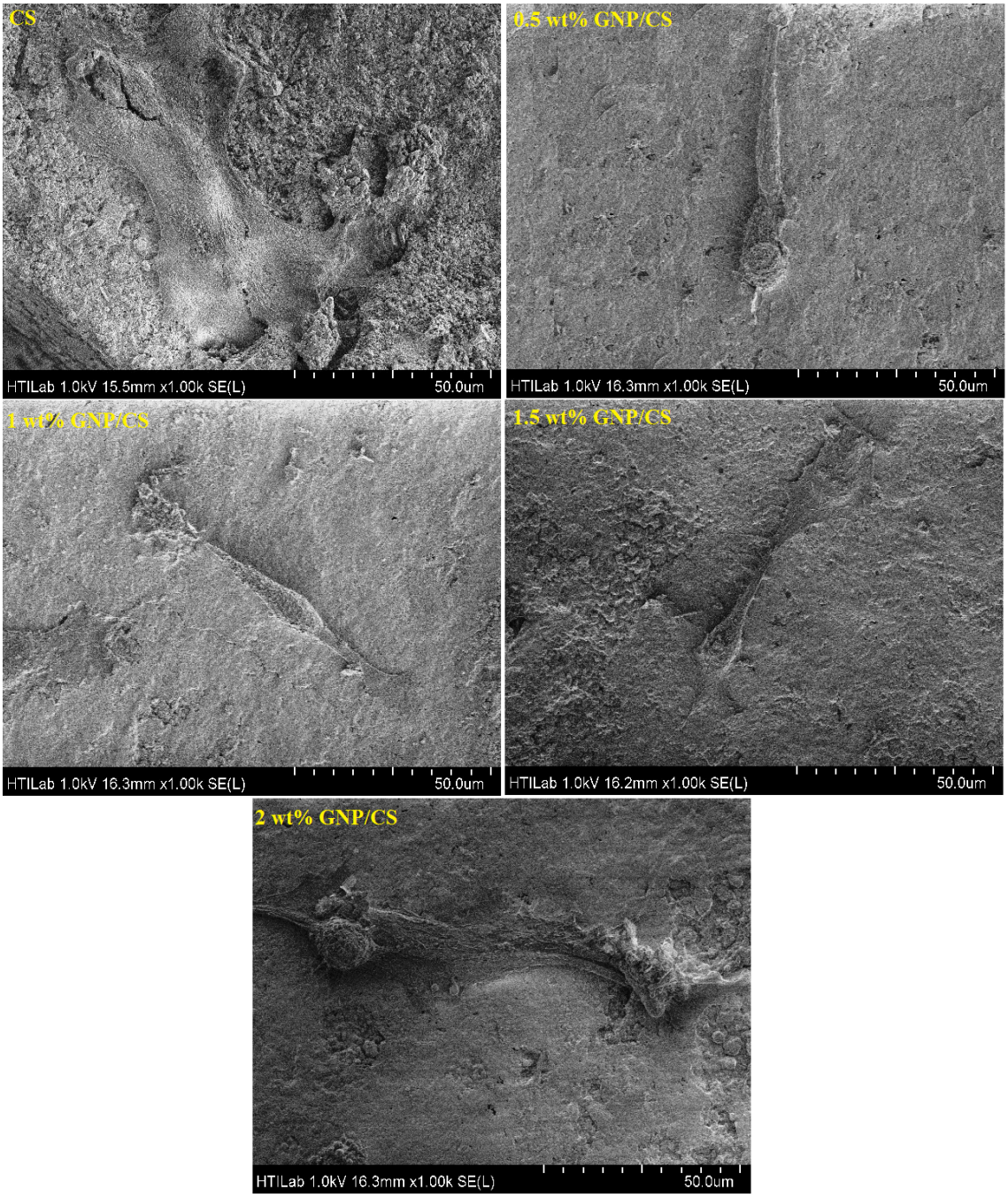

Figure 4.36: FESEM observations on cell morphology of hFOB osteoblasts cultured on pure CS and different CS/GNP composites after 24 hours. The scale bar in all the images is 50 μm.

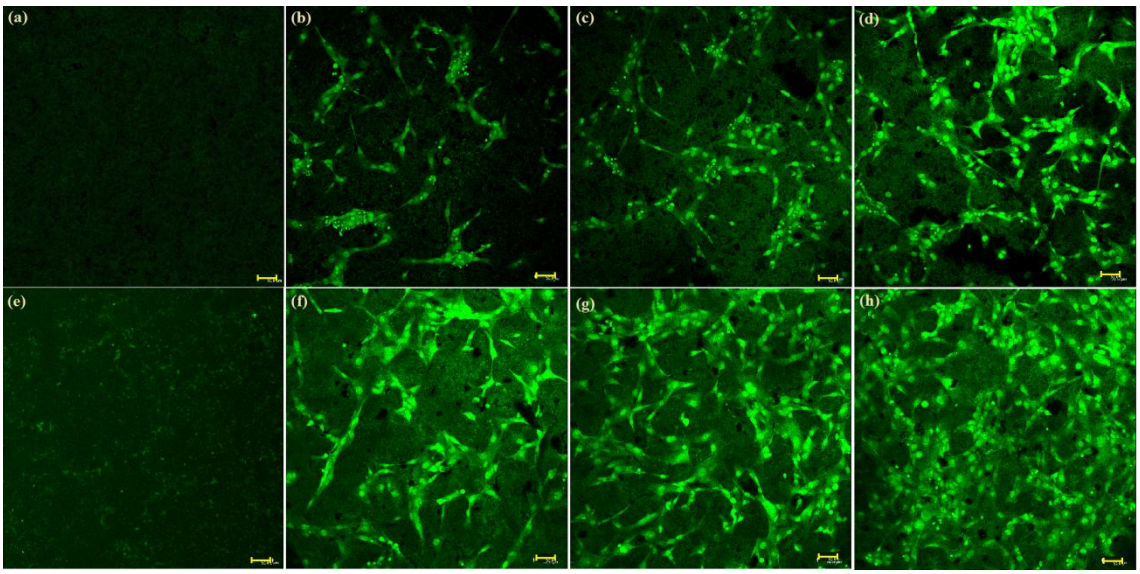

Figure 4.37: Comparison of the cell adhesion and proliferation on pure CS and CS/1 wt. % GNP composite surfaces at different time points: (a) blank of pure CS, (b-d) 1, 3 and 5 days on pure CS discs, (e) blank of CS/1 wt. % GNP, (f-h) 1, 3 and 5 days on CS/1 wt. % GNP composite. The scale bar represents 50 µm.

Fibroblast-like shape and filopodia of the cells are observed on CS/GNP composites. Since an increased number of filopodia enables the cells to tightly bind to CS/GNP surface; this composite is therefore considered more favorable to cellular integration than pure CS. Figure 4.37 presents confocal laser scanning microscopy (CLSM) images of hFOB cells cultured on the surface of pure CS and CS/1.0 wt. % GNP pellets. The osteoblast population clearly increases from 1 to 5 days on both surfaces. This observation indicates that CS and CS/GNP surfaces are suitable for osteoblast cell proliferation. Interestingly, the osteoblast population was visibly larger on CS/GNP surface than on pure CS after 3 and 5 days of culture as shown in Figure 4.37.

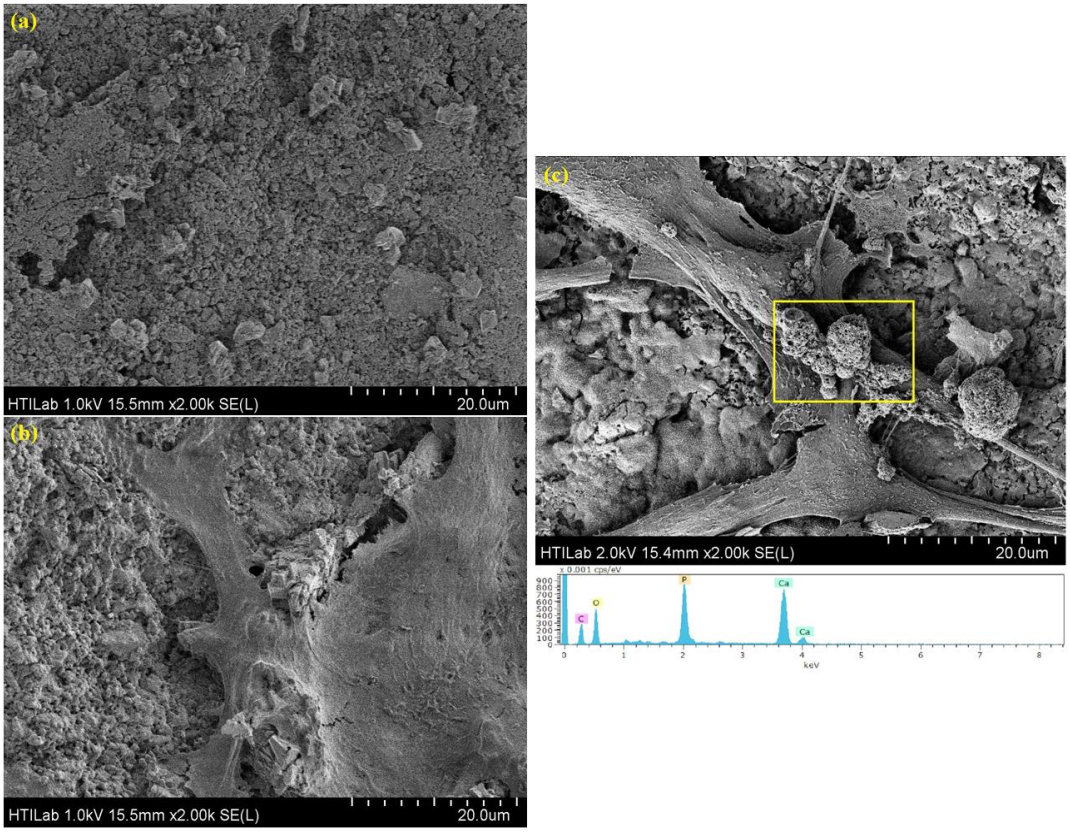

Figure 4.38: (a) CS/1 wt. % GNP composite without cells, (b) Pure CS with hFOB cells, (c) FESEM micrographs and the EDS spectrum of the hFOB cells, indicating a significant presence of P and CS on the CS/1 wt. % GNP composite following 3 days of seeding.

Merging of the cells promoted the formation of a rich ECM, showing high cell activity in the GNP/CS composites. The apatite formation on the ECM is important for mineralization and the generation of bone, as bone is formed by the mineralization of an organic matrix (largely collagen), through the nucleation and growth of a mineral closely similar to HA (Pan et al., 2010). As shown in Figure 4.38c, the mineral deposits present vivid apatite-like morphology and comprise fused globular aggregates of the minerals; and those granular minerals were illustrated in varying sizes on the CS/1 wt. % GNP composite. While, as indicated in Figure 4.38a and b, apatite like granules were not observed on the cell surface of pure CS and blank control surface of pure CS without hFOB cells after 3 day of cell culture. It is known that mineralization refers to

cell-mediated deposition of extracellular calcium and phosphorus salts where anionic matrix molecules take up the Ca^{2+}, phosphate ions and serve as nucleation and growth sites leading to calcification (Boskey, 1998). Hence, the incorporation of GNP into CS is expected to have higher negative charge than pure CS in culture medium and leads to more rapid mineral deposition on the surface of osteoblasts. In addition, the EDS pattern of hFOB cells on the CS/1 wt. % GNP composite indicated some presence of calcium and phosphate after 3 days of seeding.

It is also of interest to note that the Ca/P molar ratio of the mineral deposit on the cells was 1.65, which is approximately equal to that of HA (1.67), suggesting that the apatite formed in the ECM primarily consisted of HA, which is also the major inorganic component of bone. On the other hand, since osteoblast cells are entirely responsible for creating bone tissue by producing osteoid (composed mainly of Type I collagen) before commencing the mineralization of the osteoid matrix , this observation would propose a clear relevance to the mechanism of collagen-based apatite mineral formation (Y. Z. Zhang et al., 2008). These results provide the first evidence of growth of the osteoblasts on CS/GNP composites and corroborated those quantitative results obtained shown in Figure 4.39.

The cytotoxicity effects and cell proliferation of osteoblast cells on the various samples are shown in Figure 4.39 for comparison. There was no cytotoxicity of CS/GNP composites found in the hFOB cell line through the MTT assay. The cell proliferation of hFOB cells on each sample increased with the extension of culture time. The highest amount of cells could be observed on the CS/1 wt.% GNP composite. Many reports (X. Y. Liu et al., 2004; C. T. Wu et al., 2007; Xue, Liu, Zheng, & Ding, 2005; S. J. Zhao et al., 2008) have already shown that ionic dissolution products from CS are key factors in the metabolism, proliferation, cell–cell and matrix-cell adhesion of osteoblasts. Shen *et al.* (Y. H. Shen et al., 2011) found that the pH value of strontium-

containing CS is a critical factor for the proliferation and alkaline phosphatase (ALP) activity of osteoblasts. These results indicated a decrease in the pH of SBF due to increased GNP content in the CS ceramic, which can be desirable for cell growth. Furthermore, smaller grain size generally results in a higher specific surface area of the sample, which ultimately increases dissolution of calcium ions, and therefore it can be promoted better osteoblast interactions (Bose, Dasgupta, Tarafder, & Bandyopadhyay, 2010; Dasgupta, Tarafder, Bandyopadhyay, & Bose, 2013; Lv Zhang et al., 2013).

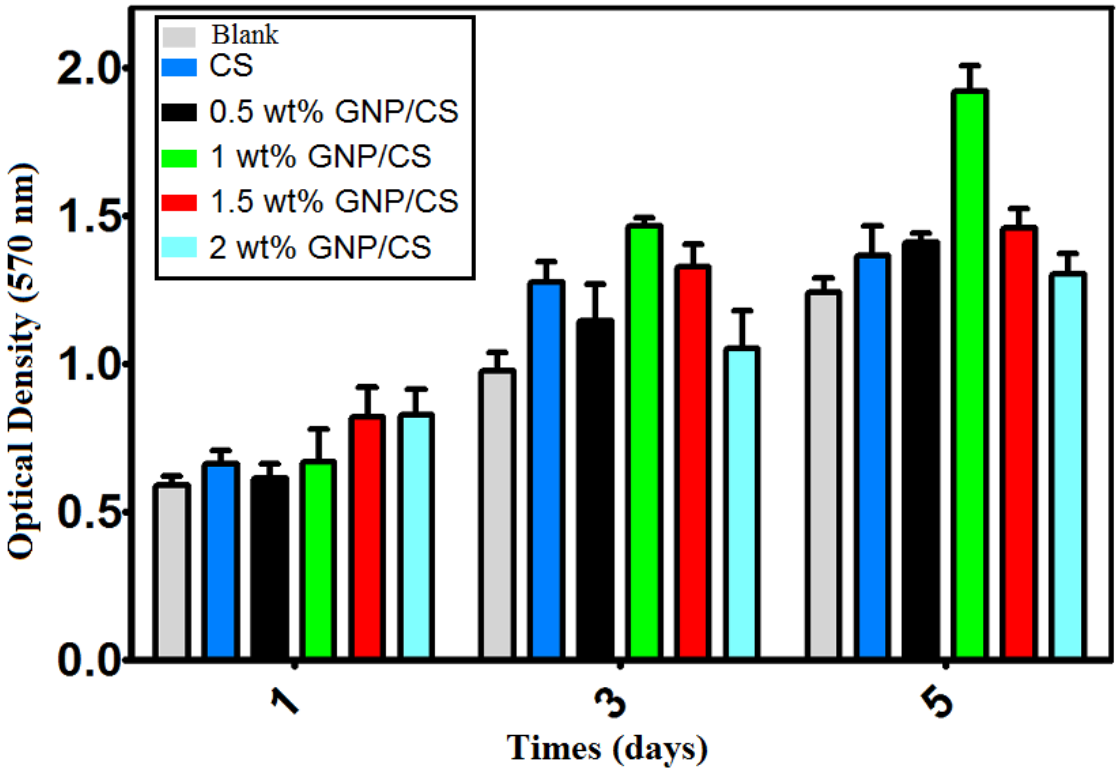

Figure 4.39: Proliferation of hFOB osteoblasts on different GNP/CS composites in comparison with pure CS and blank assessed using MTT assay ($P < 0.05, n = 5$).

The MTT result after 1,3 and 5 days shows that, the number of cells on CS/1 wt.% GNP composite with finer grain size was significantly higher than that on pure CS and 0.5, 1.5 and 2 Wt. % GNP. On the other hand, researchers have studied the effect of concentration of graphene on cell viability as well as cell cytotoxicity. They have concluded that cell viability can be affected by the concentration of graphene (Akhavan,

Ghaderi, & Akhavan, 2012; Gurunathan, Han, Eppakayala, & Kim, 2013). Previous studies have also indicated that graphene incorporation into hydroxyapatite stimulated osteoblast proliferation (Ming Li et al., 2014; Y. Liu, Dang, Wang, Huang, & Li, 2014), and that cytotoxicity of graphene to osteoblast is concentration-dependent with lowering the concentration of the graphene fillers resulting in improved biocompatibility to bone cells (Lahiri, Dua, et al., 2012; Siddique et al., 2013; X. Zhang et al., 2013). The present results show that GNP incorporation into CS has a positive effect on the proliferation of hFOB cells, while the degree of proliferation is related to the different GNP contenets in the CS ceramics. These results are a good indication that the CS/GNP composites are suitable to support the biocompatibility in terms of cell proliferation. However, it should be noted that the *in vitro* results we report here are very preliminary and further comprehensive understanding about the biocompatibility of the novel CS/GNP composites is required. Particularly, implantation in bone tissue and for longer period is required for absolute assessment of *in-vivo* biocompatibility, in order to establish the feasibility of employing CS/GNP in orthopedic implants and other tissue engineering applications.

4.5 Comparison of CS/rGO and CS/GNP composites

In this research project, graphene was proposed as reinforcement of CS for orthopaedic application. Due to the concerns related to cytotoxicity of rGO, GNP has been proposed as an alternative. The research plan thus includes processing of both CS/rGO and CS/GNP composites, their characterization for mechanical and evaluation of biocompatibility. However, two different synthesis methods were used to reinforce the CS matrix with graphene. The trends for both composite types are similar, with a steady increment in toughness with filler content up to 1 wt.%, and then decreasing for higher filler weight percentage. The toughening mechanisms were similar for all composites such as crack bridging, sheet pull-out, crack branching and crack deflection.

But, the fracture toughness of rGO composites is higher than that of GNP composites which may be due to the lower degree of exfoliation and weak interactions between the platelets and the CS matrix. The hardness of both composites increased with the graphene content up to 1 wt.% and then decreased due to porosity and agglomeration of graphene. Moreover, this trend also occurred for elastic modulus and brittleness index for both composites. Both rGO and GNP do not negatively influence the apatite forming ability and the viability of osteoblast on CS based surfaces. However, it is notable that the degree of proliferation was related to different GNP contents in the CS ceramics while this observation is not made for rGO. It should be noted that the *in vitro* results that reported here are very preliminary and further comprehensive understanding about the biocompatibility of the novel CS/rGO and CS/GNP composites is required. Particularly, implantation in bone tissue and for longer period is required for absolute assessment of *in-vivo* biocompatibility, in order to establish the feasibility of employing graphene/CS in orthopedic implants and other tissue engineering applications.

4.6 Summary

In this study, Calcium silicate hydrate (CSH) consisting of nanosheets has been successfully synthesized assisted by a tip ultrasonic irradiation (UI) method using calcium nitrate (Ca (NO_3).4H_2O), sodium silicate ($Na_2SiO_3 \cdot 9H_2O$) and sodium dodecyl sulfate (SDS) in water. Systematic studies found that reaction time of ultrasonic irradiation and concentrations of surfactant (SDS) in the system were important factors to control the crystallite size and morphologies. The results indicate that the optimum crystallite size is about 13 nm after 10 minutes of sonication time with 0.2 g SDS in mixed solvent and demonstrates bundles of nanosheets morphology with an average diameter and nanosheets length 300- 500 nm and 2-3 µm, respectively.

In the next part of this research work, a hydrothermal processing method were used to synthesize calcium silicate hydrate (xonotlite phase)-reduced graphene oxide

composite powders. This method produced CSH nanowires in the xonotlite phase with approximate diameters of 10-30 nm and lengths up to several micrometers that nucleate on and grow along graphene sheets. After densification at 1150 °C by HIP, the results indicated that the CS-1.0 wt. % rGO composite displays improved hardness, elastic modulus and fracture toughness compared to pure CS. The main toughening mechanisms are crack deflection, crack branching, crack bridging and graphene sheet pullout on the fracture surface. Moreover, the addition of rGO did not affect the ability to form apatite on CS ceramics. Interestingly, the introduction of rGO into the CS matrix stimulated hFOB proliferation and significantly increased the ALP activity of hFOB cells compared with pure CS ceramics in 7-day experiments.

GNS-reinforced calcium silicate composites have been fabricated by HIP and the influence of the different amounts of GNP (0.5, 1, 1.5 and 2 wt.%) on the microstructure development and mechanical properties were investigated. The incorporation of GNP into CS has a significant effect on grain size. Grain size is reduced in 0.5 and 1 wt.% GNP as GNP might tend to wrap around grains and inhibit grain growth. Compared to pure CS, the 1 wt.% GNP/CS composite displayed an increased hardness and ~130% and ~40% improvement in fracture toughness and brittleness index. The SBF soaking results revealed that the CS/GNP composites have apatite-forming ability. These results indicate that the incorporation of 1 wt.% GNP into CS stimulated hFOB cells, compared to cell seeding onto pure CS ceramics. The results in this study demonstrate promising *in vitro* cell compatibility and bioactivity of CS/GNP biocomposites. However, it must be noted that the degree of proliferation was related to the different GNP content in the CS ceramics.

CHAPTER 5

CONCLUSION

5.1 Conclusion

In this research, CSH and CS were fabricated and used to develop new composite materials for load bearing conditions. The CSH and CS particles were synthesized by the precipitation, hydrothermal and ultrasonic irradiation method.

Composite technology was applied to enhance the mechanical properties of CS ceramics and CS/rGO and CS/GNP composites were produced. Investigations on free standing CS-graphene composite reveal significant improvement in the fracture toughness with graphene reinforcement. The following conclusions may be drawn from the study:

(1) The synthesis of calcium silicate hydrate with appropriate quality and different morphologies is successfully performed via ultrasonic irradiation method. The following conclusions are drawn : (i) The output data from XRD and FESEM indicated that needle like morphology with average crystallite size of 9 nm have been successfully obtained by using calcium nitrate ($Ca(NO_3)\cdot 4H_2O$) and sodium silicate ($Na_2SiO_3\cdot 9H_2O$) in distilled water via UI. Moreover, the reaction time has a significant effect on the size and morphology of CSH. (ii) The results show that the SDS anionic surfactant has a significant effect on the assembly of CSH with the assistance of ultrasonication. SDS molecules can help the formation and stabilization of CSH bundles into nanosheets because of the charge and stereochemistry matching. (iii) The results indicate that the optimum crystallite size is about 13 nm after 10 minutes of sonication time with 0.2 g SDS in mixed solvent and demonstrates bundles of nanosheets morphology with an average diameter and nanosheets length 300- 500 nm and 2-3 μm, respectively. (iv) The results confirm that this CSH production method is

simple, reduces the preparation time, and low-cost with a range of different morphologies and size.

(2) Hydrothermal processing method was used to synthesize calcium silicate hydrate (xonotlite phase)-reduced graphene oxide composite powders. This method produced CS nanowires in the xonotlite phase with approximate diameters of 10-30 nm and lengths up to several micrometers that nucleate on and grow along the graphene sheets. After densification at 1150 °C by HIP, the samples obtained direct evidence of rGO in the composites using Raman spectroscopy, FTIR and FESEM. Most interestingly, the CS-1.0 wt. % rGO composite displays improved hardness, elastic modulus and fracture toughness compared to pure CS. The main toughening mechanisms are crack deflection, crack branching, crack bridging and graphene sheet pullout on the fracture surface. Moreover, the addition of rGO did not negatively affect the ability to form apatite on CS ceramics. Interestingly, the introduction of rGO into the CS matrix stimulated hFOB proliferation and significantly increased the ALP activity of hFOB cells compared with pure CS ceramics in 7-day experiments.

(3) GNS-reinforced calcium silicate composites have been fabricated by HIP and the influence of the different amounts of GNP (0.5, 1, 1.5 and 2 wt.%) on the microstructure development and mechanical properties were investigated. The incorporation of GNP into CS has a significant effect on grain size. Grain size is reduced in 0.5 and 1 wt.% GNP as GNP might tend to wrap around grains and inhibit grain growth. Compared to pure CS, the 1 wt.% GNP/CS composite displayed an increased hardness and ~130% and ~40% improvement in fracture toughness and brittleness index. Crack bridging, pull-out GNP, crack branching and crack deflection have been observed and are believed to be the causes of increased toughness. The SBF soaking results revealed that the CS/GNP composites have apatite-forming ability. These results indicate that the incorporation of 1 wt.% GNP into CS stimulated hFOB

cells, as opposed to cell seeding onto pure CS ceramics. However, it must be noted that the degree of proliferation was related to different GNP-containing CS ceramics.

5.2 Recommendations for future research

The aim of the current research was to explore the improvement of CS for orthopaedic application. The criteria for judgment were the effect of graphene reinforcement on mechanical and biological behaviour of the CS matrix. The findings of this study establish CS-graphene composites to be a potential alternative for clinically used CS. Nevertheless, some of the topics need further investigations to progress towards the clinical translation of CS-graphene. Following are recommendations for advancing the research towards the final accomplishment.

(1) The present research is the first report on CS-graphene composite. A parametric study is required to optimize the HIP parameters for consolidation of CS-graphene composite with varying graphene concentration, to achieve the optimum mechanical properties. Moreover, the spark plasma sintering (SPS) method is recommended over other methods for sintering CS-graphene composites due to prepare fully densified composites at lower temperatures and substantially shorter holding times.

(2) The apatite-forming ability test results show that the fabricated CS-graphene composites can be bioactive materials. The degradation and bonding process of CS composite implant with neighbouring natural bone are required to be studied through *in-vivo* experiments in which samples are implanted in animal hard tissues for longer exposure periods (3 months, 6 months and 1 year) followed by histocompatibility studies. The rehabilitation process of bone defects rehabilitated by CS composite implants can be further investigated. Additionally, the mechanical properties of implants after implantation for different periods should be tested to ensure that the

mechanical properties of implants are high enough to sustain general load during the whole rehabilitation process.

(3) The *in-vitro* results reported here are very preliminary and further comprehensive understanding about the biocompatibility of the novel CS-graphene composites is required. Particularly, implantation in bone tissue and for longer period is required for absolute assessment of in-vivo biocompatibility, in order to establish the feasibility of employing CS-graphene in orthopedic implants and other tissue engineering applications.

REFERENCES

Agarwal, S., Zhou, X. Z., Ye, F., He, Q. Y., Chen, G. C. K., Soo, J., . . . Chen, P. (2010). Interfacing Live Cells with Nanocarbon Substrates. *Langmuir, 26*(4), 2244-2247.

Akhavan, O., Choobtashani, M., & Ghaderi, E. (2012). Protein Degradation and RNA Efflux of Viruses Photocatalyzed by Graphene-Tungsten Oxide Composite Under Visible Light Irradiation. *Journal of Physical Chemistry C, 116*(17), 9653-9659.

Akhavan, O., & Ghaderi, E. (2010). Toxicity of Graphene and Graphene Oxide Nanowalls Against Bacteria. *ACS Nano, 4*(10), 5731-5736.

Akhavan, O., Ghaderi, E., & Akhavan, A. (2012). Size-dependent genotoxicity of graphene nanoplatelets in human stem cells. *Biomaterials, 33*(32), 8017-8025.

Akhavan, O., Ghaderi, E., & Rahighi, R. (2012). Toward Single-DNA Electrochemical Biosensing by Graphene Nanowalls. *ACS Nano, 6*(4), 2904-2916.

Amada, S., Munekata, T., Nagase, Y., Ichikawa, Y., Kirigai, A., & Yang, Z. F. (1996). The mechanical structures of bamboos in viewpoint of functionally gradient and composite materials. *Journal of Composite Materials, 30*(7), 800-819.

Anstis, G. R., Chantikul, P., Lawn, B. R., & Marshall, D. B. (1981). A critical evaluation of indentation techniques for measuring fracture toughness: I, direct crack measurements. *Journal of the American Ceramic Society, 64*(9), 533-538.

Baciu, D., & Simitzis, J. (2007). Synthesis and characterization of a calcium silicate bioactive glass. *Journal of Optoelectronics and Advanced Materials, 9*(11), 3320-3324.

Baradaran, S., Basirun, W. J., Mahmoudian, M. R., Hamdi, M., & Alias, Y. (2013). Synthesis and Characterization of Monetite Prepared Using a Sonochemical Method in a Mixed Solvent System of Water/Ethylene Glycol/N,N-Dimethylformamide. *Metallurgical And Materials Transactions A-Physical Metallurgy And Materials Science*, 1-8.

Baradaran, S., Moghaddam, E., Basirun, W. J., Mehrali, M., Sookhakian, M., Hamdi, M., . . . Alias, Y. (2014). Mechanical properties and biomedical applications of a nanotube hydroxyapatite-reduced graphene oxide composite. *Carbon, 69*(0), 32-45.

Barralet, J. E., Best, S. M., & Bonfield, W. (2000). Effect of sintering parameters on the density and microstructure of carbonate hydroxyapatite. *Journal of Materials Science-Materials in Medicine, 11*(11), 719-724.

Basavaraja, C., Noh, G. T., & Huh, D. S. (2013). Chemically modified polyaniline nanocomposites by poly(2-acrylamido-2-methyl-1-propanesulfonicacid)/graphene nanoplatelet. *Colloid and Polymer Science, 291*(12), 2755-2763.

Bauer, T. W., Geesink, R. C. T., Zimmerman, R., & McMahon, J. T. (1991). Hydroxyapatite-coated femoral stems. Histological analysis of components retrieved at autopsy. *Journal of Bone and Joint Surgery-American Volume, 73A*(10), 1439-1452.

Beheri, H. H., Mohamed, K. R., & El-Bassyouni, G. T. (2013). Mechanical and microstructure of reinforced hydroxyapatite/calcium silicate nano-composites materials. *Materials & Design, 44*, 461-468.

Best, S. M., Porter, A. E., Thian, E. S., & Huang, J. (2008). Bioceramics: Past, present and for the future. *Journal of the European Ceramic Society, 28*(7), 1319-1327.

Björnström, J., Martinelli, A., Matic, A., Börjesson, L., & Panas, I. (2004). Accelerating effects of colloidal nano-silica for beneficial calcium–silicate–hydrate formation in cement. *Chem. Phys. Lett., 392*(1–3), 242-248.

Bocanegra-Bernal, M. H. (2004). Hot Isostatic Pressing (HIP) technology and its applications to metals and ceramics. *Journal of Materials Science, 39*(21), 6399-6420.

Boccaccini, A. R. (1997). Machinability and brittleness of glass-ceramics. *Journal Of Materials Processing Technology, 65*(1-3), 302-304.

Bonaccorsi, E., Merlino, S., & Taylor, H. F. W. (2004). The crystal structure of jennite, Ca9Si6O18(OH)(6)center dot 8H(2)O. *Cement and Concrete Research, 34*(9), 1481-1488.

Bonfield, W., Grynpas, M. D., Tully, A. E., Bowman, J., & Abram, J. (1981). Hydroxyapatite reinforced polyethylene-a mechanically compatible implant material for bone replacement. *Biomaterials, 2*(3), 185-186.

Bose, Susmita, Dasgupta, Sudip, Tarafder, Solaiman, & Bandyopadhyay, Amit. (2010). Microwave-processed nanocrystalline hydroxyapatite: Simultaneous enhancement of mechanical and biological properties. *Acta Biomaterialia, 6*(9), 3782-3790.

Boskey, A. L. (1998). Biomineralization: Conflicts, challenges, and opportunities. *Journal of Cellular Biochemistry*, 83-91.

Bruinink, Arie, Bitar, Malak, Pleskova, Miriam, Wick, Peter, Krug, Harald F., & Maniura-Weber, Katharina. (2014). Addition of nanoscaledbioinspiredsurface features: A revolution for bone related implants and scaffolds? *Journal of Biomedical Materials Research Part A, 102*(1), 275-294.

Burzo, E. (2006). Xonotlite group of silicates (Text). In H. P. J. Wijn (Ed.), *Inosilicates* (Vol. 27I4, pp. 371-378): Springer Berlin Heidelberg.

Carty, William M., & Senapati, Udayan. (1998). Porcelain—Raw Materials, Processing, Phase Evolution, and Mechanical Behavior. *Journal of the American Ceramic Society, 81*(1), 3-20.

Castelain, M., Martinez, G., Marco, C., Ellis, G., & Salavagione, H. J. (2013). Effect of Click-Chemistry Approaches for Graphene Modification on the Electrical, Thermal, and Mechanical Properties of Polyethylene/Graphene Nanocomposites. *Macromolecules, 46*(22), 8980-8987.

Castillo-Rodríguez, M., Muñoz, A., & Domínguez-Rodríguez, A. (2006). Effect of atmosphere and sintering time on the microstructure and mechanical properties at high temperatures of α-SiC sintered with liquid phase Y2O3–Al2O3. *Journal of the European Ceramic Society, 26*(12), 2397-2405.

Chen, G. Y., Pang, D. W. P., Hwang, S. M., Tuan, H. Y., & Hu, Y. C. (2012). A graphene-based platform for induced pluripotent stem cells culture and differentiation. *Biomaterials, 33*(2), 418-427.

Chen, Jeffrey J., Thomas, Jeffrey J., Taylor, Hal F. W., & Jennings, Hamlin M. (2004). Solubility and structure of calcium silicate hydrate. *Cement and Concrete Research, 34*(9), 1499-1519.

Cheng, K., Zhang, S., Weng, W. J., Khor, K. A., Miao, S. D., & Wang, Y. S. (2008). The adhesion strength and residual stress of colloidal-sol gel derived beta-tricalcium-phosphate/fluoridated-hydroxyapatite biphasic coatings. *Thin Solid Films, 516*(10), 3251-3255.

Colomban, P. (2004). Raman spectrometry, a unique tool to analyze and classify ancient ceramics and glasses. *Applied Physics A-Materials Science & Processing 79*(2), 167-170.

Das, S., Singh, S., Singh, V., Joung, D., Dowding, J. M., Reid, D., . . . Seal, S. (2013). Oxygenated Functional Group Density on Graphene Oxide: Its Effect on Cell Toxicity. *Particle & Particle Systems Characterization, 30*(2), 148-157.

Dasgupta, Sudip, Tarafder, Solaiman, Bandyopadhyay, Amit, & Bose, Susmita. (2013). Effect of grain size on mechanical, surface and biological properties of microwave sintered hydroxyapatite. *Materials Science and Engineering: C, 33*(5), 2846-2854.

De Aza, P. N., Luklinska, Z. B., Anseau, M. R., Guitian, F., & De Aza, S. (1999). Bioactivity of pseudowollastonite in human saliva. *Journal of Dentistry, 27*(2), 107-113.

de Castro, M. D. L., & Priego-Capote, F. (2007). Ultrasound-assisted crystallization (sonocrystallization). *Ultrasonics Sonochemistry, 14*(6), 717-724.

Delgado, Ana H., Paroli, R. M., & Beaudoin, J. J. (1996). Comparison of IR techniques for the characterization of construction cement minerals and hydrated products. *Applied Spectroscopy, 50*(8), 970-976.

Delsanti, M., Moussaid, A., & Munch, J. P. (1993). Effect Of Electric Charges On The Growth-Process Of Micelles. *Journal of Colloid and Interface Science, 157*(2), 285-290.

Dinan, B., Gallego-Perez, D., Lee, H., Hansford, D., & Akbar, S. A. (2013). Thermally grown TiO2 nanowires to improve cell growth and proliferation on titanium based materials. *Ceramics International, 39*(5), 5949-5954.

Driessens, F. C. M. (1980). The mineral in bone, dentin and tooth enamel *Bulletin Des Societes Chimiques Belges, 89*(8), 663-689.

Dusza, J., Morgiel, J., Duszova, A., Kvetkova, L., Nosko, M., Kun, P., & Balazsi, C. (2012). Microstructure and fracture toughness of Si3N4 + graphene platelet composites. *Journal of the European Ceramic Society, 32*(12), 3389-3397.

Dusza, Ján, Morgiel, Jerzy, Duszová, Annamária, Kvetková, Lenka, Nosko, Martin, Kun, Péter, & Balázsi, Csaba. (2012). Microstructure and fracture toughness of

Si3N4 + graphene platelet composites. *Journal of the European Ceramic Society, 32*(12), 3389-3397.

Echeberria, J., Tarazona, J., He, J. Y., Butler, T., & Castro, F. (2002). Sinter-HIP of α-alumina powders with sub-micron grain sizes. *Journal of the European Ceramic Society, 22*(11), 1801-1809.

Elliott, J. C., & Young, R. A. (1967). Conversion of single crystals of chlorapatite into single crystals of hydroxyapatite [6]. *Nature, 214*(5091), 904-906.

Fan, H. L., Wang, L. L., Zhao, K. K., Li, N., Shi, Z. J., Ge, Z. G., & Jin, Z. X. (2010). Fabrication, Mechanical Properties, and Biocompatibility of Graphene-Reinforced Chitosan Composites. *Biomacromolecules, 11*(9), 2345-2351.

Fan, Yuchi, Wang, Lianjun, Li, Jianlin, Li, Jiaqi, Sun, Shikuan, Chen, Feng, . . . Jiang, Wan. (2010). Preparation and electrical properties of graphene nanosheet/Al2O3 composites. *Carbon, 48*(6), 1743-1749.

Fan, Z. J., Wang, J. Q., Wang, Z. F., Ran, H. Q., Li, Y., Niu, L. Y., . . . Yang, S. R. (2014). One-pot synthesis of graphene/hydroxyapatite nanorod composite for tissue engineering. *Carbon, 66*, 407-416.

Ferrari, A. C., & Basko, D. M. (2013). Raman spectroscopy as a versatile tool for studying the properties of graphene. *Nature Nanotechnology, 8*(4), 235-246.

Gandolfi, M. G., Ciapetti, G., Taddei, P., Perut, F., Tinti, A., Cardoso, M. V., . . . Prati, C. (2010). Apatite formation on bioactive calcium-silicate cements for dentistry affects surface topography and human marrow stromal cells proliferation. *Dental Materials, 26*(10), 974-992.

Garbev, K., Stemmermann, P., Black, L., Breen, C., Yarwood, J., & Gasharova, B. (2007). Structural features of C-S-H(I) and its carbonation in air - A Raman spectroscopic study. Part I: Fresh phases. *Journal of the American Ceramic Society, 90*(3), 900-907.

Gard, J. A., Mohan, K., Taylor, H. F. W., & Cliff, G. (1980). Analytical electron microscopy of cement pastes: I, Tricalcium silicate pastes. *Journal of the American Ceramic Society, 63*(5-6), 336-337.

Geim, A. K. (2009). Graphene: Status and Prospects. *Science, 324*(5934), 1530-1534.

Geim, A. K., & Novoselov, K. S. (2007). The rise of graphene. *Nature Materials, 6*(3), 183-191.

Gurunathan, Sangiliyandi, Han, Jae Woong, Eppakayala, Vasuki, & Kim, Jin-Hoi. (2013). Biocompatibility of microbially reduced graphene oxide in primary mouse embryonic fibroblast cells. *Colloids and Surfaces B: Biointerfaces, 105*(0), 58-66.

He, Q. Y., Sudibya, H. G., Yin, Z. Y., Wu, S. X., Li, H., Boey, F., . . . Zhang, H. (2010). Centimeter-Long and Large-Scale Micropatterns of Reduced Graphene Oxide Films: Fabrication and Sensing Applications. *ACS Nano, 4*(6), 3201-3208.

Hench, L. L. (1991). Bioceramics: from concept to clinic. *Journal of the American Ceramic Society, 74*(7), 1487-1510.

Henmi, C., Kawahara, A., Henmi, K., Kusachi, I., & Takeuchi, Y. (1983). The 3T, 4T and 5T polytypes of wollastonite from Kushiro, Hiroshima Prefecture, Japan. *American Mineralogist, 68*(1-2), 156-163.

Hoffmann, M. J., Geyer, A., & Oberacker, R. (1999). Potential of the Sinter-HIP-technique for the Development of High-temperature Resistant Si3N4-ceramics. *Journal of the European Ceramic Society, 19*(13–14), 2359-2366.

Hosseinkhani, Hossein, Hosseinkhani, Mohsen, Khademhosseini, Ali, & Kobayashi, Hisatoshi. (2007). Bone regeneration through controlled release of bone morphogenetic protein-2 from 3-D tissue engineered nano-scaffold. *Journal of Controlled Release, 117*(3), 380-386.

Hu, C. F., Liu, Y. L., Qin, J. L., Nie, G. T., Lei, B. F., Xiao, Y., . . . Rong, J. H. (2013). Fabrication of Reduced Graphene Oxide and Sliver Nanoparticle Hybrids for Raman Detection of Absorbed Folic Acid: A Potential Cancer Diagnostic Probe. *ACS Applied Materials & Interfaces, 5*(11), 4760-4768.

Hu, W. B., Peng, C., Luo, W. J., Lv, M., Li, X. M., Li, D., . . . Fan, C. H. (2010). Graphene-Based Antibacterial Paper. *ACS Nano, 4*(7), 4317-4323.

Hu, W., Peng, C., Luo, W., Lv, M., Li, X., Li, D., . . . Fan, C. (2010). Graphene-based antibacterial paper. *ACS Nano, 4*(7), 4317-4323.

Huang, N. M., Lim, H. N., Chia, C. H., Yarmo, M. A., & Muhamad, M. R. (2011). Simple room-temperature preparation of high-yield large-area graphene oxide. *International Journal of Nanomedicine, 6*, 3443-3448.

Hvizdoš, Pavol, Dusza, Ján, & Balázsi, Csaba. (2013). Tribological properties of Si3N4–graphene nanocomposites. *Journal of the European Ceramic Society, 33*(12), 2359-2364.

Ibanez, A., Pena, J. M. G., & Sandoval, F. (1990). Solid-state reaction for producing beta-wollastonite. *American Ceramic Society Bulletin, 69*(3), 374-&.

Jain, S. K., Awasthi, A. M., Jain, N. K., & Agrawal, G. P. (2005). Calcium silicate based microspheres of repaglinide for gastroretentive floating drug delivery: Preparation and in vitro characterization. *Journal of Controlled Release, 107*(2), 300-309.

Jain, S., Sharma, A., & Basu, B. (2013). In vitro cytocompatibility assessment of amorphous carbon structures using neuroblastoma and Schwann cells. *Journal of Biomedical Materials Research Part B-Applied Biomaterials, 101B*(4), 520-531.

Jevtic, M., Mitric, M., Skapin, S., Jancar, B., Ignjatovic, N., & Uskokovic, D. (2008). Crystal structure of hydroxyapatite nanorods synthesized by sonochemical homogeneous precipitation. *Crystal Growth & Design, 8*(7), 2217-2222.

Kalbacova, M., Broz, A., Kong, J., & Kalbac, M. (2010). Graphene substrates promote adherence of human osteoblasts and mesenchymal stromal cells. *Carbon, 48*(15), 4323-4329.

Kaur, Gurbinder, Pandey, O. P., Singh, K., Homa, Dan, Scott, Brian, & Pickrell, Gary. (2014). A review of bioactive glasses: Their structure, properties, fabrication and apatite formation. *Journal of Biomedical Materials Research Part A, 102*(1), 254-274.

Khorsand Zak, A., Abd. Majid, W. H., Abrishami, M. E., & Yousefi, Ramin. (2011). X-ray analysis of ZnO nanoparticles by Williamson–Hall and size–strain plot methods. *Solid State Sciences, 13*(1), 251-256.

Kim, Jung Min, Huh, Yun Suk, Han, Young-Kyu, Cho, Min Su, & Kim, Hae Jin. (2012). Facile synthesis route to highly crystalline mesoporous γ-MnO2 nanospheres. *Electrochemistry Communications, 14*(1), 32-35.

Kobayashi, T., Ono, S., Hirakura, S., Oaki, Y., & Imai, H. (2012). Morphological variation of hydroxyapatite grown in aqueous solution based on simulated body fluid. *Crystengcomm, 14*(3), 1143-1149.

Kokubo, T. (1990). Surface chemistry of bioactive glass-ceramics. *Journal of Non-Crystalline Solids, 120*(1-3), 138-151.

Kokubo, T. (1991). Bioactive glass ceramics: properties and applications. *Biomaterials, 12*(2), 155-163.

Kokubo, T., & Takadama, H. (2006). How useful is SBF in predicting in vivo bone bioactivity? *Biomaterials, 27*(15), 2907-2915.

Kothapalli, C., Wei, M., Vasiliev, A., & Shaw, M. T. (2004). Influence of temperature and concentration on the sintering behavior and mechanical properties of hydroxyapatite. *Acta Materialia, 52*(19), 5655-5663.

Kroll, A., Dierker, C., Rommel, C., Hahn, D., Wohlleben, W., Schulze-Isfort, C., . . . Schnekenburger, J. (2011). Cytotoxicity screening of 23 engineered nanomaterials using a test matrix of ten cell lines and three different assays. *Particle and Fibre Toxicology, 8*.

Kumar, Alok, Webster, Thomas J., Biswas, Krishanu, & Basu, Bikramjit. (2013). Flow cytometry analysis of human fetal osteoblast fate processes on spark plasma sintered hydroxyapatite–titanium biocomposites. *Journal of Biomedical Materials Research Part A, 101*(10), 2925-2938.

Kumar, R. V., Koltypin, Y., Palchik, O., & Gedanken, A. (2002). Preparation and characterization of nickel-polystyrene nanocomposite by ultrasound irradiation. *Journal of Applied Polymer Science, 86*(1), 160-165.

Kvetková, Lenka, Duszová, Annamária, Hvizdoš, Pavol, Dusza, Ján, Kun, Péter, & Balázsi, Csaba. (2012). Fracture toughness and toughening mechanisms in graphene platelet reinforced Si3N4 composites. *Scripta Materialia, 66*(10), 793-796.

Lahiri, D., Benaduce, A. P., Rouzaud, F., Solomon, J., Keshri, A. K., Kos, L., & Agarwal, A. (2011). Wear behavior and in vitro cytotoxicity of wear debris generated from hydroxyapatite-carbon nanotube composite coating. *Journal of Biomedical Materials Research Part A, 96A*(1), 1-12.

Lahiri, D., Dua, R., Zhang, C., de Socarraz-Novoa, I., Bhat, A., Ramaswamy, S., & Agarwal, A. (2012). Graphene Nanoplatelet-Induced Strengthening of UltraHigh Molecular Weight Polyethylene and Biocompatibility In vitro. *ACS Applied Materials & Interfaces, 4*(4), 2234-2241.

Lahiri, D., Ghosh, S., & Agarwal, A. (2012). Carbon nanotube reinforced hydroxyapatite composite for orthopedic application: A review. *Materials Science and Engineering C: Materials for Biological Applications, 32*(7), 1727-1758.

Lahiri, D., Singh, V., Benaduce, A. P., Seal, S., Kos, L., & Agarwal, A. (2011). Boron nitride nanotube reinforced hydroxyapatite composite: Mechanical and tribological performance and in-vitro biocompatibility to osteoblasts. *Journal of the Mechanical Behavior of Biomedical Materials, 4*(1), 44-56.

Li, M., Wang, Y., Liu, Q., Li, Q., Cheng, Y., Zheng, Y., . . . Wei, S. (2013). In situ synthesis and biocompatibility of nano hydroxyapatite on pristine and chitosan functionalized graphene oxide. *Journal of Materials Chemistry B, 1*(4), 475-484.

Li, Ming, Liu, Qian, Jia, Zhaojun, Xu, Xuchen, Cheng, Yan, Zheng, Yufeng, . . . Wei, Shicheng. (2014). Graphene oxide/hydroxyapatite composite coatings fabricated by electrophoretic nanotechnology for biological applications. *Carbon, 67*(0), 185-197.

Li, X. K., & Chang, J. (2006). A novel hydrothermal route to the synthesis of xonotlite nanofibers and investigation on their bioactivity. *Journal of Materials Science, 41*(15), 4944-4947.

Liao, K. H., Lin, Y. S., Macosko, C. W., & Haynes, C. L. (2011). Cytotoxicity of Graphene Oxide and Graphene in Human Erythrocytes and Skin Fibroblasts. *ACS Applied Materials & Interfaces, 3*(7), 2607-2615.

Lim, H. N., Huang, N. M., Lim, S. S., Harrison, I., & Chia, C. H. (2011). Fabrication and characterization of graphene hydrogel via hydrothermal approach as a scaffold for preliminary study of cell growth. *International Journal of Nanomedicine, 6*, 1817-1823.

Lin, K. L., Chang, J., Chen, G. F., Ruan, M. L., & Ning, C. Q. (2007). A simple method to synthesize single-crystalline beta-wollastonite nanowires. *Journal of Crystal Growth, 300*(2), 267-271.

Lin, K. L., Chang, J., & Cheng, R. M. (2007). In vitro hydroxyapatite forming ability and dissolution of tobermorite nanofibers. *Acta Biomaterialia, 3*(2), 271-276.

Lin, K. L., Chang, J., & Lu, J. X. (2006). Synthesis of wollastonite nanowires via hydrothermal microemulsion methods. *Materials Letters, 60*(24), 3007-3010.

Lin, K. L., Zhai, W. Y., Ni, S. Y., Chang, J., Zeng, Y., & Qian, W. J. (2005). Study of the mechanical property and in vitro biocompatibility of CaSiO3 ceramics. *Ceramics International, 31*(2), 323-326.

Lin, K. L., Zhang, M. L., Zhai, W. Y., Qu, H. Y., & Chang, J. A. (2011). Fabrication and Characterization of Hydroxyapatite/Wollastonite Composite Bioceramics with Controllable Properties for Hard Tissue Repair. *Journal of the American Ceramic Society, 94*(1), 206-212.

Liu, J., Yan, H. X., & Jiang, K. (2013). Mechanical properties of graphene platelet-reinforced alumina ceramic composites. *Ceramics International, 39*(6), 6215-6221.

Liu, J., Yan, H. X., Reece, M. J., & Jiang, K. (2012). Toughening of zirconia/alumina composites by the addition of graphene platelets. *Journal of the European Ceramic Society, 32*(16), 4185-4193.

Liu, Jian, Yan, Haixue, & Jiang, Kyle. (2013). Mechanical properties of graphene platelet-reinforced alumina ceramic composites. *Ceramics International, 39*(6), 6215-6221.

Liu, Jian, Yan, Haixue, Reece, Mike J., & Jiang, Kyle. (2012). Toughening of zirconia/alumina composites by the addition of graphene platelets. *Journal of the European Ceramic Society, 32*(16), 4185-4193.

Liu, X. Y., Ding, C. X., & Chu, P. K. (2004). Mechanism of apatite formation on wollastonite coatings in simulated body fluids. *Biomaterials, 25*(10), 1755-1761.

Liu, X. Y., Ding, C. X., & Wang, Z. Y. (2001). Apatite formed on the surface of plasma-sprayed wollastonite coating immersed in simulated body fluid. *Biomaterials, 22*(14), 2007-2012.

Liu, Xuanyong, Morra, Marco, Carpi, Angelo, & Li, Baoe. (2008). Bioactive calcium silicate ceramics and coatings. *Biomedicine & Pharmacotherapy, 62*(8), 526-529.

Liu, Yi, Dang, Zhaohui, Wang, Yuyue, Huang, Jing, & Li, Hua. (2014). Hydroxyapatite/graphene-nanosheet composite coatings deposited by vacuum cold spraying for biomedical applications: Inherited nanostructures and enhanced properties. *Carbon, 67*(0), 250-259.

Liu, Yi, Huang, Jing, & Li, Hua. (2013). Synthesis of hydroxyapatite-reduced graphite oxide nanocomposites for biomedical applications: oriented nucleation and epitaxial growth of hydroxyapatite. *Journal of Materials Chemistry B, 1*(13), 1826-1834.

Long, L. H., Chen, L. D., Bai, S. Q., Chang, J., & Lin, K. L. (2006). Preparation of dense beta-CaSiO3 ceramic with high mechanical strength and HAp formation ability in simulated body fluid. *Journal of the European Ceramic Society, 26*(9), 1701-1706.

Long, L. H., Zhang, F. M., Chen, L., Chen, L. D., & Chang, J. (2008). Preparation and properties of beta-CaSiO3/ZrO2 (3Y) nanocomposites. *Journal of the European Ceramic Society, 28*(15), 2883-2887.

Lu, B. Q., Zhu, Y. J., Ao, H. Y., Qi, C., & Chen, F. (2012). Synthesis and Characterization of Magnetic Iron Oxide/Calcium Silicate Mesoporous Nanocomposites as a Promising Vehicle for Drug Delivery. *ACS Applied Materials & Interfaces, 4*(12), 6968-6973.

Magallanes-Perdomo, M., De Aza, A. H., Mateus, A. Y., Teixeira, S., Monteiro, F. J., De Aza, S., & Pena, P. (2010). In vitro study of the proliferation and growth of human bone marrow cells on apatite-wollastonite-2M glass ceramics. *Acta Biomaterialia, 6*(6), 2254-2263.

Marlinda, A. R., Huang, N. M., Muhamad, M. R., An'amt, M. N., Chang, B. Y. S., Yusoff, N., . . . Kumar, S. V. (2012). Highly efficient preparation of ZnO nanorods decorated reduced graphene oxide nanocomposites. *Materials Letters, 80*, 9-12.

Mehrali, M., Latibari, S. T., Mehrali, M., Metselaar, H. S. C., & Silakhori, M. (2013). Shape-stabilized phase change materials with high thermal conductivity based on paraffin/graphene oxide composite. *Energy Conversion and Management, 67*, 275-282.

Mehrali, Mohammad, Latibari, Sara Tahan, Mehrali, Mehdi, Indra Mahlia, Teuku Meurah, & Cornelis Metselaar, Hendrik Simon. Preparation and properties of highly conductive palmitic acid/graphene oxide composites as thermal energy storage materials. *Energy*(0).

Mo, R. W., Lei, Z. Y., Sun, K. N., & Rooney, D. (2014). Facile Synthesis of Anatase TiO2 Quantum- Dot/GrapheneNanosheet Composites with Enhanced Electrochemical Performance for Lithium-Ion Batteries. *Advanced Materials, 26*(13), 2084-2088.

Mostafa, N. Y., Shaltout, A. A., Omar, H., & Abo-El-Enein, S. A. (2009). Hydrothermal synthesis and characterization of aluminium and sulfate substituted 1.1 nm tobermorites. *J. Alloy. Compd., 467*(1-2), 332-337.

Muruganandham, M., Amutha, R., & Sillanpaa, M. (2010). Reagents for ZnS Hierarchical and Non-Hierarchical Porous Self-Assembly. *ACS Applied Materials & Interfaces, 2*(7), 1817-1823.

Nath, S., Kalmodia, S., & Basu, B. (2013). In vitro biocompatibility of novel biphasic calcium phosphate-mullite composites. *Journal of Biomaterials Applications, 27*(5), 497-509.

Ni, S. Y., Chang, J., & Chou, L. (2006). A novel bioactive porous CaSiO3 scaffold for bone tissue engineering. *Journal of Biomedical Materials Research Part A, 76A*(1), 196-205.

Ni, S. Y., Chang, J., & Chou, L. (2008). In vitro studies of novel CaO-SiO(2)-MgO system composite bioceramics. *Journal of Materials Science-Materials in Medicine, 19*(1), 359-367.

Ni, S. Y., Chang, J., Chou, L., & Zhai, W. Y. (2007). Comparison of osteoblast-like cell responses to calcium silicate and tricalcium phosphate ceramics in vitro. *Journal of Biomedical Materials Research Part B-Applied Biomaterials, 80B*(1), 174-183.

Nieto, A., Lahiri, D., & Agarwal, A. (2012). Synthesis and properties of bulk graphene nanoplatelets consolidated by spark plasma sintering. *Carbon, 50*(11), 4068-4077.

Nieto, Andy, Lahiri, Debrupa, & Agarwal, Arvind. (2013). Graphene NanoPlatelets reinforced tantalum carbide consolidated by spark plasma sintering. *Materials Science And Engineering A-Structural Materials Properties Microstructure And Processing, 582*(0), 338-346.

Nonat, A. (2004). The structure and stoichiometry of C-S-H. *Cement and Concrete Research, 34*(9), 1521-1528.

O'Mahony, A. M., Williams, J. L., & Spencer, P. (2001). Anisotropic elasticity of cortical and cancellous bone in the posterior mandible increases peri-implant stress and strain under oblique loading. *Clinical Oral Implants Research, 12*(6), 648-657.

Osticioli, I., Mendes, N. F. C., Nevin, A., Gil, F. R. C., Becucci, M., & Castellucci, E. (2009). Analysis of natural and artificial ultramarine blue pigments using laser induced breakdown and pulsed Raman spectroscopy, statistical analysis and light microscopy. *Spectroc. Acta Pt. A-Molec. Biomolec. Spectr., 73*(3), 525-531.

Pan, H. B., Zhao, X. L., Darvell, B. W., & Lu, W. W. (2010). Apatite-formation ability - Predictor of "bioactivity"? *Acta Biomaterialia, 6*(11), 4181-4188.

Pattanayak, D. K., Prasad, R. C., Rao, B. T., & Mohan, T. R. R. (2006). Apatite wollastonite-titanium biocomposites: Synthesis and in vitro evaluation. *Journal of the American Ceramic Society, 89*(7), 2172-2176.

Pei, L. Z., Yang, L. J., Yang, Y., Fan, C. G., Yin, W. Y., Chen, J., & Zhang, Q. F. (2010). A green and facile route to synthesize calcium silicate nanowires. *Materials Characterization, 61*(11), 1281-1285.

Pei, S. F., Zhao, J. P., Du, J. H., Ren, W. C., & Cheng, H. M. (2010). Direct reduction of graphene oxide films into highly conductive and flexible graphene films by hydrohalic acids. *Carbon, 48*(15), 4466-4474.

Pei, Songfeng, & Cheng, Hui-Ming. (2012). The reduction of graphene oxide. *Carbon, 50*(9), 3210-3228.

Peng, C., Hu, W. B., Zhou, Y. T., Fan, C. H., & Huang, Q. (2010). Intracellular Imaging with a Graphene-Based Fluorescent Probe. *Small, 6*(15), 1686-1692.

Porwal, H., Tatarko, P., Grasso, S., Hu, C. F., Boccaccini, A. R., Dlouhy, I., & Reece, M. J. (2013). Toughened and machinable glass matrix composites reinforced with graphene and graphene-oxide nano platelets. *Science And Technology Of Advanced Materials 14*(5).

Porwal, Harshit, Tatarko, Peter, Grasso, Salvatore, Khaliq, Jibran, Dlouhý, Ivo, & Reece, Mike J. (2013). Graphene reinforced alumina nano-composites. *Carbon, 64*(0), 359-369.

Prasad, Krishnamurthy, Pinjari, D. V., Pandit, A. B., & Mhaske, S. T. (2011). Synthesis of zirconium dioxide by ultrasound assisted precipitation: Effect of calcination temperature. *Ultrasonics Sonochemistry, 18*(5), 1128-1137.

Pumera, Martin. (2013). Electrochemistry of graphene, graphene oxide and other graphenoids: Review. *Electrochemistry Communications, 36*(0), 14-18.

Rafiee, M. A., Rafiee, J., Srivastava, I., Wang, Z., Song, H. H., Yu, Z. Z., & Koratkar, N. (2010). Fracture and Fatigue in Graphene Nanocomposites. *Small, 6*(2), 179-183.

Raman, Vinay, & Abbas, Ali. (2008). Experimental investigations on ultrasound mediated particle breakage. *Ultrasonics Sonochemistry, 15*(1), 55-64.

Ramanathan, T., Abdala, A. A., Stankovich, S., Dikin, D. A., Herrera-Alonso, M., Piner, R. D., . . . Brinson, L. C. (2008). Functionalized graphene sheets for polymer nanocomposites. *Nature Nanotechnology, 3*(6), 327-331.

Ramirez, Cristina, Miranzo, Pilar, Belmonte, Manuel, Osendi, Maria Isabel, Poza, Pedro, Vega-Diaz, Sofia M., & Terrones, Mauricio. (2014). Extraordinary toughening enhancement and flexural strength in Si3N4 composites using graphene sheets. *Journal of the European Ceramic Society, 34*(2), 161-169.

Ramirez, Cristina, & Osendi, Maria Isabel. Toughening in ceramics containing graphene fillers. *Ceramics International*(0).

Robinson, J. T., Tabakman, S. M., Liang, Y. Y., Wang, H. L., Casalongue, H. S., Vinh, D., & Dai, H. J. (2011). Ultrasmall Reduced Graphene Oxide with High Near-Infrared Absorbance for Photothermal Therapy. *Journal of the European Ceramic Society, 133*(17), 6825-6831.

Rouhani, P., Taghavinia, N., & Rouhani, S. (2010). Rapid growth of hydroxyapatite nanoparticles using ultrasonic irradiation. *Ultrasonics Sonochemistry, 17*(5), 853-856.

Saadaldin, S. A., & Rizkalla, A. S. (2014). Synthesis and characterization of wollastonite glass-ceramics for dental implant applications. *Dental Materials, 30*(3), 364-371.

Sadat-Shojai, M., Khorasani, M. T., Dinpanah-Khoshdargi, E., & Jamshidi, A. (2013). Synthesis methods for nanosized hydroxyapatite with diverse structures. *Acta Biomaterialia, 9*(8), 7591-7621.

Sadjadi, Samaheh, & Eskandari, M. (2013). Ultrasonic assisted synthesis of imidazo[1,2-a]azine catalyzed by ZnO nanorods. *Ultrasonics Sonochemistry, 20*(2), 640-643.

Shanthi, P. M. S., Ashok, M., Balasubramanian, T., Riyasdeen, A., & Akbarsha, M. A. (2009). Synthesis and characterization of nano-hydroxyapatite at ambient temperature using cationic surfactant. *Materials Letters, 63*(24-25), 2123-2125.

Shaw, S, Clark, SM, & Hendersona, CMB. (2000). Hydrothermal formation of the calcium silicate hydrates, ž ž. *Chemical Geology, 167*, 129-140.

Shen, J. F., Yan, B., Shi, M., Ma, H. W., Li, N., & Ye, M. X. (2011). One step hydrothermal synthesis of TiO2-reduced graphene oxide sheets. *Journal of Materials Chemistry, 21*(10), 3415-3421.

Shen, Y. H., Liu, W. C., Lin, K. L., Pan, H. B., Darvell, B. W., Peng, S. L., . . . Chang, J. A. (2011). Interfacial pH: A Critical Factor for Osteoporotic Bone Regeneration. *Langmuir, 27*(6), 2701-2708.

Shi, S. L., & Pan, W. (2007). Machinable Ti3SiC2/Hydroxyapatite bioceramic composites by spark plasma sintering. *Journal of the American Ceramic Society, 90*(10), 3331-3333.

Shi, S. L., Pan, W., Fang, M. H., & Fang, Z. Y. (2006). Reinforcement of hydroxyapatite bioceramic by addition of Ti3SiC2. *Journal of the American Ceramic Society, 89*(2), 743-745.

Shirazi, F. S., Mehrali, M., Oshkour, A. A., Metselaar, H. S. C., Kadri, N. A., & Abu Osman, N. A. (2014). Mechanical and physical properties of calcium silicate/alumina composite for biomedical engineering applications. *Journal of the Mechanical Behavior of Biomedical Materials, 30*(0), 168-175.

Shirazi, F. S., Moghaddam, E., Mehrali, M., Oshkour, A. A., Metselaar, H. S. C., Kadri, N. A., . . . Abu, N. A. (2014). In vitro characterization and mechanical properties of β-calcium silicate/POC composite as a bone fixation device. *Journal of Biomedical Materials Research Part A*, n/a-n/a.

Siddique, Y. H., Fatima, A., Jyoti, S., Naz, F., Rahul, Khan, W., . . . Naqvi, A. H. (2013). Evaluation of the Toxic Potential of Graphene Copper Nanocomposite (GCNC) in the Third Instar Larvae of Transgenic Drosophila melanogaster (hsp70-lacZ)Bg(9). *Plos One, 8*(12).

Silver, I. A., Deas, J., & Erecinska, M. (2001). Interactions of bioactive glasses with osteoblasts in vitro: effects of 45S5 Bioglass (R), and 58S and 77S bioactive glasses on metabolism, intracellular ion concentrations and cell viability. *Biomaterials, 22*(2), 175-185.

Simitzis, J., & Baciu, D. E. (2012). In Vitro Bioactivity Investigation Of Porous Calcium Silicate Bioactive Glasses Prepared By Sol-Gel Using Peg Beads As Template. *Digest Journal of Nanomaterials and Biostructures, 7*(4), 1719-1725.

Singh, Shiv Prakash, & Karmakar, Basudeb. (2011). Mechanochemical Synthesis of Nano Calcium Silicate Particles at Room Temperature. *New Journal of Glass and Ceramics, 1*(2), 49-52.

Siriphannon, P., Kameshima, Y., Yasumori, A., Okada, K., & Hayashi, S. (2000). Influence of preparation conditions on the microstructure and bioactivity of α-CaSiO3 ceramics: Formation of hydroxyapatite in simulated body fluid. *Journal of Biomedical Materials Research, 52*(1), 30-39.

Siriphannon, P., Kameshima, Y., Yasumori, A., Okada, K., & Hayashi, S. (2002). Formation of hydroxyapatite on CaSiO3 powders in simulated body fluid. *Journal of the European Ceramic Society, 22*(4), 511-520.

Song, Y. H., Ju, Y., Song, G. B., & Morita, Y. (2013). In vitro proliferation and osteogenic differentiation of mesenchymal stem cells on nanoporous alumina. *International Journal of Nanomedicine, 8*, 2745-2756.

Sookhakian, M., Amin, Y. M., & Basirun, W. J. Hierarchically ordered macro-mesoporous ZnS microsphere with reduced graphene oxide supporter for a highly efficient photodegradation of methylene blue. *Applied Surface Science*(0).

Speiser, C., Baumann, T., & Niessner, R. (2000). Morphological and chemical characterization of calcium hydrate phases formed in alteration processes of deposited municipal solid waste incinerator bottom ash. *Environmental Science & Technology, 34*(23), 5030-5037.

Sprio, S., Tampieri, A., Celotti, G., & Landi, E. (2009). Development of hydroxyapatite/calcium silicate composites addressed to the design of load-bearing bone scaffolds. *Journal of the Mechanical Behavior of Biomedical Materials, 2*(2), 147-155.

Stankovich, S., Dikin, D. A., Piner, R. D., Kohlhaas, K. A., Kleinhammes, A., Jia, Y., . . . Ruoff, R. S. (2007). Synthesis of graphene-based nanosheets via chemical reduction of exfoliated graphite oxide. *Carbon, 45*(7), 1558-1565.

Suk, J. W., Piner, R. D., An, J. H., & Ruoff, R. S. (2010). Mechanical Properties of Mono layer Graphene Oxide. *ACS Nano, 4*(11), 6557-6564.

Tagliente, M. A., & Massaro, M. (2008). Strain-driven (0 0 2) preferred orientation of ZnO nanoparticles in ion-implanted silica. *Nuclear Instruments and Methods in Physics Research Section B: Beam Interactions with Materials and Atoms, 266*(7), 1055-1061.

Tang, J., Chen, Q., Xu, L. G., Zhang, S., Feng, L. Z., Cheng, L., . . . Peng, R. (2013). Graphene Oxide-Silver Nanocomposite As a Highly Effective Antibacterial Agent with Species-Specific Mechanisms. *ACS Applied Materials & Interfaces, 5*(9), 3867-3874.

Tapasztó, O., Kun, P., Wéber, F., Gergely, G., Balázsi, K., Pfeifer, J., . . . Balázsi, C. (2011). Silicon nitride based nanocomposites produced by two different sintering methods. *Ceramics International, 37*(8), 3457-3461.

Taylor, H. F. W. (1986). Proposed Structure For Calcium Silicate Hydrate Gel. *Journal of the American Ceramic Society, 69*(6), 464-467.

Thrivikraman, G., Madras, G., & Basu, B. (2014). In vitro/In vivo assessment and mechanisms of toxicity of bioceramic materials and its wear particulates. *Rsc Advances, 4*(25), 12763-12781.

Tjong, S. C., & Lau, K. C. (1999). Properties and abrasive wear of TiB2/Al-4%Cu composites produced by hot isostatic pressing. *Composites Science and Technology, 59*(13), 2005-2013.

Tripathi, G., & Basu, B. (2012). A porous hydroxyapatite scaffold for bone tissue engineering: Physico-mechanical and biological evaluations. *Ceramics International, 38*(1), 341-349.

Tsoukleri, G., Parthenios, J., Papagelis, K., Jalil, R., Ferrari, A. C., Geim, A. K., . . . Galiotis, C. (2009). Subjecting a Graphene Monolayer to Tension and Compression. *Small, 5*(21), 2397-2402.

Vichaphund, S., Kitiwan, M., Atong, D., & Thavorniti, P. (2011). Microwave synthesis of wollastonite powder from eggshells. *Journal of the European Ceramic Society, 31*(14), 2435-2440.

Vukovich, Milan. (1956). Effect of Wollastonite Substitutions in a Semivitreous Dinnerware Body. *Journal of the American Ceramic Society, 39*(10), 323-329.

Walker, L. S., Marotto, V. R., Rafiee, M. A., Koratkar, N., & Corral, E. L. (2011). Toughening in Graphene Ceramic Composites. *ACS Nano, 5*(4), 3182-3190.

Wan, X. H., Chang, C. K., Mao, D. L., Jiang, L., & Li, M. (2005). Preparation and in vitro bioactivities of calcium silicate nanophase materials. *Materials Science & Engineering C-Biomimetic and Supramolecular Systems, 25*(4), 455-461.

Wang, D. W., Wu, K. H., Gentle, I. R., & Lu, G. Q. (2012). Anodic chlorine/nitrogen co-doping of reduced graphene oxide films at room temperature. *Carbon, 50*(9), 3333-3341.

Wang, H., Wang, Y., Xu, J., Yang, H., Lee, C. S., & Rogach, A. L. (2012). Polyvinylpyrrolidone-assisted ultrasonic synthesis of Sno nanosheets and their use as conformal templates for tin dioxide nanostructures. *Langmuir, 28*(28), 10597-10601.

Wang, Kai, Wang, Yongfang, Fan, Zhuangjun, Yan, Jun, & Wei, Tong. (2011). Preparation of graphene nanosheet/alumina composites by spark plasma sintering. *Materials Research Bulletin, 46*(2), 315-318.

Wei, J., Chen, F. P., Shin, J. W., Hong, H., Dai, C. L., Su, J. C., & Liu, C. S. (2009). Preparation and characterization of bioactive mesoporous wollastonite - Polycaprolactone composite scaffold. *Biomaterials, 30*(6), 1080-1088.

Wei, J., Heo, S. J., Li, C. S., Kim, D. H., Kim, S. E., Hyun, Y. T., . . . Shin, J. W. (2009). Preparation and characterization of bioactive calcium silicate and poly(epsilon-caprolactone) nanocomposite for bone tissue regeneration. *Journal of Biomedical Materials Research Part A, 90A*(3), 702-712.

Wilson, Judy R., Mills, John G., Prather, Irvine D., & Dimitrijevich, S. Dan. (2005). A Toxicity Index of Skin and Wound Cleansers Used on In Vitro Fibroblasts and Keratinocytes. *Advances in Skin & Wound Care, 18*(7), 373-378.

Wu, C., & Chang, J. (2013). A review of bioactive silicate ceramics. *Biomedical Materials (Bristol), 8*(3).

Wu, C. T., & Chang, J. (2013). A review of bioactive silicate ceramics. *Biomedical Materials, 8*(3).

Wu, C. T., Ramaswamy, Y., Kwik, D., & Zreiqat, H. (2007). The effect of strontium incorporation into CaSiO3 ceramics on their physical and biological properties. *Biomaterials, 28*(21), 3171-3181.

Wu, C. T., Ramaswamy, Y., Soeparto, A., & Zreiqat, H. (2008). Incorporation of titanium into calcium silicate improved their chemical stability and biological properties. *Journal of Biomedical Materials Research Part A, 86A*(2), 402-410.

Wu, J., Zhu, Y. J., Cao, S. W., & Chen, F. (2010). Hierachically Nanostructured Mesoporous Spheres of Calcium Silicate Hydrate: Surfactant-Free Sonochemical Synthesis and Drug-Delivery System with Ultrahigh Drug-Loading Capacity. *Advanced Materials, 22*(6), 749-+.

Wu, J., Zhu, Y. J., & Chen, F. (2013). Ultrathin Calcium Silicate Hydrate Nanosheets with Large Specific Surface Areas: Synthesis, Crystallization, Layered Self-Assembly and Applications as Excellent Adsorbents for Drug, Protein, and Metal Ions. *Small, 9*(17), 2911-2925.

Wu, Jin, Zhu, Ying-Jie, Cao, Shao-Wen, & Chen, Feng. (2010). Hierachically Nanostructured Mesoporous Spheres of Calcium Silicate Hydrate: Surfactant-Free Sonochemical Synthesis and Drug-Delivery System with Ultrahigh Drug-Loading Capacity. *Advanced Materials, 22*(6), 749-753.

Xu, S., Lin, K., Wang, Z., Chang, J., Wang, L., Lu, J., & Ning, C. (2008). Reconstruction of calvarial defect of rabbits using porous calcium silicate bioactive ceramics. *Biomaterials, 29*(17), 2588-2596.

Xu, Z. P., & Buehler, M. J. (2010). Geometry Controls Conformation of Graphene Sheets: Membranes, Ribbons, and Scrolls. *ACS Nano, 4*(7), 3869-3876.

Xue, W. C., Liu, X. Y., Zheng, X. B., & Ding, C. X. (2005). In vivo evaluation of plasma-sprayed wollastonite coating. *Biomaterials, 26*(17), 3455-3460.

Xynos, I. D., Edgar, A. J., Buttery, L. D. K., Hench, L. L., & Polak, J. M. (2000). Ionic products of bioactive glass dissolution increase proliferation of human osteoblasts and

induce insulin-like growth factor II mRNA expression and protein synthesis. *Biochemical and Biophysical Research Communications, 276*(2), 461-465.

Yadhukulakrishnan, Govindaraajan B., Karumuri, Sriharsha, Rahman, Arif, Singh, Raman P., Kalkan, A. Kaan, & Harimkar, Sandip P. (2013). Spark plasma sintering of graphene reinforced zirconium diboride ultra-high temperature ceramic composites. *Ceramics International, 39*(6), 6637-6646.

Yelten, A., Yilmaz, S., & Oktar, F. N. (2012). Sol-gel derived alumina-hydroxyapatite-tricalcium phosphate porous composite powders. *Ceramics International, 38*(4), 2659-2665.

Yu, P., Kirkpatrick, R. J., Poe, B., McMillan, P. F., & Cong, X. D. (1999). Structure of calcium silicate hydrate (C-S-H): Near-, mid-, and far-infrared spectroscopy. *Journal of the American Ceramic Society, 82*(3), 742-748.

Yu, Ping, Kirkpatrick, R. James, Poe, Brent, McMillan, Paul F., & Cong, Xiandong. (1999). Structure of Calcium Silicate Hydrate (C-S-H): Near-, Mid-, and Far-Infrared Spectroscopy. *Journal of the American Ceramic Society, 82*(3), 742-748.

Zapanta-Legeros, R. (1965). Effect of Carbonate on the Lattice Parameters of Apatite [18]. *Nature, 206*(4982), 403-404.

Zeng, H. D., Cao, Y., Xie, S. F., Yang, J. H., Tang, Z. H., Wang, X. Y., & Sun, L. Y. (2013). Synthesis, optical and electrochemical properties of ZnO nanowires/graphene oxide heterostructures. *Nanoscale Research Letters, 8*.

Zhang, H., Peng, C., Yang, J. Z., Lv, M., Liu, R., He, D. N., . . . Huang, Q. (2013). Uniform Ultrasmall Graphene Oxide Nanosheets with Low Cytotoxicity and High Cellular Uptake. *ACS Applied Materials & Interfaces, 5*(5), 1761-1767.

Zhang, L., Liu, W. W., Yue, C. G., Zhang, T. H., Li, P., Xing, Z. W., & Chen, Y. (2013). A tough graphene nanosheet/hydroxyapatite composite with improved in vitro biocompatibility. *Carbon, 61*, 105-115.

Zhang, L. M., Xia, J. G., Zhao, Q. H., Liu, L. W., & Zhang, Z. J. (2010). Functional Graphene Oxide as a Nanocarrier for Controlled Loading and Targeted Delivery of Mixed Anticancer Drugs. *Small, 6*(4), 537-544.

Zhang, Lv, Liu, Weiwei, Yue, Chunguang, Zhang, Taihua, Li, Pei, Xing, Zhanwen, & Chen, Yao. (2013). A tough graphene nanosheet/hydroxyapatite composite with improved in vitro biocompatibility. *Carbon, 61*(0), 105-115.

Zhang, M., & Chang, J. (2010). Surfactant-assisted sonochemical synthesis of hollow calcium silicate hydrate (CSH) microspheres for drug delivery. *Ultrasonics Sonochemistry, 17*(5), 789-792.

Zhang, Ping, Qian, Guangren, Xu, Zhi Ping, Shi, Huisheng, Ruan, Xiuxiu, Yang, Jing, & Frost, Ray L. (2012). Effective adsorption of sodium dodecylsulfate (SDS) by hydrocalumite (CaAl-LDH-Cl) induced by self-dissolution and re-precipitation mechanism. *Journal of Colloid and Interface Science, 367*(1), 264-271.

Zhang, X., Li, M., Wang, Y. B., Cheng, Y., Zheng, Y. F., Xi, T. F., & Wei, S. C. (2013). Cell response of nanographene platelets to human osteoblast-like MG63 cells. *Journal of Biomedical Materials Research Part A*, n/a-n/a.

Zhang, Y. Z., Venugopal, J. R., El-Turki, A., Ramakrishna, S., Su, B., & Lim, C. T. (2008). Electrospun biomimetic nanocomposite nanofibers of hydroxyapatite/chitosan for bone tissue engineering. *Biomaterials, 29*(32), 4314-4322.

Zhao, S. J., Wang, L. J., Jiang, W., Zhang, J. F., & Chen, L. D. (2008). Mechanical Properties of CaSiO3/Ti3SiC2 Composites and Hydroxyapatite Forming Ability in Simulated Body Fluid. *Materials Transactions, 49*(10), 2310-2314.

Zhao, X. J., Chen, D. L., Ru, H. Q., & Zhang, N. (2011). Zirconium nitride nano-particulate reinforced Alon composites: Fabrication, mechanical properties and toughening mechanisms. *Journal of the European Ceramic Society, 31*(5), 883-892.

Zhao, Yan, Sun, Kang-Ning, Wang, Wei-Li, Wang, Yu-Xiang, Sun, Xiao-Lin, Liang, Yan-Jie, . . . Chui, Peng-Fei. Microstructure and anisotropic mechanical properties of graphene nanoplatelet toughened biphasic calcium phosphate composite. *Ceramics International*(0).

Zhong, H. B., Wang, L. J., Fan, Y. C., He, L. F., Lin, K. L., Jiang, W., . . . Chen, L. D. (2011). Mechanical properties and bioactivity of beta-Ca2SiO4 ceramics synthesized by spark plasma sintering. *Ceramics International, 37*(7), 2459-2465.

Zhou, K., Thouas, G. A., Bernard, C. C., Nisbet, D. R., Finkelstein, D. I., Li, D., & Forsythe, J. S. (2012). Method to Impart Electro- and Biofunctionality to Neural Scaffolds Using Graphene-Polyelectrolyte Multilayers. *ACS Applied Materials & Interfaces, 4*(9), 4524-4531.

Zhou, Y., Bao, Q. L., Tang, L. A. L., Zhong, Y. L., & Loh, K. P. (2009). Hydrothermal Dehydration for the "Green" Reduction of Exfoliated Graphene Oxide to Graphene and Demonstration of Tunable Optical Limiting Properties. *Chemistry of Materials, 21*(13), 2950-2956.

Zou, Zhaoyong, Lin, Kaili, Chen, Lei, & Chang, Jiang. (2012). Ultrafast synthesis and characterization of carbonated hydroxyapatite nanopowders via sonochemistry-assisted microwave process. *ultrasound sonochemistry, 19*(6), 1174-1179.

APPENDIX

List of Publications related to the thesis

- Mehrali M, Moghaddam E, Shirazi SFS, Baradaran S, Mehrali M, et al. (2014) Synthesis, Mechanical Properties, and in Vitro Biocompatibility with Osteoblasts of Calcium Silicate–Reduced Graphene Oxide Composites. ACS applied materials & interfaces 6: 3947-3962. **Impact factor: 5.9 (Q1)**

- Mehrali M, Seyed Shirazi SF, Baradaran S, Mehrali M, Metselaar HSC, et al. (2014) Facile synthesis of calcium silicate hydrate using sodium dodecyl sulfate as a surfactant assisted by ultrasonic irradiation. Ultrasonics sonochemistry 21: 735-742. **Impact factor: 3.81 (Q1)**

- Mehrali M, Moghaddam E, Shirazi SFS, Baradaran S, Mehrali M, Latibari ST, et al. Mechanical and In Vitro Biological Performance of Graphene Nanoplatelets Reinforced Calcium Silicate Composite. PloS one. 2014;9:e106802. **Impact factor: 3.53 (Q1)**

- Mehrali M, Shirazi FS, Mehrali M, Metselaar HSC, Kadri NAB, et al. (2013) Dental implants from functionally graded materials. Journal of Biomedical Materials Research Part A 101: 3046-3057. **Impact factor: 2.834 (Q1)**

- Mehrali, Mehdi, et al. "Electrophoretic deposition of calcium silicate–reduced graphene oxide composites on titanium substrate" (under review).

List of publications during PhD study

- Talebiana S, Mehralia M, Mohanb S, raghavendranb HRB, Muhammad Afifia A. Chitosan (PEO)/bioactive glass hybrid nanofibers for bone tissue engineering 4(90), 49144-49152. RSC Advances. **Impact factor: 3.7 (Q1)**

- Shirazi F, Mehrali M, Oshkour A, Metselaar H, Kadri N, et al. (2014) Mechanical and physical properties of calcium silicate/alumina composite for biomedical engineering applications. Journal of the mechanical behavior of biomedical materials 30: 168-175. **Impact Factor: 3.3 (Q1)**

- Shirazi F, Moghaddam E, Mehrali M, Oshkour A, Metselaar H, et al. (2014) In vitro characterization and mechanical properties of β-calcium silicate/POC composite as a bone fixation device. Journal of Biomedical Materials Research Part A. **Impact factor: 2.834 (Q1)**

- Shirazi FS, Mehrali M, Ataollahi Oshkour A, Metselaar HSC, Kadri NA, et al. (2013) Characterization and Mechanical Properties of Calcium Silicate/Citric Acid–Based Polymer Composite Materials. International Journal of Applied Ceramic Technology. **Impact factor: 1.153 (Q2)**

- Baradaran S, Moghaddam E, Basirun W, Mehrali M, Sookhakian M, et al. (2014) Mechanical properties and biomedical applications of a nanotube hydroxyapatite-reduced graphene oxide composite. Carbon 69: 32-45. **Impact factor: 6.16 (Q1)**

- Mehrali M, Latibari ST, Mehrali M, Mahlia TMI, Sadeghinezhad E, Metselaar HSC. Preparation of nitrogen-doped graphene/palmitic acid shape stabilized composite phase change material with remarkable thermal properties for thermal energy storage. Applied Energy. 2014;135:339-49. **Impact factor: 5.26 (Q1)**

- Mehrali M, Latibari ST, Mehrali M, Metselaar HSC, Silakhori M (2013) Shape-stabilized phase change materials with high thermal conductivity based on paraffin/graphene oxide composite. Energy Conversion and Management 67: 275-282. **Impact factor: 3.59 (Q1)**

- Mehrali M, Latibari ST, Mehrali M, Indra Mahlia TM, Cornelis Metselaar HS (2013) Preparation and properties of highly conductive palmitic acid/graphene oxide composites as thermal energy storage materials. Energy 58: 628-634. **Impact factor: 4.15 (Q1)**

- Mehrali M, Sadeghinezhad E, Latibari ST, Kazi SN, Mehrali M, et al. (2014) Investigation of thermal conductivity and rheological properties of nanofluids containing graphene nanoplatelets. Nanoscale research letters 9: 1-12. **Impact factor: 2.524 (Q1)**

- Mehrali M, Latibari ST, Mehrali M, Mahlia TMI, Metselaar HSC. Effect of carbon nanospheres on shape stabilization and thermal behavior of phase change

materials for thermal energy storage. Energy Conversion and Management. 2014;88:206-13. **Impact factor: 3.59 (Q1)**

- Mehrali M, Latibari ST, Mehrali M, Indra Mahlia TM, Cornelis Metselaar HS, et al. (2013) Preparation and characterization of palmitic acid/graphene nanoplatelets composite with remarkable thermal conductivity as a novel shape-stabilized phase change material. Applied Thermal Engineering 61: 633-640**. Impact factor: 2.127 (Q1)**

- Mehrali M, Sadeghinezhad E, Latibari ST, Mehrali M, Togun H, et al. Preparation, characterization, viscosity, and thermal conductivity of nitrogen-doped graphene aqueous nanofluids. Journal of Materials Science: 1-16. **Impact factor: 2.163 (Q1)**

- Tahan Latibari S, Mehrali M, Mehrali M, Indra Mahlia TM, Cornelis Metselaar HS (2013) Synthesis, characterization and thermal properties of nanoencapsulated phase change materials via sol–gel method. Energy 61: 664-672. **Impact factor: 4.15 (Q1)**

- Askari E, Mehrali M, Metselaar I, Kadri N, Rahman MM (2012) Fabrication and mechanical properties of functionally graded material by electrophoretic deposition. Journal of the mechanical behavior of biomedical materials 12: 144-150. **Impact Factor: 3.3 (Q1)**

- Hee AC, Mehrali M, Metselaar HSC, Mehrali M, Osman NAA (2012) Comparison of nanostructured nickel zinc ferrite and magnesium copper zinc ferrite prepared by water-in-oil microemulsion. Electronic Materials Letters 8: 639-642. **Impact Factor: 3.97 (Q1)**

- Ranjbar N, Mehrali M, Alengaram UJ, Metselaar HSC, Jumaat MZ (2014) Compressive strength and microstructural analysis of fly ash/palm oil fuel ash based geopolymer mortar under elevated temperatures. Construction and Building Materials 65: 114-121. **Impact Factor: 2.818 (Q1)**

- Tahan Latibari S, Mehrali M, Mehrali M, Mahlia TMI, Metselaar HSC (2014) Facile Preparation of Carbon Microcapsules Containing Phase-Change Material with Enhanced Thermal Properties. The Scientific World Journal 2014. **Impact Factor: 1.730 (Q1)**

- Sadeghinezhad E, Mehrali M, Latibari ST, Mehrali M, et al, (2014) An experimental investigation of convective heat transfer using graphene nanoplatelet based nanofluids under turbulent flow conditions. Industrial & Engineering Chemistry Research. 53(31), 12455-12465. **Impact Factor: 2.206 (Q1)**

- Ranjbar N, Mehrali M, Behnia A, Alengaram UJ, Jumaat MZ (2014) Compressive strength and microstructural analysis of fly ash/palm oil fuel ash based geopolymer mortar. Materials & Design 59: 532-539**. Impact Factor: 2.913 (Q1)**